REPORT

BIOIMAGING

Bioadhesive ultrasound for long-term continuous imaging of diverse organs

Chonghe Wang[1]†, Xiaoyu Chen[1]†, Liu Wang[1], Mitsutoshi Makihata[2], Hsiao-Chuan Liu[3], Tao Zhou[1], Xuanhe Zhao[1,4]*

Continuous imaging of internal organs over days could provide crucial information about health and diseases and enable insights into developmental biology. We report a bioadhesive ultrasound (BAUS) device that consists of a thin and rigid ultrasound probe robustly adhered to the skin via a couplant made of a soft, tough, antidehydrating, and bioadhesive hydrogel-elastomer hybrid. The BAUS device provides 48 hours of continuous imaging of diverse internal organs, including blood vessels, muscle, heart, gastrointestinal tract, diaphragm, and lung. The BAUS device could enable diagnostic and monitoring tools for various diseases.

Wearable devices that can continuously monitor human physiology in a noninvasive manner represent a pivotal trend in precision and digital medicine (*1*). Particularly, deep-tissue physiology, including internal organ signals and dynamics, contains crucial information regarding health and diseases (*2*). Although current wearable devices have successfully recorded physical and chemical signals from the skin such as electrocardiogram data (*3*–*5*) and sweat metabolites and electrolytes (*6*–*8*), clinical-grade imaging of various internal organs remains a central task and a challenge in the field of wearable devices. Ultrasound imaging with zero radiation allows clinicians to evaluate tissue and organ functions and diagnose various diseases (*9*). If sampled frequently over days to months, ultrasound imaging of internal organs could help clinicians monitor health status, observe disease progression, and assess disease risks (*10*–*12*); it could also lead to discoveries in and a better understanding of developmental biology (*13*).

Wearable ultrasound devices have the potential for continuous imaging of internal organs. Conventional wearable ultrasound imaging usually relies on mounting bulky ultrasound probes on the skin by either robotic systems (*14*, *15*) or mechanical fixtures such as straps and tapes (*16*–*18*), which hamper patients' mobility and wearing convenience and comfort. In addition, conventional wearable ultrasound imaging is only applicable to limited body parts such as muscles because of the thick ultrasound probe and the high pressure exerted by the probe (*16*). For example, mechanically mounting a conventional ultrasound probe on the neck to image the carotid artery, jugular vein, and vagus nerve could cause suffocation.

Although the stretchable ultrasound imaging device has improved wearability (*12*), it still suffers from limitations, including low imaging resolution, unstable imaging quality during body motions (fig. S1), a short continuous imaging duration (1 hour), and susceptibility to device failure (table S1). (The continuous imaging duration is defined as the longest time that a device can be adhered or worn on the skin.) These limitations mainly stem from the design of the device, which consists of piezoelectric elements over a stretchable substrate (Fig. 1A). Although the stretchable substrate can deform conformally with the skin, it limits the density of elements (156 per square centimeter) and is incompatible with backing and matching layers, leading to a low imaging resolution (*12*). In addition, when the substrate deforms with the skin under body motions, the elements' spatial and angular positions vary unpredictably, which hampers the imaging stability of the device (fig. S1). Furthermore, existing wearable ultrasound devices, in both rigid and stretchable form factors, mostly rely on hydrogel or elastomer couplants for acoustic transmission to the skin (*19*–*22*). However, the hydrogel couplants usually get dehydrated or detached from the skin over a few hours (*19*, *20*), and the elastomer couplants are too damping to image deep organs (*21*, *22*) (fig. S2 and table S2).

We report a bioadhesive ultrasound (BAUS) device that consists of a thin and rigid ultrasound probe robustly adhered on the skin via a couplant layer made of a soft, tough, antidehydrating, and bioadhesive hydrogel-elastomer hybrid (Fig. 1, B to D). The BAUS probe enables a high density of elements (400 elements per square centimeter; fig. S3), stable element positions under dynamic body motions, and high reliability of the probe in long-term applications. The BAUS couplant effectively transmits acoustic waves, insulates the BAUS probe from skin deformation, and maintains robust and comfortable adhesion on the skin over 48 hours.

The BAUS probe consists of an array of high-performance piezoelectric elements with a center frequency of 3, 7, or 10 MHz (Fig. 1, E and F; fig. S3; and table S3). Each element is controlled by the top and bottom circuits of the BAUS probe. The circuit can be fabricated with three techniques: three-dimensional (3D) printing (Fig. 1F, fig. S4, and movie S2) (*23*), laser etching (*24*), and photolithography (fig. S5) (*25*), which give circuit-line resolutions of 100, 10, and 1 μm, respectively. The bottom circuit is covered by an optimized acoustic matching layer to enhance the acoustic transmission to the skin, and the top circuit is covered by an optimized acoustic backing layer to quench the resonance effect (fig. S6; see materials and methods for details on fabrication and optimization of the matching and backing layers). The BAUS probe is sealed by a layer of epoxy for high stability and reliability in long-term applications. We further designed a plug-and-play input-output to connect with the flexible flat cable (fig. S7). The BAUS probe has a thickness of 3 mm, length and width of 1 to 2 cm, and weight of 10 to 40 g (fig. S3 and table S3).

The BAUS couplant consists of a soft yet tough hydrogel composed of chitosan-polyacrylamide interpenetrating polymer networks (10 wt %) and water (90 wt %) (see materials and methods for details on fabrication of the BAUS couplant). The hydrogel is encapsulated by a thin elastomer membrane (thickness of <40 μm) of polyurethane to prevent dehydration of the hydrogel and to provide comfortable skin contact with a dry couplant surface (figs. S8 and S9). The polyurethane membrane is grafted with poly(acrylic acid) coupled with *N*-hydroxysuccinimide ester (NHS ester) to form robust bonding with the hydrogel (*26*). The hydrogel-elastomer hybrid is further coated by a thin bioadhesive layer (thickness of <10 μm) synthesized by copolymerizing poly(ethylene glycol) diacrylate, 2-ethylhexyl acrylate, acrylic acid, and acrylic acid–NHS ester (fig. S10). The carboxylic acid, ethyl, and hexyl groups in the bioadhesive can form physical bonds such as hydrogen bonds and electrostatic interactions with the skin; the NHS ester groups in the bioadhesive can form covalent amide bonds with the skin (*26*). The total thickness of the elastomer membrane and the bioadhesive layer is less than one-fourth of the acoustic wavelength to minimize the acoustic attenuation of the BAUS couplant (Fig. 2D).

To quantitatively validate that the BAUS device can robustly adhere to the skin under

[1]Department of Mechanical Engineering, Massachusetts Institute of Technology, Cambridge, MA 02139, USA. [2]Makihata Engineering, San Jose, CA 95130, USA. [3]Department of Radiology, Mayo Clinic, Rochester, MN 55905, USA. [4]Department of Civil and Environmental Engineering, Massachusetts Institute of Technology, Cambridge, MA 02139, USA.
*Corresponding author. Email: zhaox@mit.edu
†These authors contributed equally to this work.

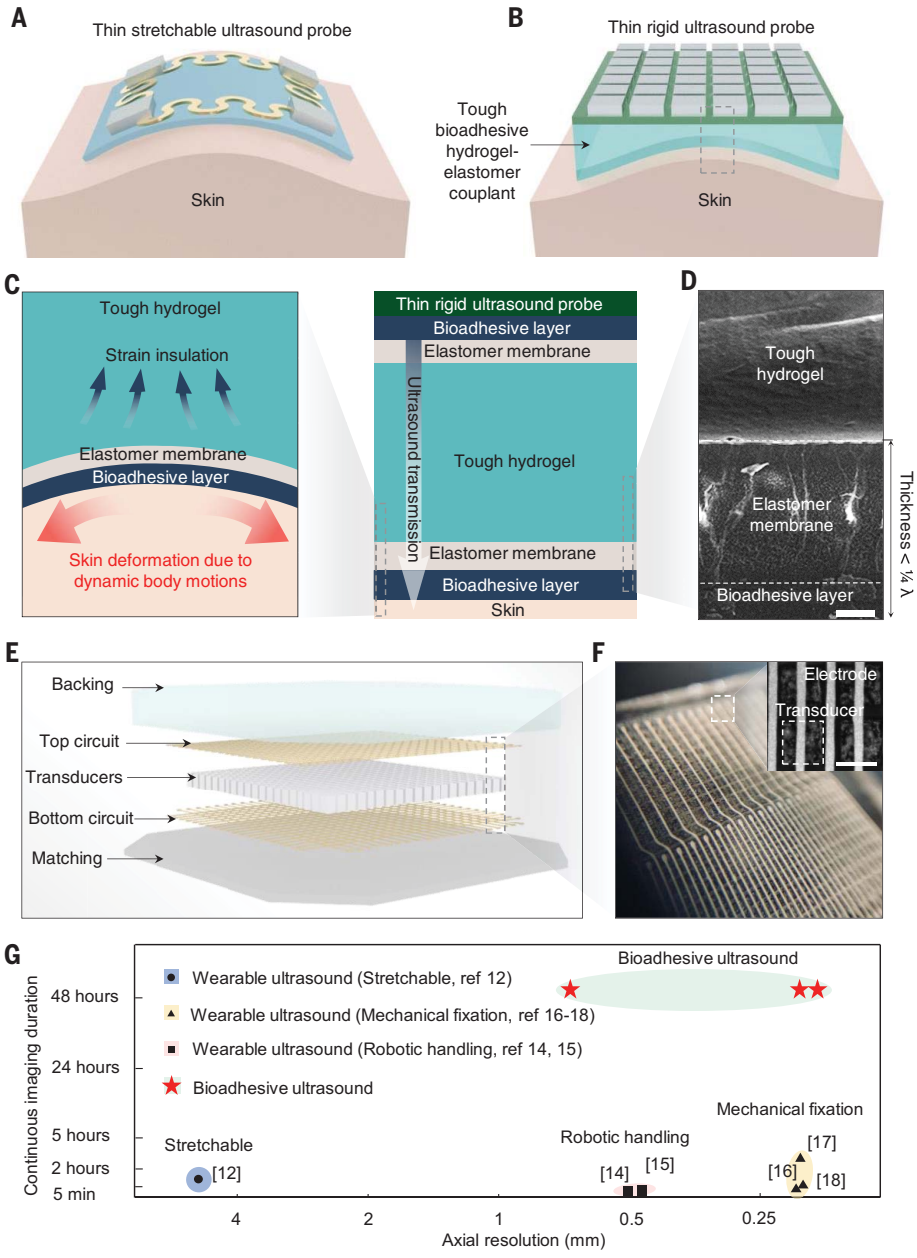

Fig. 1. Design and imaging performances of the BAUS device. (**A**) Existing epidermal wearable ultrasound imaging usually relies on thin and stretchable devices physically attached to the skin. (**B**) The BAUS device consists of a thin and rigid ultrasound probe robustly adhered to the skin via a couplant made of a soft, tough, antidehydrating, and bioadhesive hydrogel-elastomer hybrid. The dashed rectangle indicates the region shown on the right in (C). (**C**) The BAUS couplant consists of a tough hydrogel, containing 90 wt % water, that is encapsulated by an elastomer membrane further coated by a thin bioadhesive layer. The BAUS couplant maintains robust adhesion between the BAUS probe and the skin over 48 hours and insulates the BAUS probe from skin deformation during dynamic body motions. (**D**) Scanning electron microscopy (SEM) image of the cross section of the BAUS couplant. The total thickness of the elastomer membrane and the bioadhesive layer is less than one-fourth of the ultrasound wavelength λ. Scale bar is 10 μm. (**E**) Schematics of the BAUS probe structure. The BAUS probe consists of an array of high-performance piezoelectric elements, which are controlled by the top and bottom circuits. The top and bottom circuits are covered by the acoustic backing and matching layers, respectively. The dashed rectangle indicates the region shown in (F). (**F**) Optical microscopic image of a BAUS probe with 3D-printed top and bottom circuits. The inset image provides a zoomed-in top view of the device showing the top circuit and piezoelectric elements. Scale bar is 0.5 mm. (**G**) Comparison of axial-imaging resolutions and continuous-imaging durations of existing wearable ultrasound imaging devices and the BAUS device.

dynamic body motions, we developed a model of a rigid device adhered to the skin via a soft couplant layer (Fig. 2A; see fig. S11 and materials and methods for details on the model). When the skin is stretched under an applied strain ε_{app}, a crack may initiate at the edge of the couplant-skin interface and propagate. Crack propagation is driven by the energy release rate G (defined as the reduction of stored elastic energy in the couplant-skin system when the crack propagates by a unit area) and resisted by the interfacial toughness Γ (defined as the energy required to propagate the crack by a unit area). In Fig. 2B, we calculate the energy release rate G of a couplant-skin system under the plane-strain condition with a typical device length L of 2 cm and a typical applied strain on the skin ε_{app} of 20%. For simplicity of calculation, the skin and the couplant layer are taken as incompressible linear elastic materials with the same Young's modulus of 100 kPa. If the energy release rate is higher than the interfacial toughness $G > \Gamma$ (unshaded zone in Fig. 2B), the crack propagates on the interface and the device debonds from the skin. When the rigid device is physically attached on the skin without any couplant (couplant thickness $H = 0$), the interfacial toughness is ~1 J/m^2, and the rigid device detaches from the skin. By contrast, when the rigid device is adhered to the skin via the BAUS couplant, the interfacial toughness exceeds 500 J/m^2 both in air and under water (Fig. 2C), robustly bonding the device on the skin for any couplant thickness. In fig. S11, we calculate the energy release rate of the couplant-skin system with various parameters for the future design of bioadhesive devices.

To evaluate the adhesion performance of the BAUS couplant on the skin, we conducted the standard 90°-peeling test (ASTM D2861) to measure the interfacial toughness of the elastomer membrane adhered on porcine skin via the bioadhesive layer (see materials and methods for details on the test). We choose porcine skin as the model tissue for evaluating adhesion performance because of its resemblance to human skin (*26*). The elastomer membrane can establish tough adhesion on porcine skin upon contact, providing an interfacial toughness of 853 J/m^2. When the adhered sample is stored in air (relative humidity of 30 to 50%; temperature of 24°C), the interfacial toughness decreases to 756 J/m^2 over 48 hours. When the adhered sample is stored in water to simulate wet environments, the interfacial toughness decreases to 518 J/m^2 over 48 hours. These results (Fig. 2, C and E) show that the bioadhesive layer can robustly adhere the BAUS device on the skin over 48 hours in dry and wet environments. The BAUS device can be detached from the skin by peeling from one edge of the BAUS couplant without leaving any residue (fig. S12). In comparison, the

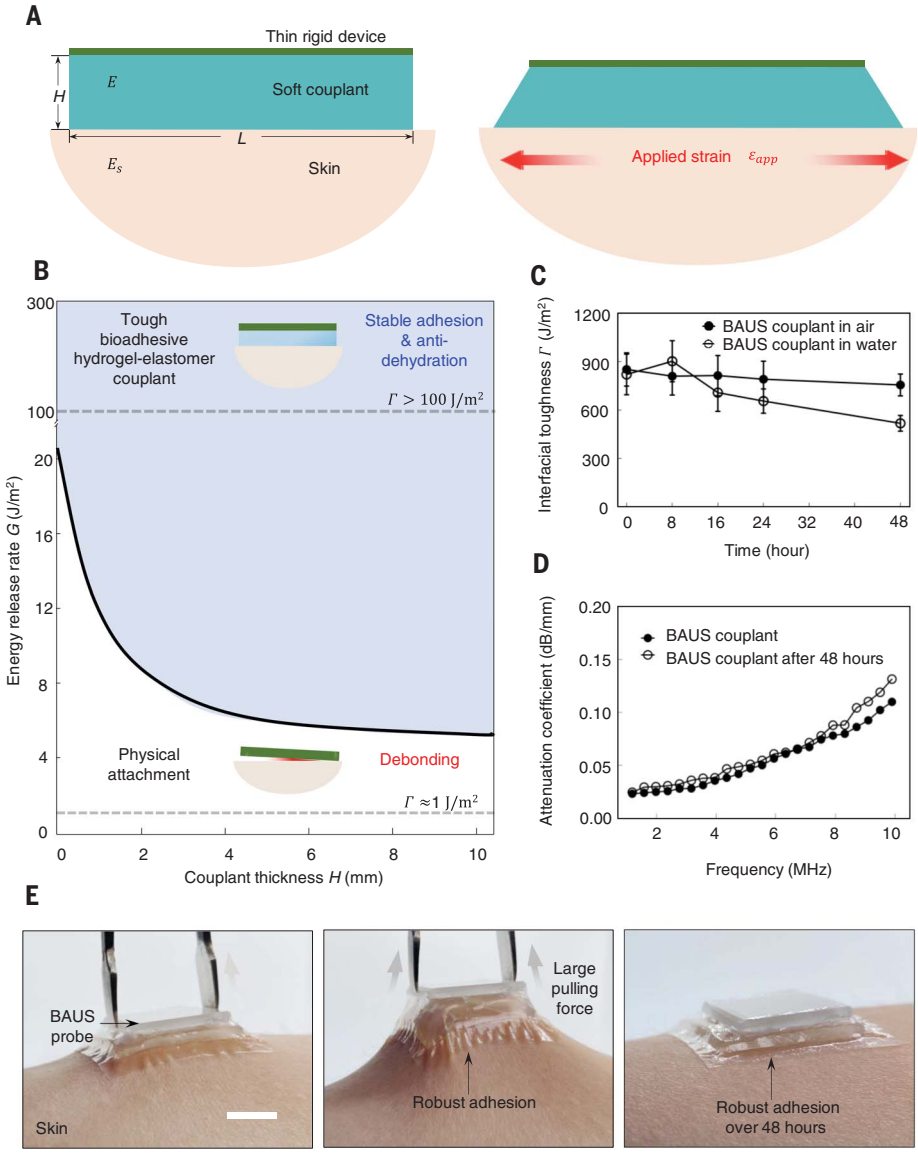

Fig. 2. Adhesion and acoustic performances of the BAUS device. (**A**) Schematics of the mechanical model for a rigid device adhered on the skin via a couplant layer. E, couplant Young's modulus; E_s, skin Young's modulus; H, couplant thickness; L, device length. (**B**) The energy release rate G as a function of the couplant thickness H calculated by the model with typical parameters: skin and couplant Young's modulus $E_s = E =$ 100 kPa, device length $L = 2$ cm, applied strain on the skin $\varepsilon_{app} = 20\%$, and interfacial toughness between the couplant and the skin Γ. (**C**) Interfacial toughness between the BAUS couplant and porcine skin measured over 48 hours after adhesion formation. Error bars indicate standard deviation (±SD) of interfacial toughness ($n = 4$ independent samples). (**D**) Acoustic attenuation coefficients of the BAUS couplant at frequencies from 1 to 10 MHz over 48 hours in air. (**E**) The BAUS device adhered on the skin can withstand high pulling forces and maintain robust adhesion on the skin over 48 hours. Scale bar is 10 mm.

interfacial toughness of typical liquid (Aquasonic Clear, Parker Labs) and solid (Aquaflex, Parker Labs) hydrogel couplants and elastomer couplants, including silicone (Ecoflex, Smooth-On), polyurethane (Sigma-Aldrich), and Aqualene (Olympus), are all less than 10 J/m^2, which cannot give stable adhesion of ultrasound probes on the skin. Although the 3M VHB acrylic tape can maintain a relatively high interfacial toughness (>456 J/m^2) in air over 48 hours, the interfacial toughness reduces to 27 J/m^2 in water, possibly leading to unstable adhesion in wet environments.

To evaluate the wearing comfort of the BAUS couplant on the skin, we adhered a set of BAUS couplants on various body locations—including arm, neck, chest, and waist—of 15 subjects for 48 hours (fig. S9). Most of the subjects reported no positive reaction (i.e., itchiness, irritation, dryness, or redness) at any location; only one subject reported minor itchiness after 48 hours of continuous wearing (fig. S13). As control samples, the abovementioned typical couplants were adhered (3M VHB acrylic tape) or mechanically wrapped (others) on the arms of the 15 subjects. The liquid and solid hydrogel couplants received the highest positive reactions, and the positive reactions of the elastomer couplants were also higher than that of the BAUS couplant. These results are consistent with the comfort level of the subjects as evaluated by the visual analog scale (VAS): the BAUS couplant is most comfortable, and the liquid and solid hydrogel couplants are least comfortable (fig. S13).

To evaluate the acoustic performance of the BAUS couplant, we used the transmission-through method to measure the attenuation coefficients of the BAUS couplant. At frequencies from 1 to 10 MHz, the attenuation coefficients of the BAUS couplant were measured to be from 0.036 to 0.131 dB/mm (Fig. 2D and fig. S14). We further measured the acoustic impedance of the BAUS couplant to be 1.59 MRayl, which matches the acoustic impedance of the skin. In comparison, the typical liquid and solid hydrogel couplants have similar attenuation coefficients as those of the BAUS couplant at frequencies from 1 to 10 MHz: 0.070 to 0.120 dB/mm and 0.117 to 0.174 dB/mm, respectively. However, the attenuation coefficients of all abovementioned elastomer couplants are multiple times higher than that of the BAUS couplant at the same frequency. This is consistent with the result that these elastomer couplants are too damping to allow wearable ultrasound imaging of internal organs (fig. S2).

To evaluate the performances of the BAUS probes, we first performed electrical impedance measurements on all elements in the probes (fig. S15 and table S4). The measured center frequency of the elements on each BAUS probe is indeed 3, 7, or 10 MHz (with a minor deviation of <5%) as prescribed; the electrical impedances of the probes at their center frequencies are 49, 36, or 43 ohms, respectively (fig. S16 and table S4). We then measured the cross-talk in each BAUS probe to be less than −40 dB, which is sufficiently low for high-quality imaging applications (fig. S17 and table S4) (*27*). We next performed the pulse-echo tests on all BAUS probes to measure their bandwidths. The measured bandwidths of the 3-, 7-, and 10-MHz BAUS probes are 68, 75, and 78%, respectively (fig. S18 and table S4).

To evaluate the imaging resolutions of the BAUS probes, we first performed the pulse-echo tests on the BAUS probes to characterize their axial resolutions (fig. S19). The axial resolutions of the 3-, 7-, and 10-MHz BAUS probes are 0.77, 0.225, and 0.1924 mm, respectively (fig. S19 and table S4). We then measured the point spread functions of the BAUS probes to characterize their lateral resolutions. The

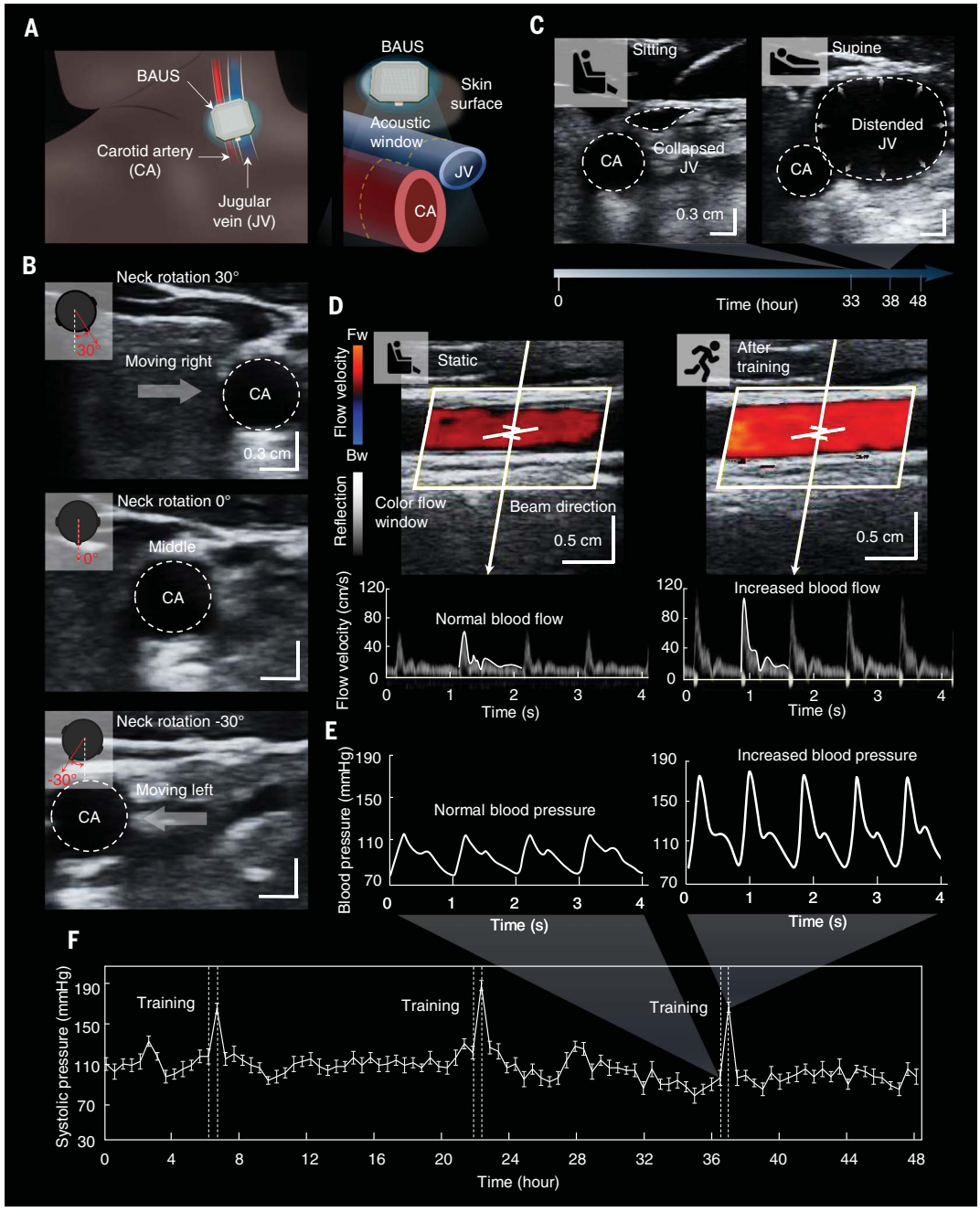

Fig. 3. Long-term continuous BAUS imaging of blood vessels. See also fig. S30 and movie S5. (**A**) Schematics of the BAUS device adhered on the neck of the subject to image the carotid artery (CA) and jugular vein (JV). (**B**) The BAUS device can stably image the blood vessels under dynamic body motions such as neck rotation with angles up to ±30°. (**C**) The diameter of the jugular vein increases substantially from the sitting or standing position to the supine position. (**D**) Color-flow imaging of the carotid artery by the BAUS device. The diameter of the carotid artery and the blood flow rate in the carotid artery increase substantially after 0.5 hours of physical exercise. Fw, forward; Bw, backward. (**E**) Blood pressure waveforms of the carotid artery before and after 0.5 hours of physical exercise. The systolic blood pressure of the carotid artery increases substantially after 0.5 hours of physical exercise. The decrease in the blood pressure from the systolic peak in each cardiac cycle is much steeper after 0.5 hours of physical exercise. (**F**) The systolic blood pressure of the carotid artery over 48 hours as measured from the BAUS imaging. The systolic blood pressure is measured by calculating the mean and standard deviation of 15 consecutive systolic peaks every 0.5 hours. Error bars indicate standard deviation (±SD) of measured systolic pressure (n = 15 independent samples). The 0.5-hour training periods are indicated by the dashed lines.

lateral resolutions of the 3-, 7-, and 10-MHz BAUS probes are 1.79, 0.38, and 0.38 mm at their imaging focal depths of 6, 3, and 2 cm, respectively (figs. S20 to S22 and table S4). These measured values are also confirmed by the acoustic simulations (figs. S20 to S22). In comparison, the axial resolution of the stretchable ultrasound imaging probe (2 MHz) is reported to be 5.775 mm (*12*).

To test the imaging stability of the BAUS device, we adhered the BAUS device on a phantom of a blood vessel in soft tissues under various frequencies of vibration (0 to 3.5 Hz with an amplitude of 2 cm) to evaluate its acoustic performance under dynamic body motions. Because of stable adhesion of the BAUS device to the phantom and the relatively high imaging frame rate (40 Hz), the motion artifact on imaging is minimal (fig. S23).

To test the thermal properties of the BAUS device, we measured the temperature of the BAUS device when continuously actuated by various levels of working voltages (0 to 90 V) over 48 hours. Owing to its low working power and thin form factor for heat dissipation, the BAUS device can maintain a constant level of temperature (24°C) while continuously imaging for 48 hours (figs. S24 and S25), validating its thermal stability in long-term applications.

We demonstrate the BAUS imaging platform's capability to perform 48-hour continuous imaging of human organs, including blood vessels and heart, muscle and diaphragm, stomach, and lung. These organs represent the cardiovascular, muscular, digestive, and respiratory systems, respectively. To image organs with depths less than 6 cm beneath the skin (i.e., jugular vein, carotid artery, and bicep muscle), we chose an ultrasound probe with a center frequency of 7 or 10 MHz and adopted the plane wave compounding method (fig. S26). To image organs deeper than 6 cm beneath the skin (i.e., heart, stomach, diaphragm, and lung), we chose an ultrasound probe with a center

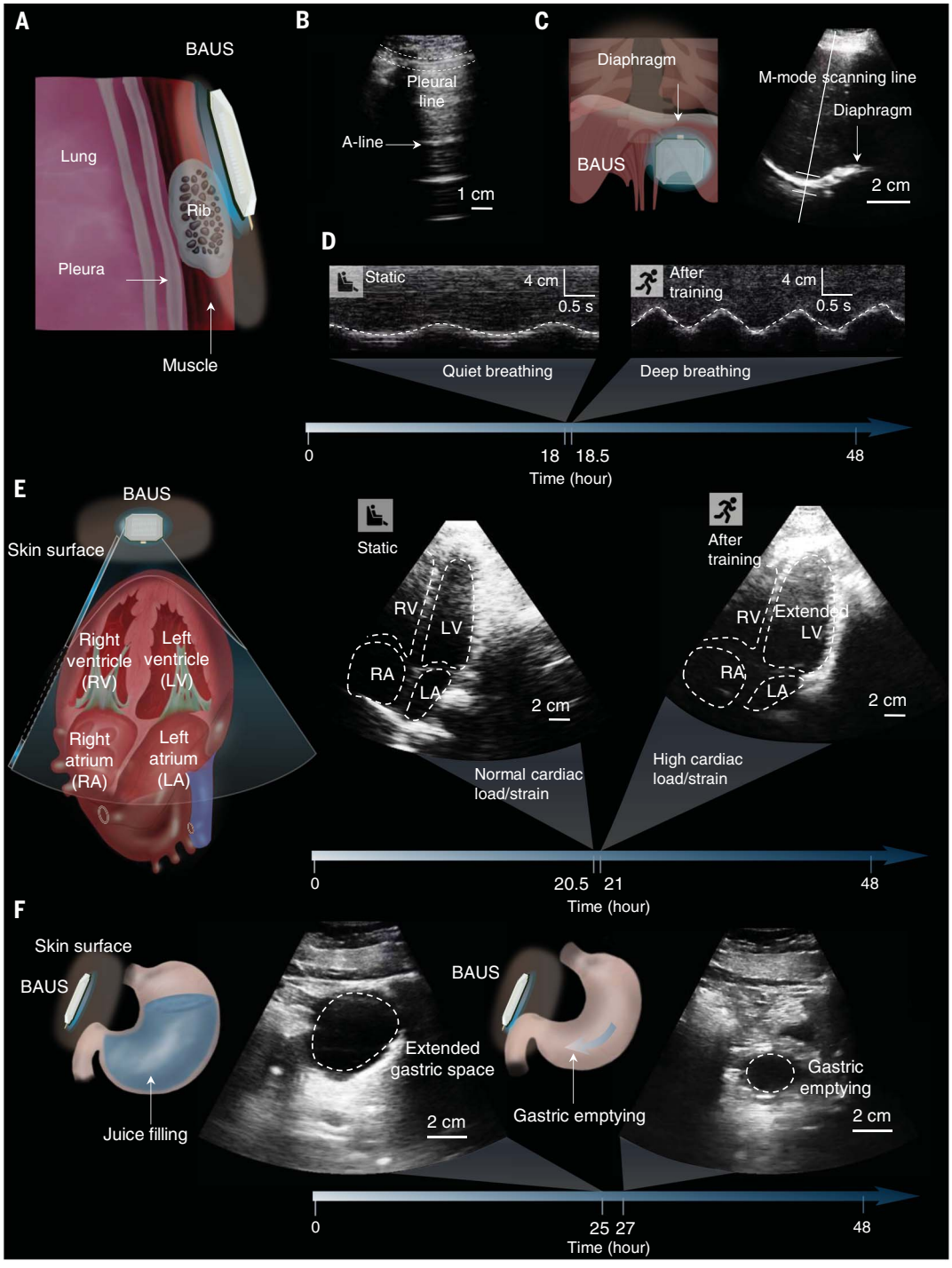

Fig. 4. Long-term continuous BAUS imaging of lung, diaphragm, heart, and stomach. See also figs. S33 to S36. (**A**) Schematics of the BAUS device adhered to the chest of the subject to image the lung. (**B**) The BAUS imaging shows a smooth pleural line and repetitive A-lines of the lung. (**C**) The BAUS imaging (right) shows clear diaphragm morphology. A diagram of the placement of the BAUS device is shown on the left. (**D**) The diaphragm motility increases substantially in amplitude and frequency after 0.5 hours of physical exercise. (**E**) The BAUS imaging shows the dynamics of the four chambers of the heart. The size of the left ventricle greatly increases after 0.5 hours of physical exercise. (**F**) The BAUS imaging shows the dynamics of the stomach. The gastric antral cross-sectional area gradually decreases after the subject drinks 450 ml of juice.

frequency of 3 MHz and adopted the phased array imaging method (figs. S27 to S29 and movies S3 and S4; see materials and methods for details on acoustic simulation). The probes are adhered to various locations on the skin of a healthy subject via the BAUS couplants for continuous imaging of the corresponding organs over 48 hours (see materials and methods for details on data acquisition and image processing).

Figure 3 and fig. S30 demonstrate the imaging results of the jugular vein and carotid artery obtained by the 10-MHz BAUS device adhered to the right-hand side of the neck (Fig. 3A). Dynamic body motions such as neck rotation can cause blood vessel shifting and skin deformation, which deteriorate the imaging quality and stability of existing wearable ultrasound devices (*11*). By contrast, the BAUS device can provide 48-hour continuous imaging of the jugular vein and carotid artery under dynamic body motions such as neck rotation with angles up to ±30° (Fig. 3B and movie S5). This is because of the robust adhesion of the BAUS device on the neck, the high imaging resolution of the BAUS probe, and the large acoustic window given by the BAUS probe aperture (2 cm by 1 cm). The BAUS imaging results show that the diameter of the jugular vein in the subject increases

from the sitting or standing position to the supine position (Fig. 3C and fig. S30). The change of the jugular vein diameter strongly correlates with the right atrium pressure (*28*) and thus can be used to diagnose cardiac diseases such as heart failure and pulmonary hypertension (*29*). The BAUS imaging results further provide 48-hour continuous blood flow rate and blood pressure waveform data of the carotid artery (Fig. 3, D to F, and fig. S30). For example, we observed dramatic increases in blood flow rate (from 65 to 117 cm/s; Fig. 3D) and systolic blood pressure (from 115 to 168 mmHg; Fig. 3E) of the carotid artery in the subject before and after 0.5 hours of physical exercise (see materials and methods for details on data acquisition and calculation of the blood pressure). Moreover, from the blood pressure waveform measured after the 0.5-hour jogging session (right panel of Fig. 3E), we can see a steeper decrease in the blood pressure from the systolic peak in each cardiac cycle than before the exercise, possibly because of the exercise-induced vasodilation of the carotid artery.

Figure S31 demonstrates the imaging results of the bicep muscle obtained by the 7-MHz BAUS device adhered to the upper arm of the subject (fig. S31). The BAUS system can provide 48-hour continuous imaging of the bicipital muscle. For example, we observed increased blood perfusion and echogenicity on the muscle and tendon interface 2 hours after a 1-hour weightlifting training session and increased vascularity 10 hours after the training (fig. S32).

Figure 4, A and B, and fig. S33 demonstrate the imaging results of the lung obtained by the 3-MHz BAUS phased-array device adhered on the right chest (longitudinal direction) of the subject (Fig. 4A). The BAUS system can provide 48-hour continuous imaging of key characteristics of the lung, including the pleural line and A-lines. The BAUS device is also able to continuously and stably image the lung under body motions such as jogging and cycling (fig. S34). The BAUS imaging shows a smooth pleural line and repetitive A-lines of the subject over 48 hours, indicating a healthy, normally aerated lung. Although lung ultrasonography has proven to be an effective tool for diagnosing COVID-19 patients (*30*), it is mostly available in hospitals for infrequent and noncontinuous imaging of the lung. By contrast, the wearable BAUS system could continuously monitor the symptoms of possibly infected COVID-19 patients at home.

Figure 4, C and D, demonstrates the imaging results of the diaphragm motility obtained by the 3-MHz BAUS phased-array device adhered on the right anterior subcostal region of the subject before and after 0.5 hours of physical exercise. The BAUS imaging shows that the diaphragm motility after training is more dramatic in amplitude and frequency compared with quiet breathing before training.

Figure 4E and fig. S35 demonstrate the imaging results of the heart obtained by the 3-MHz BAUS phased-array device adhered on the left chest of the subject (as visualized through the apical four-chamber view). The BAUS system can provide 48-hour continuous imaging of the dynamics of the four cardiac chambers: the right ventricle, right atrium, left ventricle, and left atrium. The BAUS device is also able to continuously and stably image the heart under body motions such as jogging and cycling (fig. S34). For example, we observed that the size of the left ventricle greatly increases after 0.5 hours of physical exercise. The continuous images of the cardiac chambers (fig. S35) can be further processed to calculate the dynamics of cardiac strain, which is an important parameter that could indicate cardiomyopathy.

Figure 4F and fig. S36 demonstrate the imaging results of the stomach obtained by the 3-MHz BAUS phased-array device adhered on the upper abdomen skin of the subject. The BAUS imaging system provides 48-hour continuous imaging of the gastric antral cross section. For example, we observed an extended gastric antrum once the subject drank 450 ml of juice (Fig. 4F). Over the next 2 hours, the gastric antral cross-sectional area gradually decreased because of gastric emptying (Fig. 4F and fig. S36).

Although the imaging resolutions of the BAUS probes are superior to those of existing wearable ultrasound devices (Fig. 1G and table S1), the BAUS probes can be further improved for better imaging quality in the future. The pitch of the current BAUS probes is relatively large (0.5 mm; table S3) and can cause grating lobes, especially in the 7- and 10-MHz BAUS probes. Although the grating-lobe artifacts can be alleviated by using the plane wave compounding method (fig. S26) (*31*), the pitches of future BAUS probes will be reduced to eliminate the artifacts. Although the current BAUS probes do not have elevation focusing, thin-profile (<1 mm) elevation lenses (*32*) can be added to future BAUS probes for elevation focusing to achieve better imaging quality, especially for deep organs.

Because the current work is focused on designing and fabricating the BAUS devices, we use an external system (Verasonics Vantage system) for data acquisition. Despite the large size of the data acquisition system, the BAUS devices may find immediate applications in nonmobile imaging in clinical settings such as long-term imaging of patients in intensive-care units. In addition, because the data acquisition systems of point-of-care ultrasound devices (e.g., GE VScan, Butterfly IQ, and Phillips Lumify) have been miniaturized to the size of a cell phone, the data acquisition system of BAUS can be miniaturized in the future. Beyond clinical applications, the BAUS imaging platform could provide long-term continuous imaging of the developments of tissues and organs—including embryo, tumors, and brain—in a noninvasive manner (*33*, *34*).

The current paradigm for the biointegration of devices is to make the devices thin and stretchable for conformal attachment on the body. Here, we propose a different paradigm for biointegration: to robustly adhere thin and rigid devices on the body via a soft, tough, and bioadhesive couplant (Figs. 1 and 2). Developing bioadhesive couplants that enable electrical, optical, thermal, chemical, and/or biological interfacing with the body could open new avenues to future biointegrated devices.

REFERENCES AND NOTES

1. E. Topol, *Deep Medicine: How Artificial Intelligence Can Make Healthcare Human Again* (Basic Books, 2019).
2. M. Lin, H. Hu, S. Zhou, S. Xu, *Nat. Rev. Mater.* (2022).
3. D.-H. Kim *et al*., *Science* **333**, 838–843 (2011).
4. S. Xu *et al*., *Science* **344**, 70–74 (2014).
5. S. Yang *et al*., *Adv. Mater.* **27**, 6423–6430 (2015).
6. W. Gao *et al*., *Nature* **529**, 509–514 (2016).
7. H. Lee *et al*., *Nat. Nanotechnol.* **11**, 566–572 (2016).
8. J. R. Sempionatto *et al*., *Nat. Biomed. Eng.* **5**, 737–748 (2021).
9. C. L. Moore, J. A. Copel, *N. Engl. J. Med.* **364**, 749–757 (2011).
10. C. Wang *et al*., *Nat. Biomed. Eng.* **2**, 687–695 (2018).
11. S. R. Steinhubl, E. J. Topol, *Nat. Biomed. Eng.* **2**, 633–634 (2018).
12. C. Wang *et al*., *Nat. Biomed. Eng.* **5**, 749–758 (2021).
13. C. K. L. Phoon, *Pediatr. Res.* **60**, 14–21 (2006).
14. Q. Huang, J. Lan, X. Li, *IEEE Trans. Industr. Inform.* **15**, 1173–1182 (2019).
15. H. T. Sen, M. A. L. Bell, I. Iordachita, J. Wong, P. Kazanzides, in *2013 IEEE/RSJ International Conference on Intelligent Robots and Systems* (IEEE, 2013), pp. 3071–3076.
16. H. M. Heres *et al*., *J. Med. Ultrason.* **47**, 47–56 (2020).
17. R. W. Nuckols *et al*., *Sci. Robot.* **6**, eabj1362 (2021).
18. M. Sjoerdsma *et al*., *Appl. Sci.* **11**, 1534 (2021).
19. H. R. Laine, A. Harjula, P. Peltokallio, *J. Ultrasound Med.* **6**, 33–36 (1987).
20. F. Chasset *et al*., *J. Dermatol.* **43**, 318–320 (2016).
21. E. Ginzel, R. MacNeil, R. Ginzel, M. Zuber, A. Sinclar, *NDT.net J.* **20**, 1–12 (2015).
22. J. S. Kenny *et al*., *Sci. Rep.* **11**, 7780 (2021).
23. B. Y. Ahn *et al*., *Science* **323**, 1590–1593 (2009).
24. Z. Huang *et al*., *Nat. Electron.* **1**, 473–480 (2018).
25. G. Hong *et al*., *Science* **360**, 1447–1451 (2018).
26. H. Yuk *et al*., *Nature* **575**, 169–174 (2019).
27. Q. Zhou, K. H. Lam, H. Zheng, W. Qiu, K. K. Shung, *Prog. Mater. Sci.* **66**, 87–111 (2014).
28. S. Magder, *Crit. Care Med.* **34**, 2224–2227 (2006).
29. A. E. Raine *et al*., *N. Engl. J. Med.* **315**, 533–537 (1986).
30. C. Xing *et al*., *Crit. Care* **24**, 174 (2020).
31. M. Tanter, M. Fink, *IEEE Trans. Ultrason. Ferroelectr. Freq. Control* **61**, 102–119 (2014).
32. D. G. Wildes *et al*., *IEEE Trans. Ultrason. Ferroelectr. Freq. Control* **44**, 1027–1037 (1997).
33. L. V. Wang, S. Hu, *Science* **335**, 1458–1462 (2012).
34. C. Errico *et al*., *Nature* **527**, 499–502 (2015).
35. C. Wang, X. Chen, L. Wang, M. Makihata, H.-C. Liu, T. Zhou, X. Zhao, Bioadhesive ultrasound for long-term continuous imaging of diverse organs, Version 1. Harvard Dataverse (2022).

ACKNOWLEDGMENTS

We thank Z. Zhang and B. Anthony for technical support on imaging algorithms, R. Chen for advice on device packaging, S. Lin for help on interfacial toughness tests, Y. Cao for SEM sample preparation, and H. Roh for initial involvement in device fabrication. **Funding:** This work was supported by the Defense Advanced Research Projects Agency through cooperative agreement D20AC00004, the National Science Foundation (no. EFMA-1935291), the National Institutes of Health (no. 1R01HL153857), and the US Army Research Office through the Institute for Soldier Nanotechnologies at MIT (no. W911NF-13-D-0001). X.Z. acknowledges support from a George N. Hatsopoulos (1949) Faculty Fellowship and a Humbolt Research Award. **Author contributions:** C.W. and X.Z. conceived the project. X.C. and X.Z. designed the BAUS couplant, and X.C. fabricated and characterized

the BAUS couplant. T.Z. took SEM images of the BAUS couplant. C.W. designed the BAUS probe, and C.W. and X.C. fabricated and characterized the BAUS probe. H.-C.L. designed the imaging algorithms. M.M. designed the circuit adaptor. C.W. performed the acoustic simulation. L.W. performed the mechanical simulation. C.W. and X.C. tested the BAUS device in vitro and in vivo and analyzed the results. C.W., X.Z., X.C., and L.W. wrote the paper and incorporated comments and edits from all authors. X.Z. supervised the project. **Competing interests:** X.Z., C.W., and X.C. are inventors on a patent application describing the BAUS system and technology. X.Z. has a financial interest in SanaHeal, Inc., a biotechnology company focused on the development of medical devices for surgical sealing and repair. The authors declare that they have no other competing interests. **Data and materials availability:** All data are available in the main text or the supplementary materials. The website associated with the manuscript, including data and algorithms, is available at Harvard Dataverse (*35*).

SUPPLEMENTARY MATERIALS

science.org/doi/10.1126/science.abo2542
Materials and Methods
Figs. S1 to S36
Tables S1 to S4
References (*36*, *37*)
Movies S1 to S5

Submitted 22 January 2022; resubmitted 4 April 2022
Accepted 9 June 2022
10.1126/science.abo2542

Science

Bioadhesive ultrasound for long-term continuous imaging of diverse organs

Chonghe WangXiaoyu ChenLiu WangMitsutoshi MakihataHsiao-Chuan LiuTao ZhouXuanhe Zhao

Science, 377 (6605), • DOI: 10.1126/science.abo2542

Continuous long-term ultrasound imaging

Ultrasound is widely used for the noninvasive imaging of tissues and organs, but this method requires close contact between the transducer and the target area. This can make it difficult to acquire images over a long period of time, especially if the patient needs to be mobile. Wang *et al*. describe a wearable ultrasound imaging device (see the Perspective by Tan and Lu). A rigid piezoelectric probe array is bonded to the skin with an acoustically transparent hydrogel elastomer. In vivo testing showed that the device could be comfortably worn for 48 hours, and hooking the array up to a commercially available ultrasound platform allowed for continuous ultrasound images of the carotid artery, lung, and abdomen. —MSL

Science (ISSN) is published by the American Association for the Advancement of Science. 1200 New York Avenue NW, Washington, DC 20005. The title *Science* is a registered trademark of AAAS.

Science
AAAS

Supplementary Materials for

Bioadhesive ultrasound for long-term continuous imaging of diverse organs

Chonghe Wang *et al*.

Corresponding author: Xuanhe Zhao, zhaox@mit.edu

Science **377**, 517 (2022)
DOI: 10.1126/science.abo2542

The PDF file includes:

Other Supplementary Material for this manuscript includes the following:

Materials and Methods

Finite element simulations of the couplant-skin system

Finite element simulations are conducted using the commercial package Abaqus/standard. Both the couplant and the skin are modeled as incompressible linear elastic materials with Poisson's ratio of $v = 0.5$ and Young's moduli of E and E_s, respectively. The plane strain condition is adopted in the simulations, and the plane strain moduli of the couplant and the skin are denoted as $E^* = E/(1-v^2)$ and $E_s^* = E_s/(1-v^2)$, respectively. A symmetric model about the y-axis is adopted as shown in fig. S11A and B. A significantly large substrate of the skin is modelled (not fully shown in the figure) and a strain $\varepsilon_{app} = 20\%$ is applied on the skin. Notably, 20% is typically the maximum tensile strain that the normal skin can sustain without feeling pains. To simulate the initial crack, a seam with length *a* is assigned at the edge of the couplant/skin interface. Meshes around the crack tip are carefully controlled such that circular contours can be generated to compute the J-integral around the crack tip. Thereafter, the energy release rate G is calculated by averaging the J-integrals of the six contours. By taking $E = E_s = 100$ kPa and L=2 cm while varying the initial crack length *a* and the thickness of the couplant *H*, we can plot the energy release rate as a function of the normalized crack length *a* /*L* under various values of *H*/*L* in fig. S11C. The maximum energy release rate $G_{\max}$ is then determined as the peak value of each curve as highlighted by the red dot in fig. S11C. Based on those results, we can see that the maximum energy release rate $G_{\max}$ increases as the couplant becomes thinner. Notably, the energy release rate *G* used in Fig. 2B is taken from the $G_{\max}$ calculated here.

By further tunning the modulus of the couplant, we can plot the normalized maximum energy release rate $G_{\max}/\left(E_s^* L\varepsilon_{app}^2\right)$ as a function of normalized thickness *H*/*L* under various E^*/E_s^* in fig. S11D. It is evident that the maximum energy release rate increases when the couplant gets stiffer and thinner. And the upper limit of $G_{\max}$ is achieved when the couplant is becoming rigid, i.e., $E^* \to \infty$. Note that this extreme scenario is essentially the same as the scenario when the thickness of the couplant is approaching zero, i.e., $H \to 0$ since the top surface of the bioadhesive is assumed to be bonded on a rigid device.

Analytical solutions of the couplant-skin system

Analytical solutions can be derived when the couplant is rigid $E^* \to \infty$. For a rigid punch bonded to an infinitely large substrate, the displacement at plane y=0 in x-direction within the bonded zone (i. e., $0 \le x \le L/2 - a$) in the initial configuration can be written as

$$u = 0. \tag{1}$$

Consider an intermediate configuration where the substrate undergoes an applied strain ε_{app} without constraints at y=0. The displacement within the $0 \le x \le L/2 - a$ is uniform and can be written as

$$u_1 = \varepsilon_{app} x \tag{2}$$

Now assume a shear stress $q(x)$ is applied at plane y=0 in the intermediate configuration such that the displacement field within the $0 \le x \le L/2 - a$ is changed from Eq. 2 to Eq. 1, i.e., $q(x)$ yields a displacement

$$u_2 = -\varepsilon_{app} x \tag{3}$$

$q(x)$ can be calculated as *(36)*

$$q(x) = -\frac{2}{3} E \frac{x}{\sqrt{(L/2-a)^2 - x^2}} \varepsilon_{app} \tag{4}$$

Given that initial and intermediate configurations are interchangeable in linear elasticity, Eq. (4) represents the shear stress within the bonded zone. From Eq. (4) one can further calculate the Mode II stress intensity factor

$$K_{II} = \lim_{x \to L/2-a} q(x) \sqrt{2\pi \left(\frac{L}{2} - a - x\right)} = -\frac{2}{3} E \sqrt{\pi \left(\frac{L}{2} - a\right)} \varepsilon_{app} \tag{5}$$

Therefore, the energy release rate can be calculated as

$$G = \frac{1}{2E_s^*} (K_{II})^2 = \frac{\pi}{6} E_s \left(\frac{L}{2} - a\right) \varepsilon_{app}^2 \tag{6}$$

Plugging $E_s = 100$ kPa, $L = 2$ cm, $\varepsilon_{app} = 0.2$, Eq. (6) is plotted as the magenta curve in fig. S11C. The maximum energy release rate $G_{\max} = 20.9$ J/m^2 is achieved when $a \to 0$.

Fabrication of the BAUS couplant

All chemicals were obtained from Sigma-Aldrich unless otherwise indicated and used without further purification. The chemicals for synthesizing the tough hydrogel include acrylamide (AAm), acetic acid (AAc), α-ketoglutaric acid, chitosan (high molecular weight), *N, N*′-methylenebisacrylamide (MBA), calcium chloride ($CaCl_2$). The chemicals for synthesizing the elastomer membrane include hydrophilic polyurethane (Advan Source biomaterials), hydrophobic polyurethane (Advan Source biomaterials), acrylic acid (AAc), benzophenone, α-ketoglutaric acid, 1-ethyl-3-(3-dimethylaminopropyl) carbodiimide (EDC), and *N*-hydroxysuccinimide ester (NHS ester), tetrahydrofuran (THF), *N, N*-Dimethylformamide (DMF), and ethanol. The chemicals for synthesizing the bioadhesive layer include acrylic acid (AAc), acrylic acid *N*-hydroxysuccinimide ester (AAc-NHS ester), 2-hydroxy-4′-(2-hydroxyethoxy)-2-methylpropiophenone (Irgacure 2959), polycaprolactone polyurethane, 2-ethylhexyl acrylate (EHA), poly(ethylene glycol) diacrylate (average Mn 560, PEGDA), and ethanol.

To prepare the PAAm-chitosan tough hydrogel, we dissolved 3% (w/w) high molecular weight chitosan, 12% (w/w) acrylamide, 0.15% (w/w) *N, N*′-methylenebisacrylamide, 0.3% (w/w) α-ketoglutaric acid,1% (w/w) acetic acid in deionized water. The mixture was then centrifuged at 9000 rpm to remove air bubbles and poured into a glass mold with a transparent cover. The solution was cured in ultraviolet light (UV) chamber (364 nm, 10 W power) for 60 min. The obtained tough hydrogels were immersed in 1M $CaCl_2$ solution for 24 hours to reach an equilibrium state.

To prepare the polyurethane elastomer membrane, an adhesive polyurethane was first made by grafting PAA chains onto hydrophilic polyurethane. Specifically, we dissolved 32% (w/w) acrylic acid, 8% (w/w) hydrophilic polyurethane (AdvanSource Biomaterial), 1.5% (w/w) benzophenone, and 0.3% (w/w) α-ketoglutaric acid in nitrogen-purged deionized water and ethanol mixture (water:ethanol = 1:2 v/v). The mixture was degassed and reacted under ultraviolet light (UV) (364 nm, 10 W power) for 120 min. After the reaction, the mixture solution was dialyzed (Cutoff Mn 3000 Da) against ethanol for 3 days and against water for 3 more days to obtain the pure adhesive polyurethane. The purified adhesive polyurethane was washed with water and fully dried for future use. Then a thin layer of hydrophobic polyurethane (30% (w/w) hydrophobic polyurethane in a mixture of DMF, THF, and acetone (DMF:THF:Acetone = 3:3:4 v/v)) was spin-coated at 1500 rpm on a clean glass. After the hydrophobic polyurethane was fully dried, a thin layer of hydrophilic polyurethane (30% (w/w) hydrophilic polyurethane in deionized water and ethanol mixture (water:ethanol = 1:2 v/v)) was spin-coated at 1500 rpm on the hydrophobic polyurethane layer. Then, a thin layer of adhesive polyurethane with EDC and NHS (30% (w/w) adhesive polyurethane, 5% (w/w) EDC, and 5% (w/w) NHS in nitrogen-purged deionized water and ethanol mixture (water:ethanol = 1:2 v/v)) was spin-coated at 1500 rpm on the hydrophilic polyurethane layer. After the film was fully dried in airflow for 4 hours, the polyurethane elastomer membrane was obtained.

To prepare the bioadhesive layer, we dissolved 0.5% (w/w) Irgacure 2959, 0.05% (w/w) PEGDA, 12% (w/w) AAc, 3% (w/w) AAc-NHS ester, 35% (w/w) EHA in nitrogen-purged ethanol. The mixture was then poured on a glass mold with spacers. The adhesive film was obtained after curing the mixture under ultraviolet light (UV) (364 nm, 10 W power) for 40 min.

To integrate the above components into the hydrogel-elastomer hybrid, the tough hydrogel was cut into desired shape and size, and then we carefully adhered the adhesive polyurethane side of the elastomer membrane onto the tough gel with a gentle press to avoid any bubbles. Then the hydrophobic side of the polyurethane was adhered to one side of the bioadhesive layer by 50% (w/w) hydrophilic polyurethane in nitrogen-purged deionized water and ethanol mixture (water:ethanol = 1:2 v/v). The edge of the elastomer and bioadhesive encapsulation was cut and sealed by laser sintering.

Acoustic simulation of the ultrasound probe

The calculations of the acoustic beam directivity, beamwidth, penetration, and intensity in fig. S20-22, and S27-29 were performed in Field II, MATLAB (MathWorks, Natick, MA). The center frequency and the geometry of all elements in each probe were set to be identical. The input excitation voltage (40 V), the single-cycle pulse, and the electromechanical coefficient (0.6) of all

elements were set to be identical as well. The attenuation coefficient of the media (normalized by frequency) was taken as 0.75 $dB \cdot cm^{-1} \cdot MHz^{-1}$ to mimic acoustic properties of human tissues.

Measurement of the interfacial toughness

The interfacial toughness of the elastomer membrane adhered on a dried porcine skin via the bioadhesive layer was measured using the standard 90°-peeling test (ASTM D 2861) with a mechanical testing machine (20 N load cells; Zwick/Roell Z2.5) and 90°-peeling fixture (Test Resources, G50). All tests were performed either in ambient air or in water at room temperature. The dried porcine skin was treated with ethanol to memetic the properties of human epidemic skin. The elastomer (thickness, 40 μm) and bioadhesive (thickness, 10 μm) were prepared with 2.5 cm in width W and 7.5 cm in length L. As a stiff backing for the elastomer membrane, a polycarbonate film was bonded onto the back surface of the elastomer. The resultant sample was tested with the standard 90°-peeling test with a constant peeling speed of 50 mm min^{-1}. The measured peeling force reached a plateau (with slight oscillations), as the peeling process entered a steady state. The interfacial toughness Γ was determined by dividing the plateau force F by the width of the sample W.

Measurement of the attenuation coefficient

The ultrasound attenuation coefficients of the BAUS couplant and various commercial couplants were measured by the transmission-through method in a water tank. Specifically, a broadband emitter transducer (driven by Verasonics Vantage system) was fixed at one end of the water tank. An Onda broadband needle hydrophone (connected with a hydrophone preamplifier and a Picoscope digital oscilloscope) was mounted coaxially as the receiver. The samples were placed perpendicularly to the transducer in a sample-holder between the emitter and the receiver. The transmitted signals through the samples were recorded, and the pure water (without sample) signal was also recorded as a reference. The attenuation coefficient α (in dB/mm) of the sample could be obtained by comparing the amplitude spectrum of the sample signal and the reference water signal,

$$\alpha(\omega) = 20h^{-1}\log_{10}[A_{\text{water}}(\omega)/A_{\text{sample}}(\omega)] \quad (7)$$

where α (in dB/mm) is the attenuation coefficient of the sample, h is the thickness of the sample, $A_{\text{water}}(\omega)$ is the amplitude spectrum of the reference water, and $A_{\text{sample}}(\omega)$ is the amplitude spectrum of the sample.

Fabrication and optimization of the matching layer

The matching layer for the BAUS probe was constructed by doping epoxy (EPO-TEK 301) with cerium dioxide nanoparticles (particle size 10 nm, Sigma-Aldrich) in ethanol (cerium dioxide weight ratio in epoxy from 0% to 80%). The matching layer provided the required acoustic impedance gradient, which is essential for the acoustic wave from the transducer to smoothly penetrate into the skin and for the reflected acoustic waves (the returning echo) to smoothly return to the transducer for imaging.

According to the Krimholtz-Leedom-Matthaei (KLM) model, the theoretical 100% transmission of a sinusoidal acoustic wave is shown to occur when the matching layer thickness approaches ¼ λ_m, where λ_m is the acoustic wavelength in the matching layer. Further based on the KLM model, the acoustic impedance of the matching layer material Z_m is

$$Z_m = (Z_p Z_l)^{1/2} \tag{8}$$

where Z_p and Z_l are the acoustic impedances of the piezoelectric material and the loading medium, respectively. The 1-3 composite piezoelectric material we adopt in this paper has an acoustic impedance of 18 MRayl and the skin (the loading media) has an acoustic impedance of 1.62 MRayl. Based on Eq. 8, we can calculate Z_m=5.4 MRayl, which can be realized by doping 15 wt. % cerium dioxide nanoparticles into epoxy. The acoustic wavelengths (λ_m) of 3 MHz, 7 MHz, and 10 MHz ultrasound waves in the matching layer with Z_m=5.4 MRayl are 412.4 μm, 235.6 μm, and 165.2 μm, respectively. Therefore, the optimized thicknesses of the matching layers (¼ λ_m) for 3 MHz, 7 MHz, and 10 MHz BAUS probes are 103.1 μm, 58.9 μm, and 41.3 μm, respectively.

Fabrication and optimization of the backing layer

The backing layer for the BAUS probe can give mechanical support to the elements inside the probe that will generate high-frequency vibrations. The backing layer also has strong attenuation of the ultrasound wave to effectively shorten the pulse duration and thus increase the imaging resolution.

To optimize the composition of the backing layer, we constructed the transducers with backing layers of different compositions of epoxy (EPO-TEK 301) with tungsten powder (particle size 1 um, Sigma-Aldrich). A composition of 8:1 (epoxy to tungsten powder, weight ratio) gave the optimized acoustic properties. The BAUS probe with the optimized backing layer showed a decent increase in signal quality, including shorter pulse length and higher signal-to-noise ratio (40 dB) (fig. S6).

To optimize the thickness of the backing layer, we then used the KLM model to calculate the pulse-echo excitation response of the BAUS probe with the optimized matching layer. From the KLM model calculation, we found that increasing the backing layer thickness from 1 mm to 2 mm can shorten the spatial pulse length (fig. S6A, fig. S6B). However, further increasing the backing layer thickness from 2 mm to 4 mm will not decrease the spatial pulse length (fig. S6B, fig. S6C). The experimental results (fig. S6D-F) are consistent with the KLM models' results. Therefore, we chose an optimized thickness of 2mm for the backing layers of our BAUS probes.

Determination of imaging resolutions

Axial resolution:

To evaluate the axial resolutions of the BAUS probes, we used the pulse-echo tests to characterize the spatial pulse lengths (SPL) of 3 MHz, 7 MHz, and 10 MHz BAUS probes. From the pulse-echo results (Fig. S19), we can derive the spatial pulse lengths of the 3 MHz, 7 MHz, and 10 MHz BAUS probes to be 1.54, 0.55, and 0.385 mm, respectively. Their axial resolutions can be calculated as SPL/2.

The axial resolution of the stretchable ultrasound imaging probe was reported to be 5.775 mm at the frequency of 2 MHz *(12)*. Since other wearable ultrasound imaging devices *(14-18)* did not report their axial resolutions, we first calculated their acoustic wavelengths in the tissue based on their frequencies. Then the SPL was estimated as the acoustic wavelengths multiplied by the pulse-cycle number, which is 2 to 4 for common ultrasound imaging probes. Taking the pulse-cycle number as 3, we can approximately estimate the axial resolutions of these wearable ultrasound devices.

Lateral resolution:

To evaluate the lateral resolutions of the BAUS probes, we used the probes to image a standard imaging phantom (fig. S20, S21, and S22). The phantom contains standard thin wire reflectors (200 μm diameter) distributed at various depths. Based on the images of the reflectors, we measured the beamwidths at various depths. The beamwidth gave the lateral resolution of the BAUS probe at the imaging depth. To validate the experimental results, we performed the corresponding acoustic simulations by Field II platform. The simulation results on the lateral resolutions are consistent with the experimental measurements (fig. S20, S21, and S22). Other wearable ultrasound imaging devices *(12, 14-18)* did not report their lateral resolutions.

Imaging mode and data acquisition of the BAUS system

Radio-frequency signals received by the BAUS probe were post-processed by the Vantage system (Verasonics, Inc). For imaging organs that are within 6 cm beneath the skin including muscle, carotid artery, and jugular vein, we adopted the plane wave compounding method. For imaging organs that are deeper than 6 cm beneath the skin, including heart, lung, diaphragm, and stomach, we adopted the phased array harmonic imaging and spatial compounding algorithms. All imaging algorithms were adapted from the algorithm packages of the Verasonics system. If a commercial ultrasound probe was adopted as the BAUS probe, the signals were post-processed by the corresponding commercial ultrasound machine.

Calculation of blood pressure.

By recording the continuous cross-sectional images of the blood vessel, we can extract its diameter to calculate the blood pressure waveform following a previously reported method *(37)*. The arterial blood pressure waveform $p(t)$ follows,

$$p(t) = p_d \cdot e^{\alpha\left(\frac{A(t)}{A_d}-1\right)} \tag{9}$$

where p_d is the diastolic pressure, A_d is the diastolic cross-sectional area of the artery, $A(t)$ is the cross-sectional area of the artery as a function of time t, α is the rigidity coefficient, and t is the time. Assuming that the artery is rotationally symmetrical, $A(t)$ can be calculated as,

$$A(t) = \frac{\pi d^2(t)}{4} \tag{10}$$

where $d(t)$ is the diameter of the artery as a function of time t.

We assume the human blood vessel is elastic with negligible viscoelasticity, so that the pressure-diameter curve has a moderate hysteresis, below 0.2%. This is suitable for subjects with normal local vascular conditions or with slight local atherosclerosis. In this situation, the diameter of the vessel will not lag behind the pressure waveforms. And the equation above can be used to reconstruct the blood-pressure waveforms from the vessel-diameter waveforms.

The rigidity coefficient α can be calculated by,

$$\alpha = \frac{A_d \ln(p_s / p_d)}{A_s - A_d} \tag{11}$$

where A_s is the systolic cross-sectional area of the artery and p_s is the systolic pressure which can be measured by a commercial blood pressure cuff. Using the aforementioned equations (Eq. 9-11), the pressure waveform $p(t)$ can be achieved after a brief calibration for α and p_d.

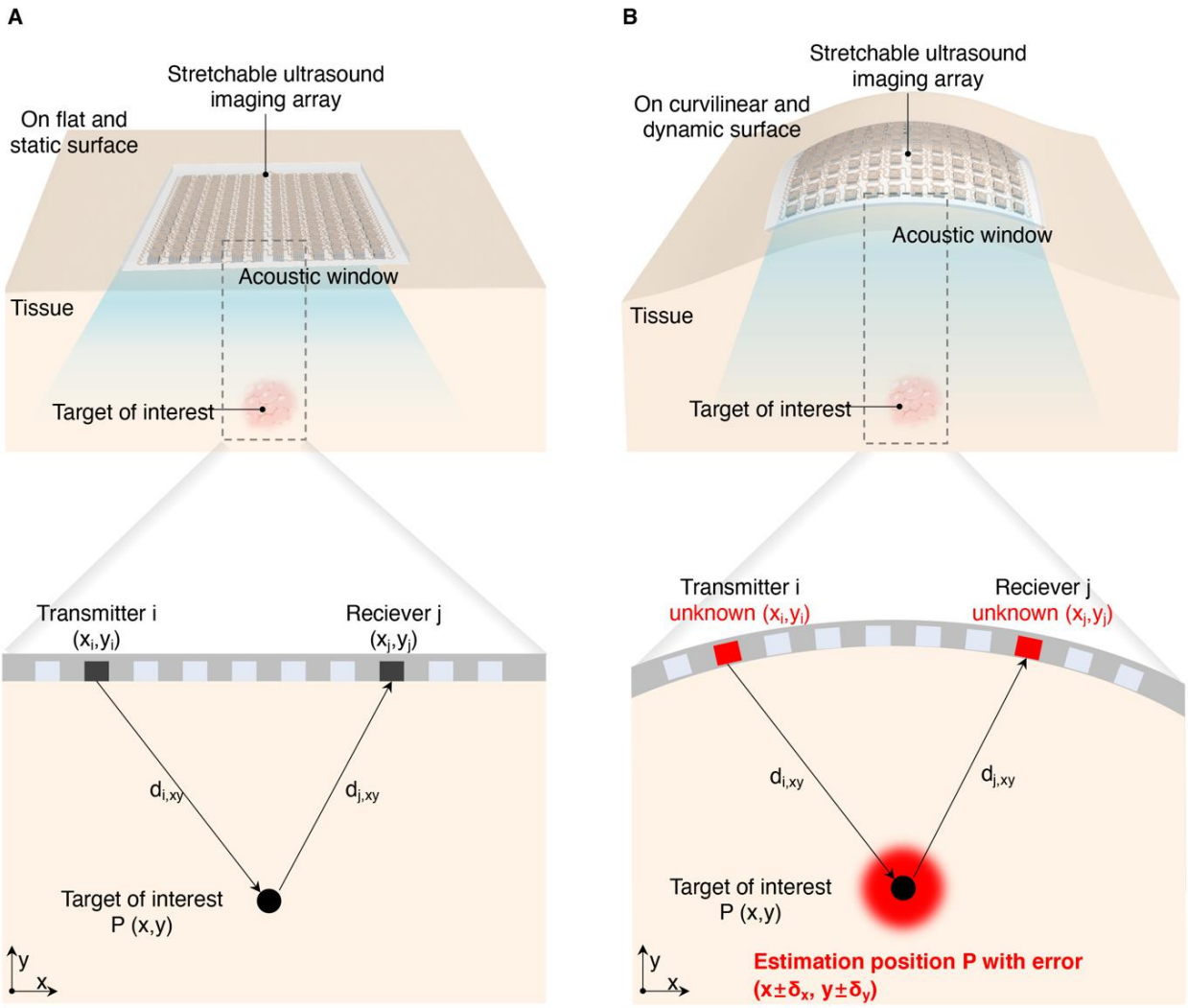

Fig. S1.

Intrinsic limitation on the imaging resolution and stability of stretchable ultrasound devices. A. Stretchable ultrasound array on a static and flat surface. When the relative positions of the transmitter (x_i, y_i) and the receiver (x_j, y_j) are on a flat geometry, the spatial location of the target of interest *P* (x, y) can be calculated based on the signal received accurately. B. Stretchable ultrasound array on a curvilinear surface. The unknown profile of the skin creates unpredictable disturbance to the relative positions of the transmitter (x_i, y_i) and the receiver (x_j, y_j), making them into unknown parameters. In addition, dynamic body motions can cause skin deformation, further exacerbating the disturbance of the relative positions of the transmitter and the receiver. Because there is no practical way to calculate the transmitter and receiver locations in real-time, image reconstruction must assume that the transmitter and receiver are fixed at static locations, causing errors in image reconstruction for the target of interest *P* ($x\pm\delta_x$, $y\pm\delta_y$) where δ denotes error.

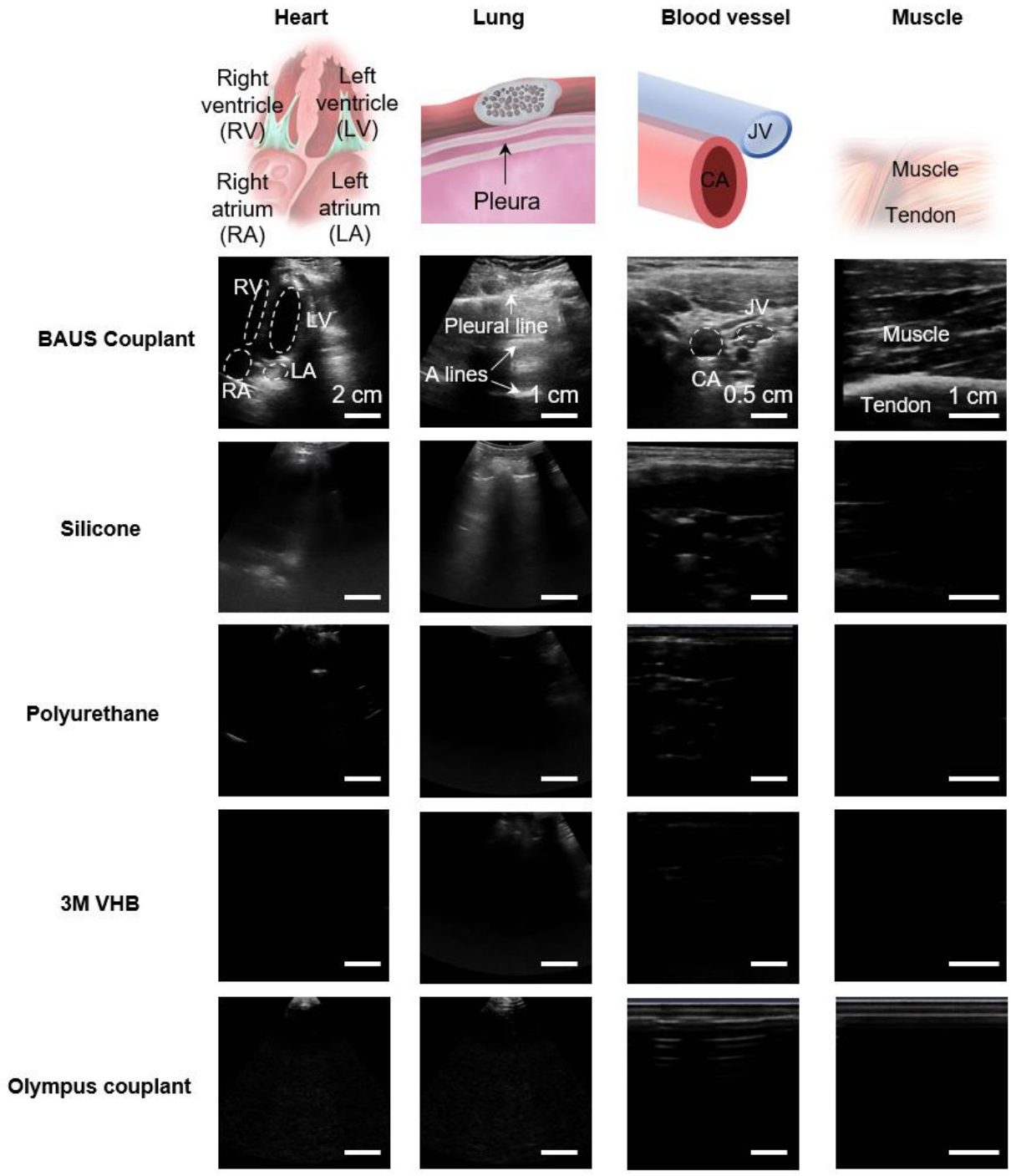

Fig. S2.

Comparison of imaging performances of the BAUS couplant and typical elastomer couplants on the market including silicone (Ecoflex, Smooth-On), polyurethane (Sigma-Aldrich), acrylic tape (VHB, 3M), and Aqualene (Olympus).

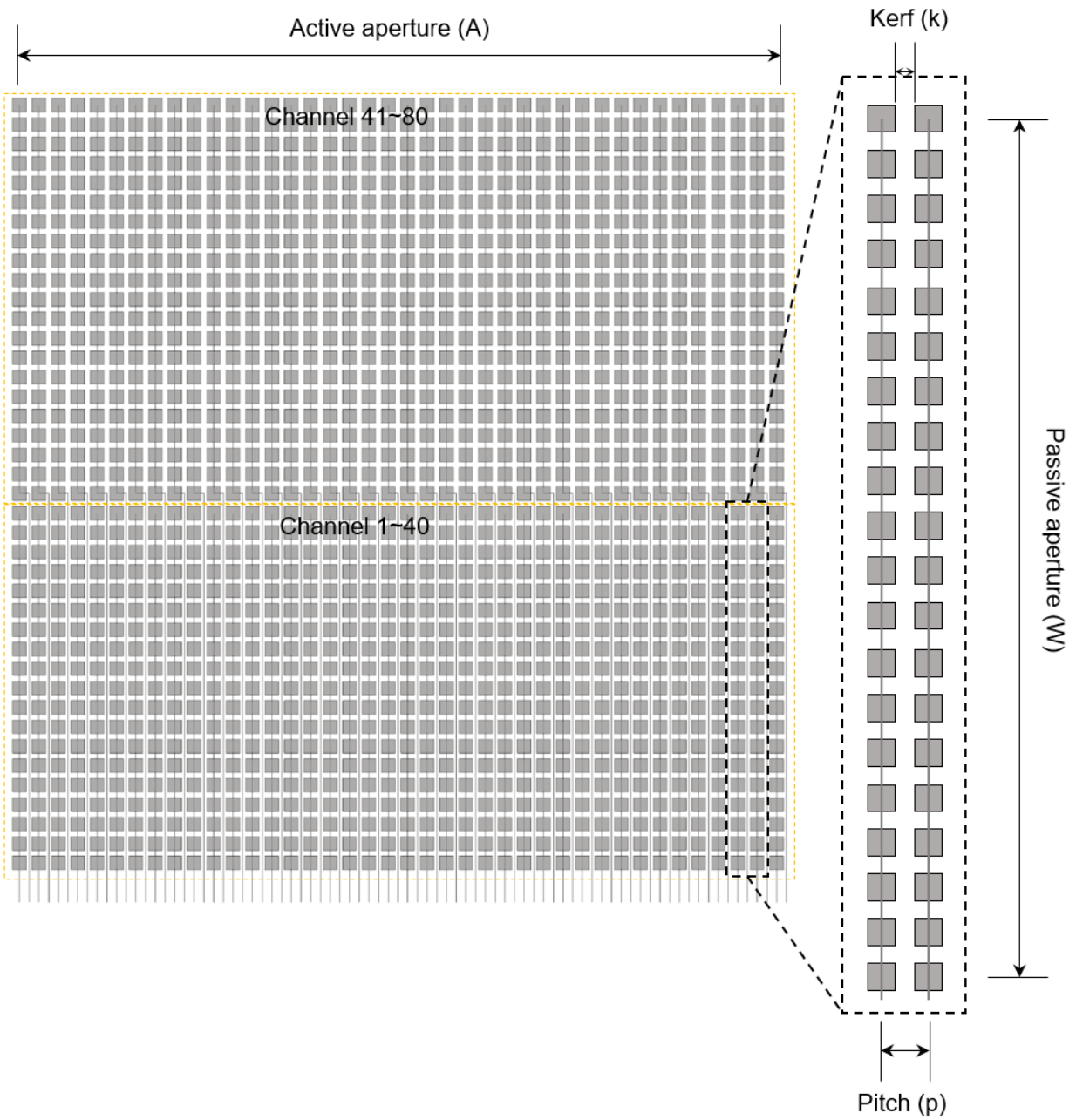

Fig. S3.

Illustration of the design of the BAUS probes. See table S3 for design specifications of 3 MHz, 7 MHz, and 10 MHz BAUS probes.

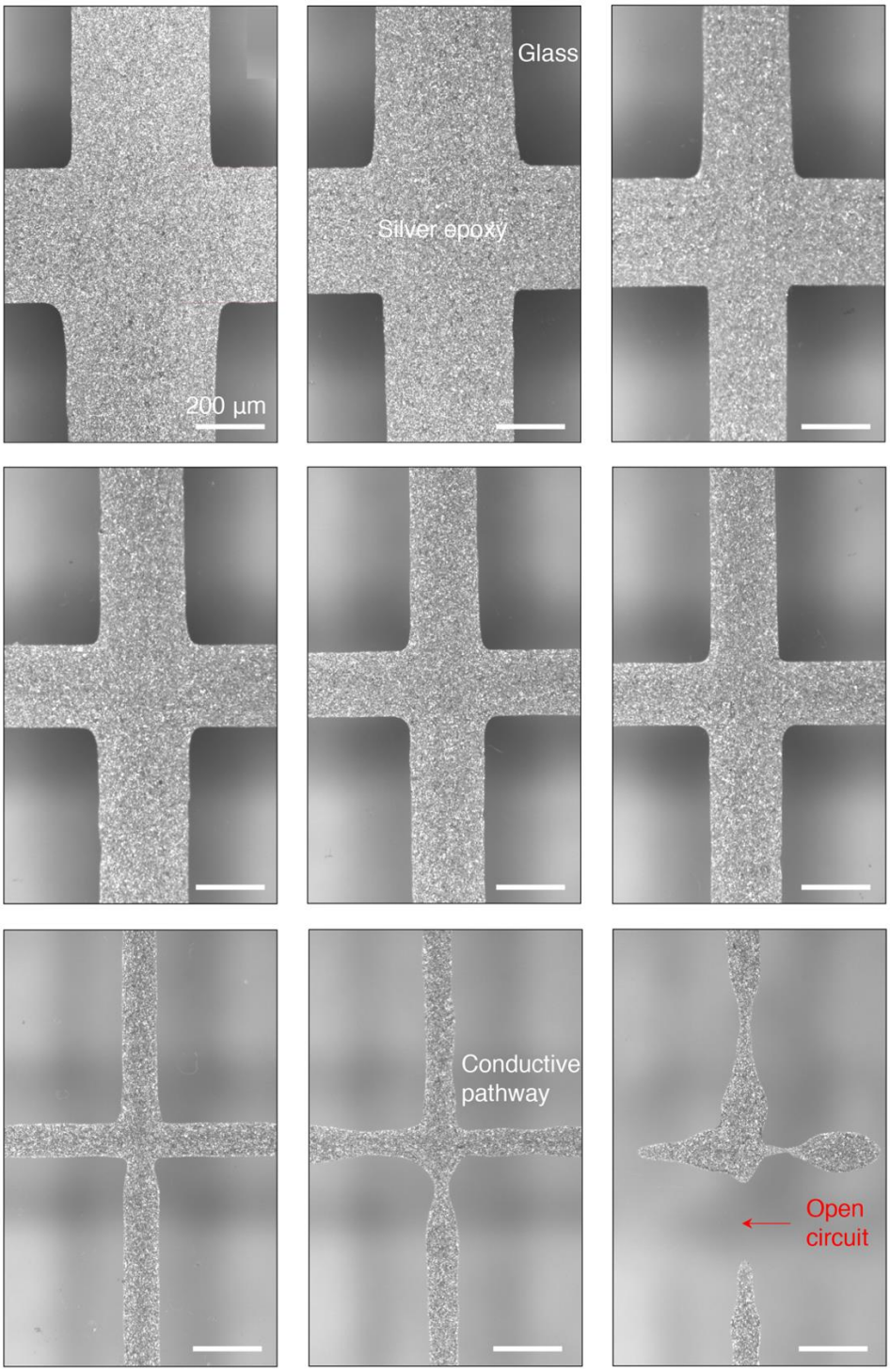

Fig. S4.

Resolution limit of 3D-printed circuits. From the upper left image to the bottom right image, we gradually decreased the printed circuit-line width. Only the finest one (bottom right image) appear an open circuit in the printing trajectory. The resolution of the printed circuit line can reach 100 µm. Scale bar, 200 µm.

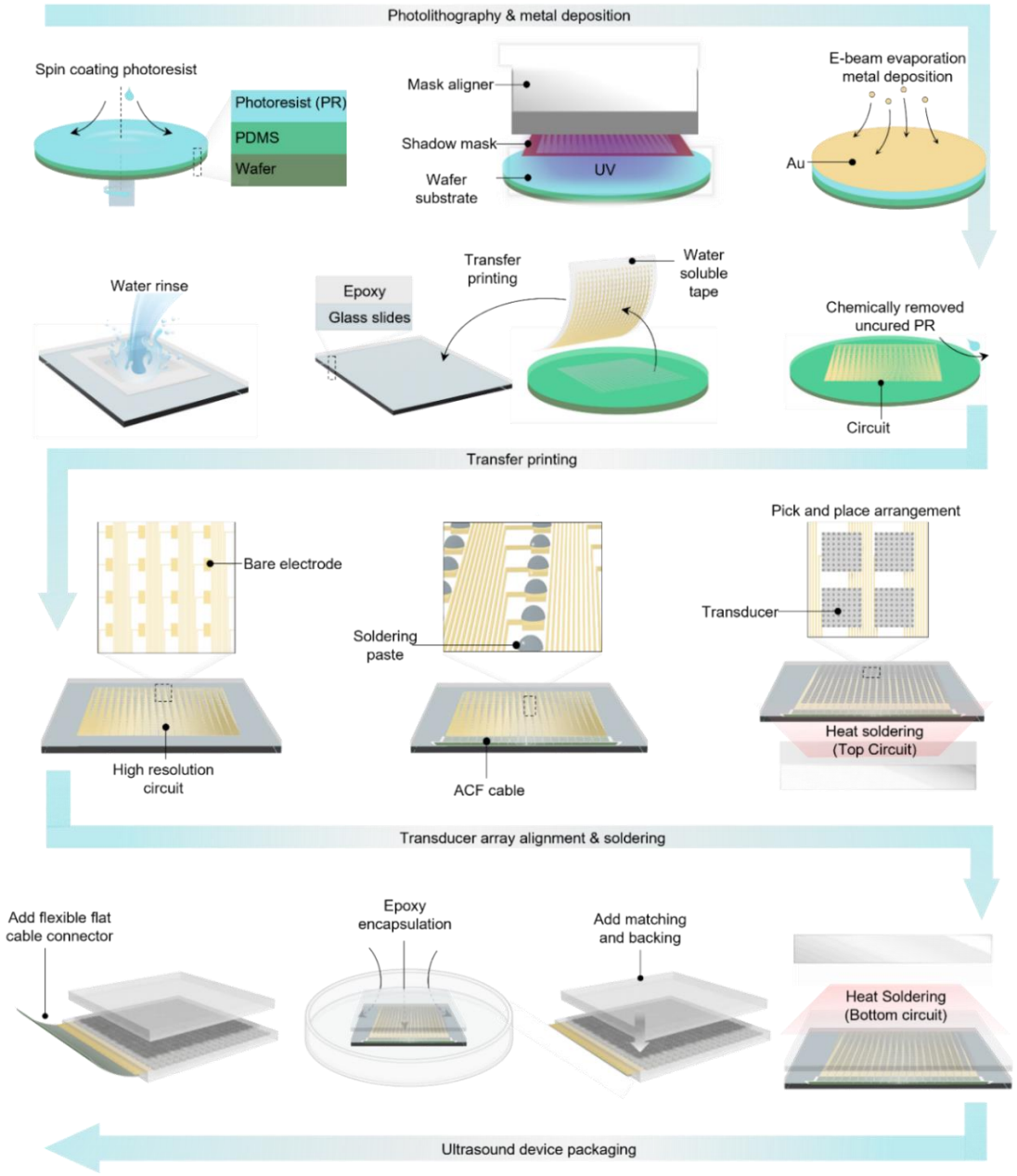

Fig. S5.

Fabrication of the top and bottom circuits by photolithography and full device assembly. For high-resolution circuit fabrication, we performed photolithography by using mask aligner followed by E-beam evaporator for metal deposition. Then we performed transfer printing of the high-resolution circuit to an epoxy substrate. Next we applied soldering paste to each bare electrode on the circuit for bonding to individual elements, and then we performed the soldering process by heating (150° C for 5 minutes). After each element was fully bonded on the circuits, we added backing and matching layers on the top and bottom circuits with spin coating. The resultant probe was encapsulated by epoxy to increase device robustness. As the final step, we added a flexible flat cable connector to the device.

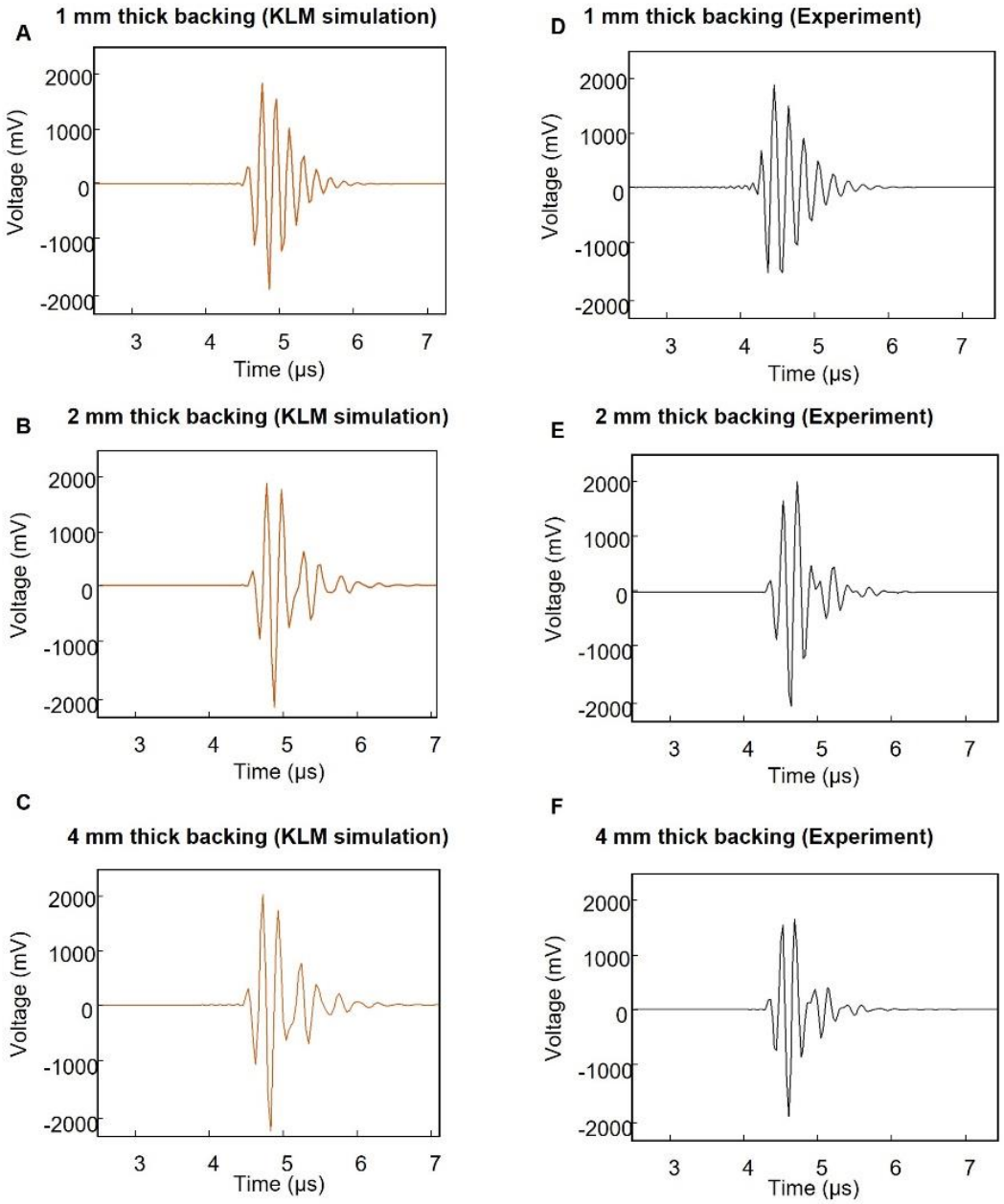

Fig. S6.

Krimholtz-Leedom-Matthaei (KLM) simulation and pulse-echo tests for optimizing the backing layer on the BAUS probe (3 MHz). A. KLM simulation of pulse-echo of the BAUS probe with 1-mm backing layer. B. KLM simulation of pulse-echo of the BAUS probe with 2-mm backing layer. C. KLM simulation of pulse-echo of the BAUS probe with 4-mm backing layer. D. Experimental measurement of pulse-echo from the BAUS probe with 1-mm backing layer. E. Experimental measurement of pulse-echo from the BAUS probe with 2-mm backing layer. F. Experimental measurement of pulse-echo from the BAUS probe with 4-mm backing layer. Note an aluminum block was used as the reflector.

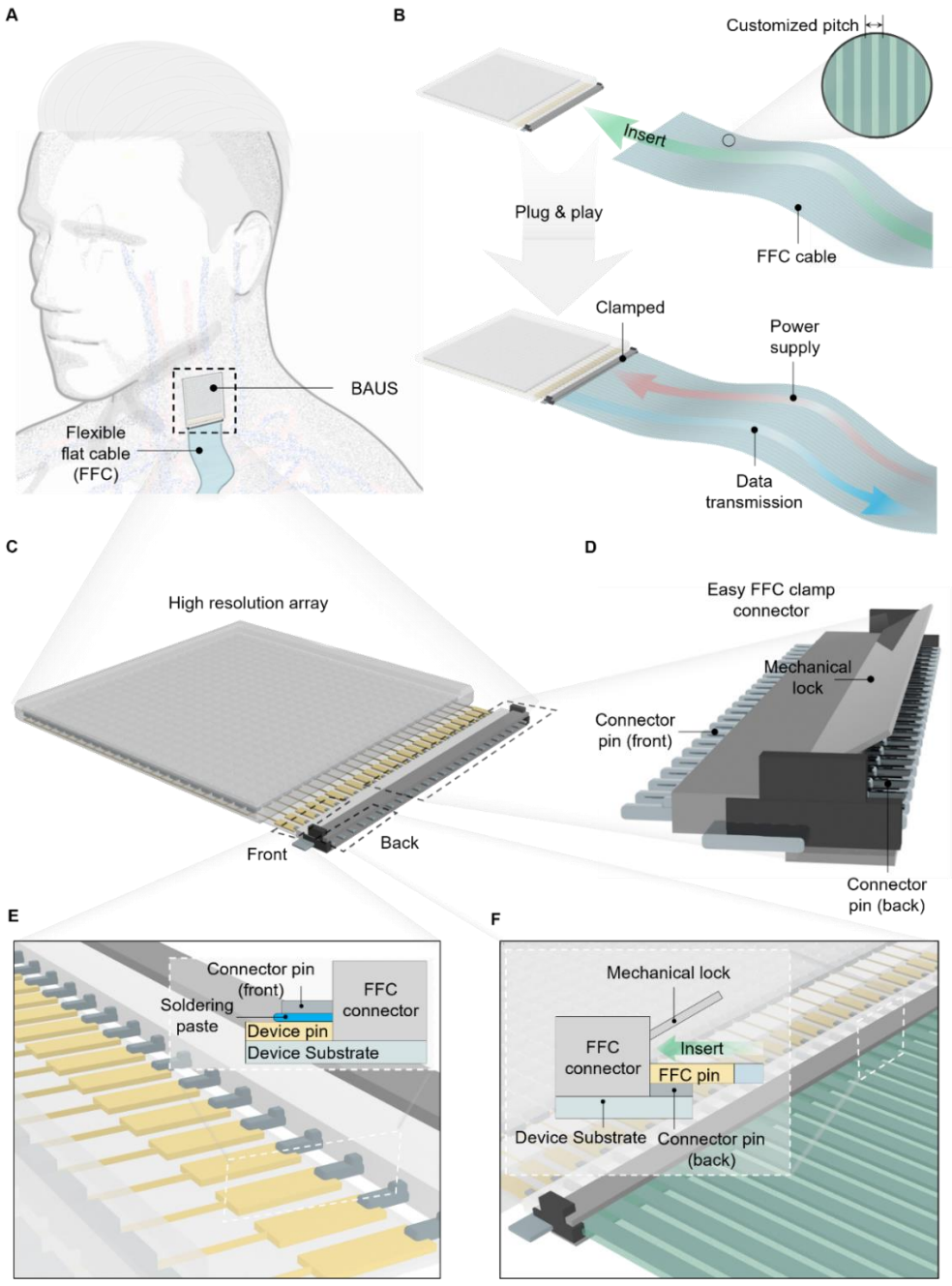

Fig. S7.

Plug & play design for the BAUS device. A. The input and output (I/O) allows for immediate usage of the BAUS probe after plugging in the flexible flat cable (FFC). B. The FFC can easily insert the connector for power supply and data transmission. C. Schematics for the whole device containing the BAUS probe and the FFC connector. D. 3D view of the FFC connector, which contains front pins to interface with the transducer and back pins to connect with the FFC. The mechanical lock can fix the FFC after plugged in. E. Front view of the FFC connector and transducer interface. The insert schematics show the side view of the connection. F. Back view of the FFC connector pin to the FFC. The insert schematics show the side view of the connection.

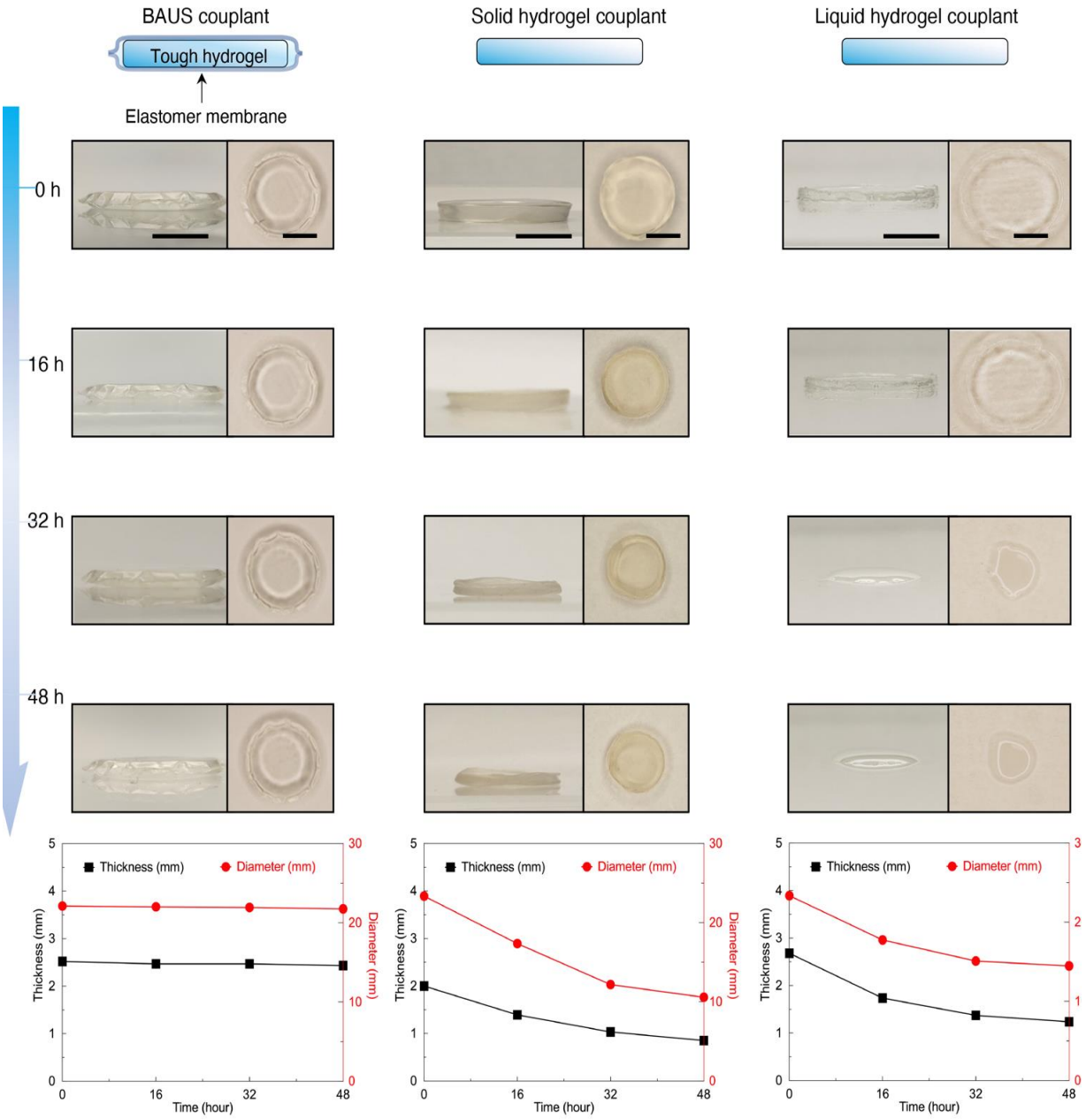

Fig. S8.

Comparison of anti-dehydration performances of the BAUS couplant, liquid hydrogel couplant (Aquasonic Clear, Parker Labs), and solid hydrogel couplant (Aquaflex, Parker Labs). All samples are stored in the ambient environment (relative humidity, 30-50%; temperature, 24°C) for 48 hours. The BAUS couplant shows negligible changes of its thickness or diameter, indicating almost no dehydration. Both the liquid hydrogel couplant and the solid hydrogel couplant shrink their dimensions substantially, indicating severe dehydration. Scale bar, 10 mm.

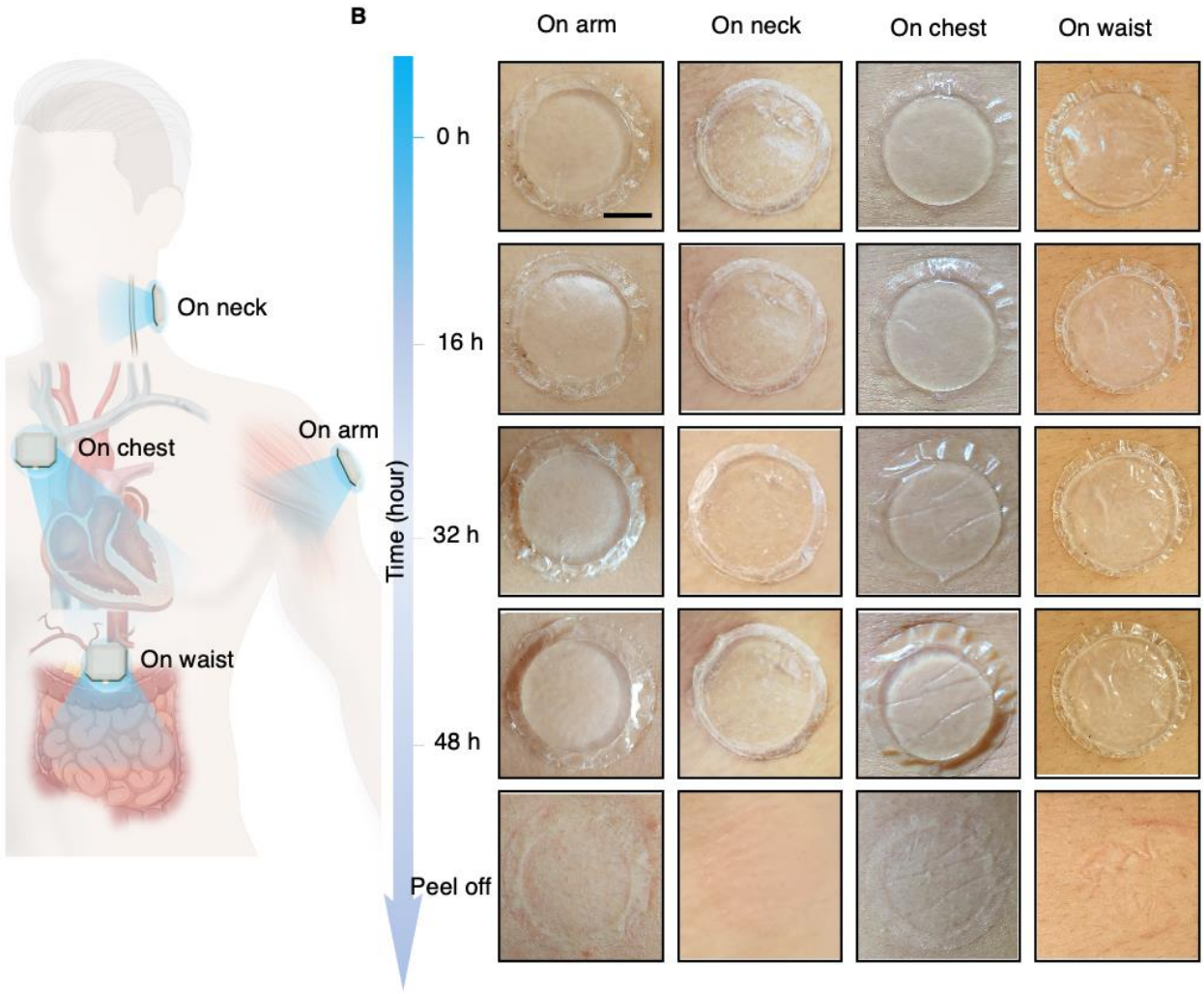

Fig. S9.

Stable adhesion of the BAUS couplant on the skin over 48 hours. A. Schematic illustration of stable adhesion of the bioadhesive couplant on various locations on the body (arm, neck, chest, waist). B. Photos of stable adhesion of the bioadhesive couplant on various locations on the body (arm, neck, chest, waist) over 48 hours (relative humidity, 30-50%; temperature, 24°C). Scale bar, 10 mm.

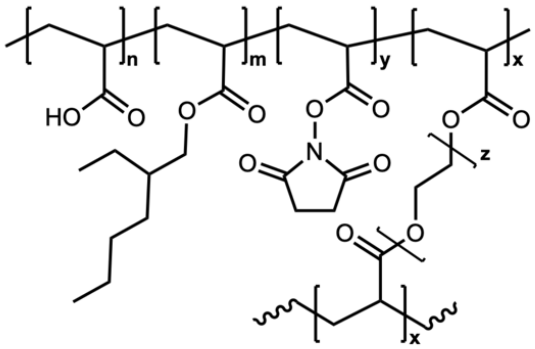

Fig. S10.
Chemical structure of the bioadhesive layer in the BAUS couplant.

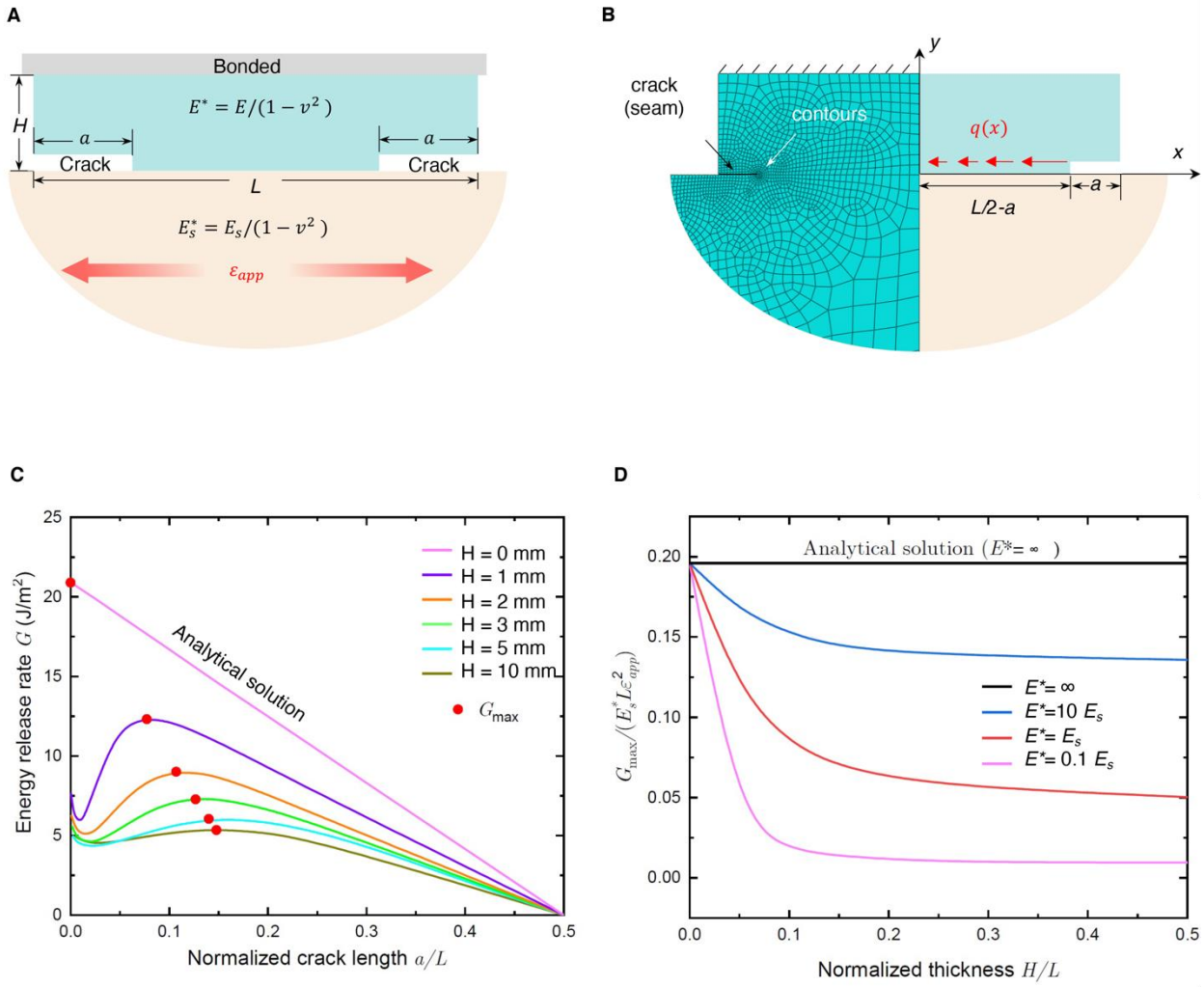

Fig. S11.

Mechanical modeling of the couplant-skin system. A. Schematic illustration of the parameters in the mechanical model. B. The mechanical simulation adopts a symmetric model about the y-axis. Finite element simulations are conducted using the commercial package Abaqus/standard. C. Energy release rate G versus normalized crack length (a/L) of various couplant thicknesses. D. Normalized maximum energy release rate $G_{\max}/\left(E_s^* L\varepsilon_{app}^2\right)$ versus normalized thickness H/L under various E^*/E_s^*.

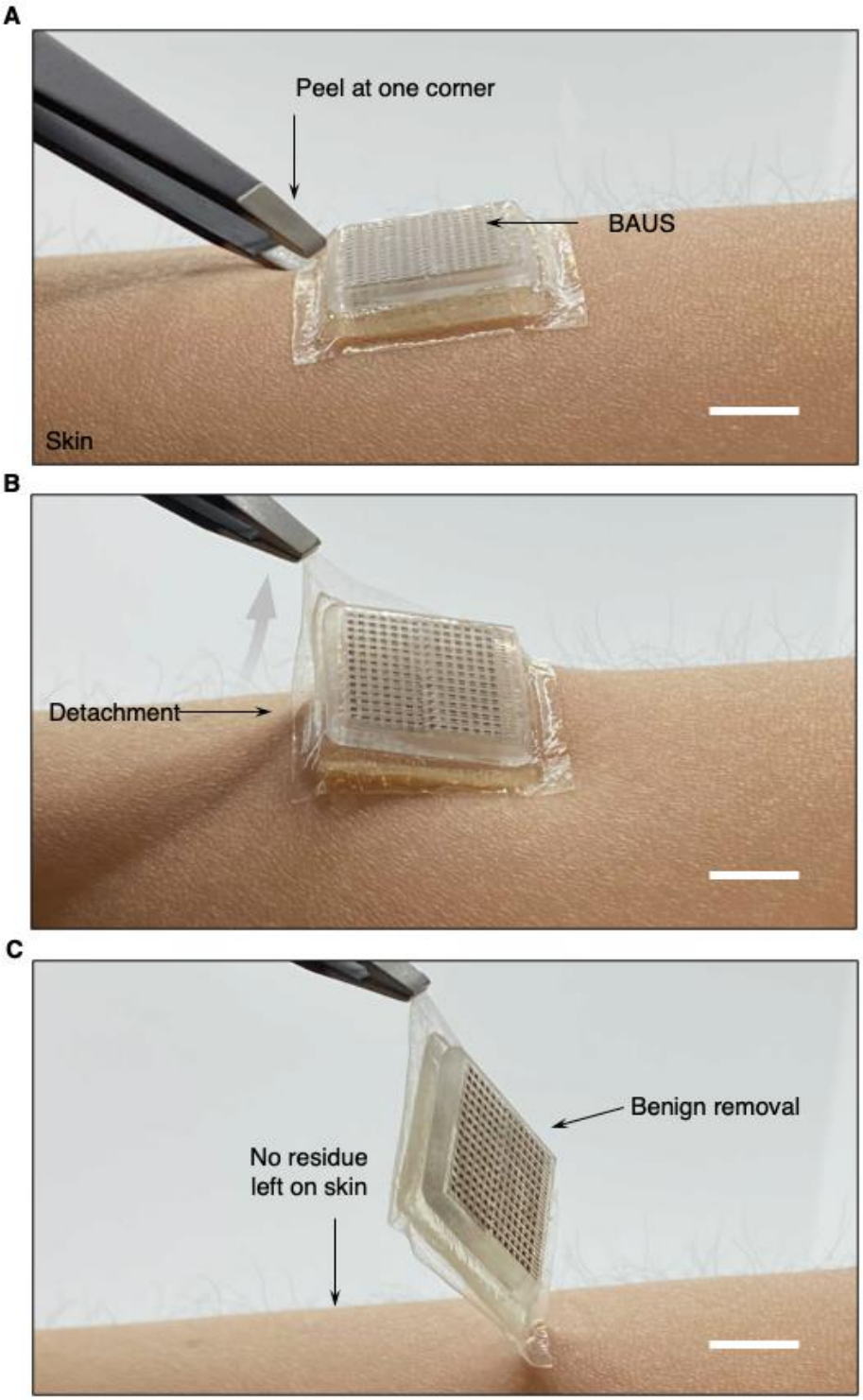

Fig. S12.

Benign detachment of the BAUS device from the skin. A. The detachment can be initiated anytime by peeling from one corner of the BAUS couplant. B. Detachment process. C. No residue is left on the skin after the removal of the BAUS device. Scale bar, 10 mm.

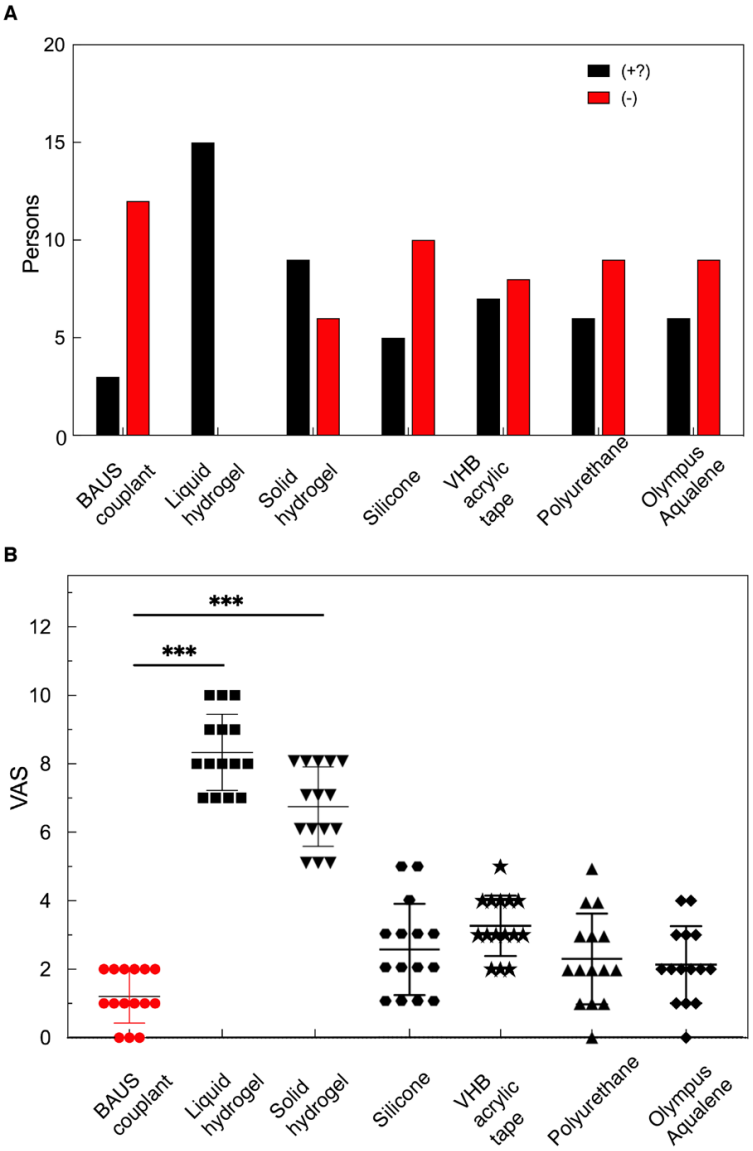

Fig. S13.

Comparison of 48-hour wearing comfort of the BAUS couplant, typical liquid (Aquasonic Clear, Parker Labs) and solid (Aquaflex, Parker Labs) hydrogel couplants, and elastomer couplants including silicone (Ecoflex, Smooth-On), acrylic tape (VHB, 3M), polyurethane (Sigma-Aldrich), and Aqualene (Olympus) on the market. A. wearing comfort tests. Evaluations for different couplants according to the patch test criteria of the International Contact Dermatitis Research Group (ICDRG). '+?' and '−' stand for doubtful positive reaction and negative reaction, respectively. B. Participants reported their feelings of discomfort while the couplants were attached to the skin. The feelings were then evaluated by the visual analogue scale (VAS), ranging from 0 (most comfortable) –10 (most uncomfortable). Error bar values represent the mean +/- SD (n = 15 independent samples). Statistical significance and P values are determined by one-way ANOVA followed by Tukey's multiple comparison test; ***P⩽ 0.001.

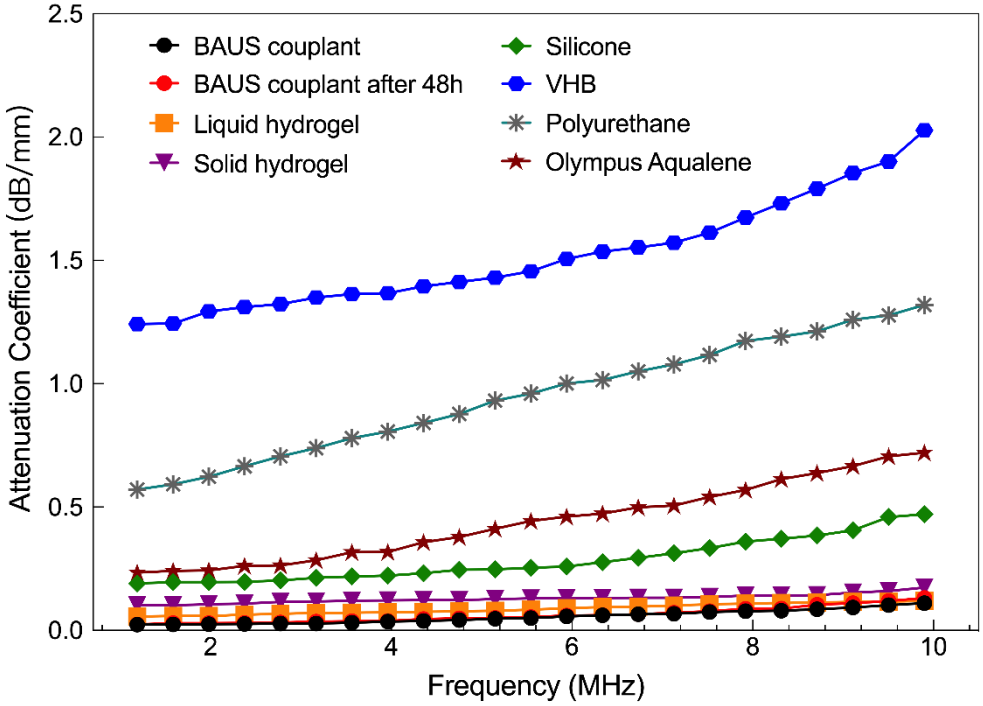

Fig. S14.

Comparison of attenuation coefficients of the BAUS couplant and typical couplants on the market. Attenuation coefficients of the BAUS couplant, typical liquid (Aquasonic Clear, Parker Labs) and solid (Aquaflex, Parker Labs) hydrogel couplants, and elastomer couplants including silicone (Ecoflex, Smooth-On), acrylic tape (VHB, 3M), polyurethane (Sigma-Aldrich), and Aqualene (Olympus) on the market.

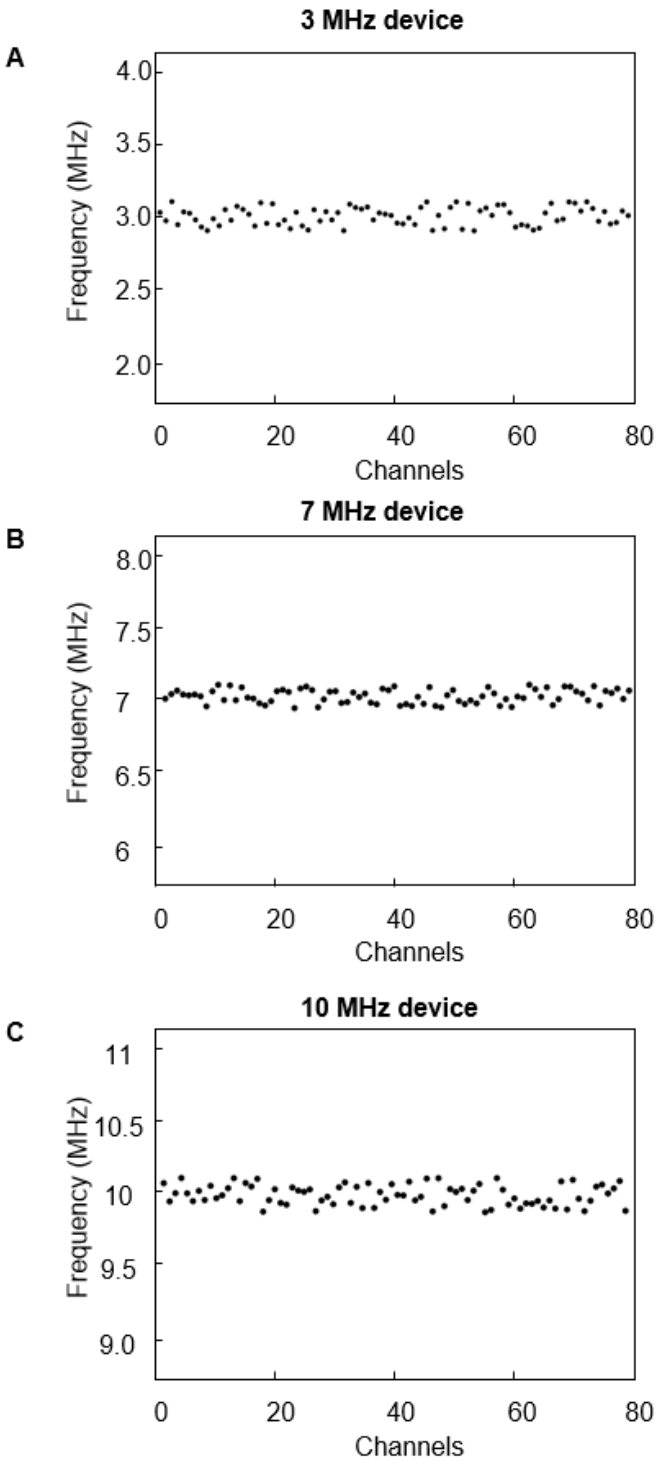

Fig. S15.

Center frequency distribution characterization of the BAUS probes. A. 80 elements (channels) of 3 MHz probe. B. 80 elements (channels) of 7 MHz probe. C. 80 elements (channels) of 10 MHz probe.

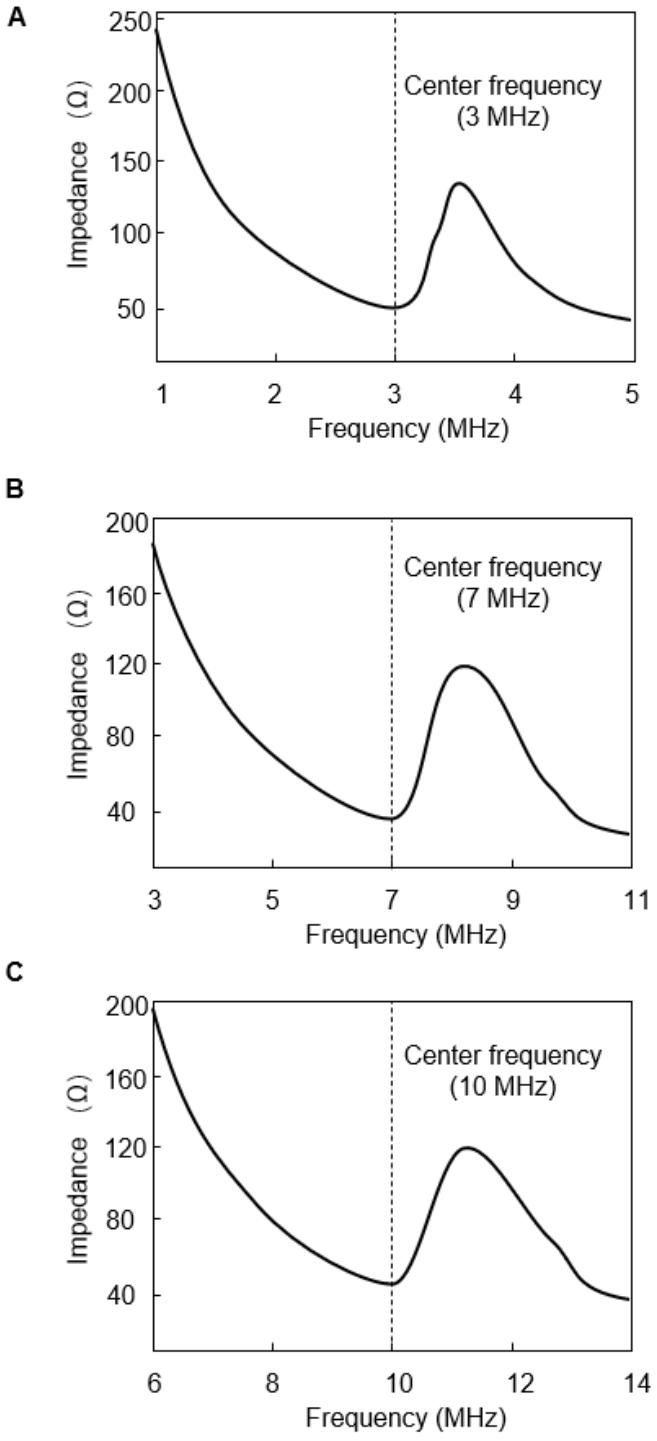

Fig. S16.

Electrical impedance characterization of the BAUS probes. A. Impedance spectrum of 3 MHz BAUS probe. B. Impedance spectrum of 7 MHz probe. C. Impedance spectrum of 10 MHz probe.

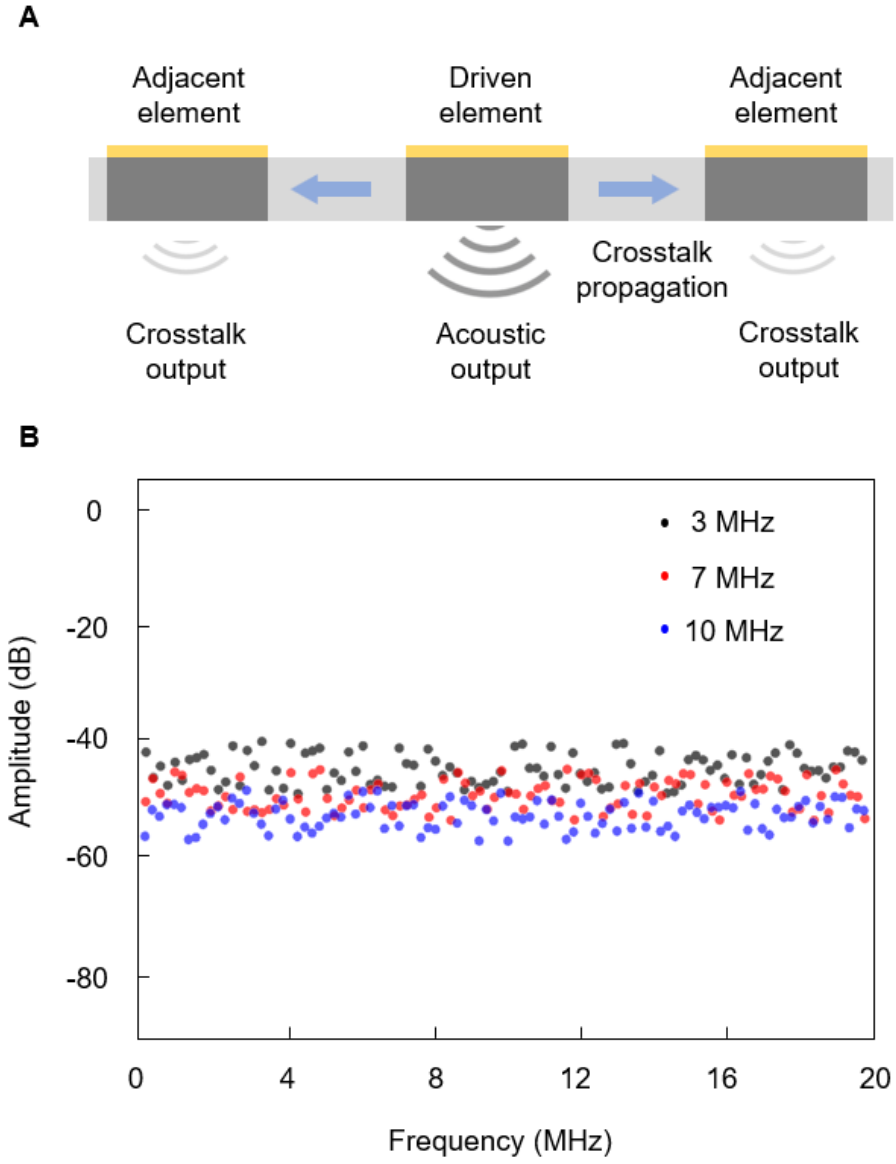

Fig. S17.
Crosstalk measurement of the BAUS probes. A. schematic illustration of the crosstalk-characterization setup. B. Measurement results for 3 MHz, 7 MHz, and 10 MHz BAUS probes.

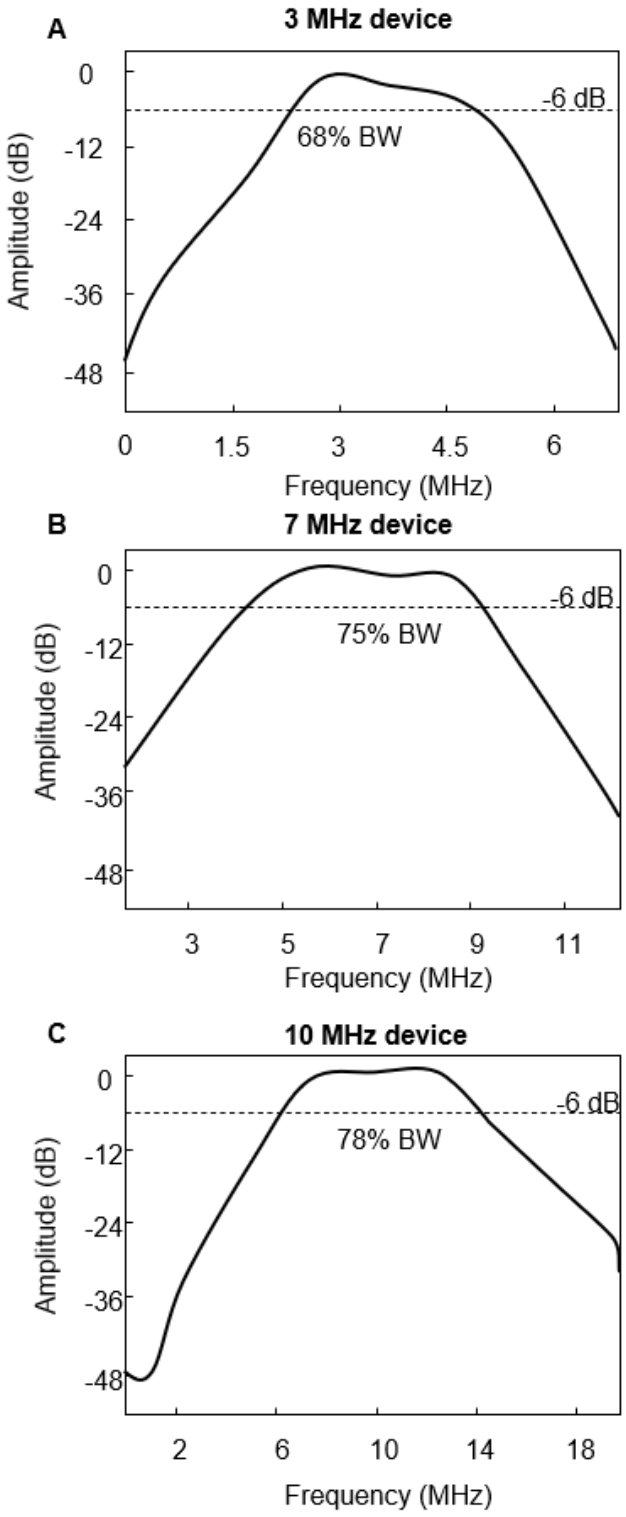

Fig. S18.

Experimentally measured pulse bandwidths of the BAUS probes. A. 3 MHz BAUS probe. B. 7 MHz BAUS probe. C. 10 MHz BAUS probe. The bandwidth results are from Fast Fourier Transform (FFT) of the pulse-echo test results in Fig. S19.

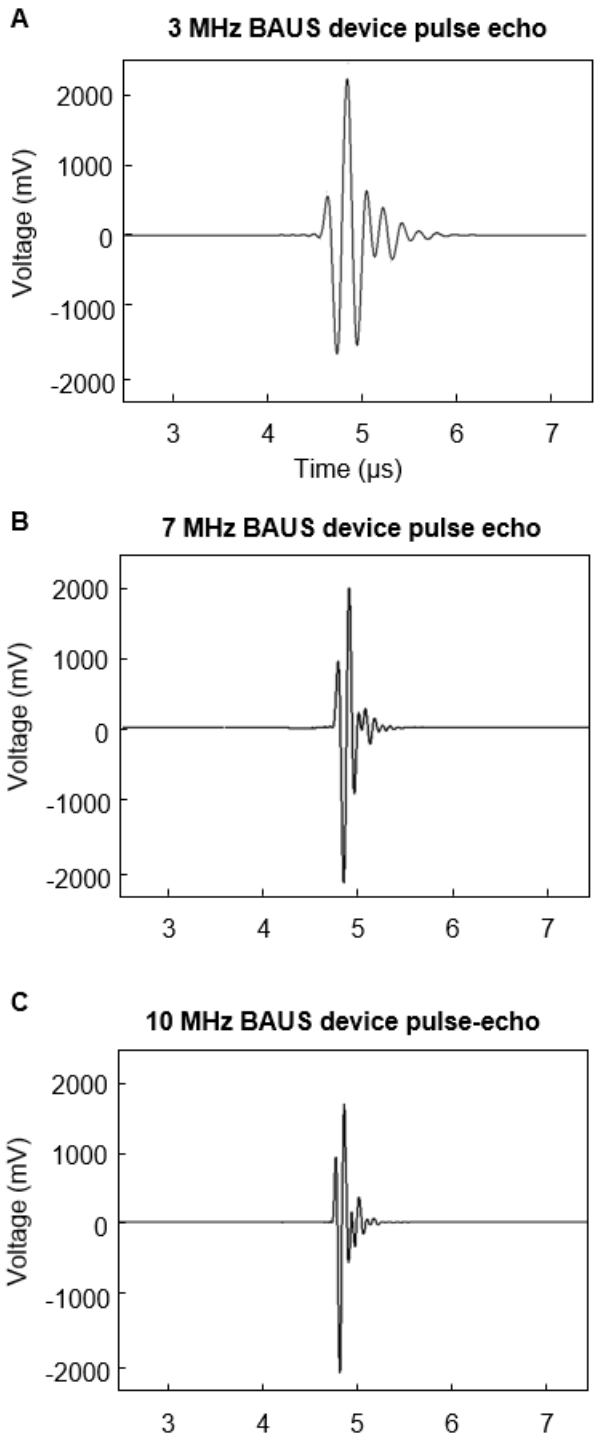

Fig. S19.

Spatial pulse length characterization of the BAUS probes. A. pulse-echo response of 3 MHz BAUS probe. B. pulse-echo response of 7 MHz BAUS probe. C. pulse-echo response of 10 MHz BAUS probe. Note a standard wire phantom was used as the reflector.

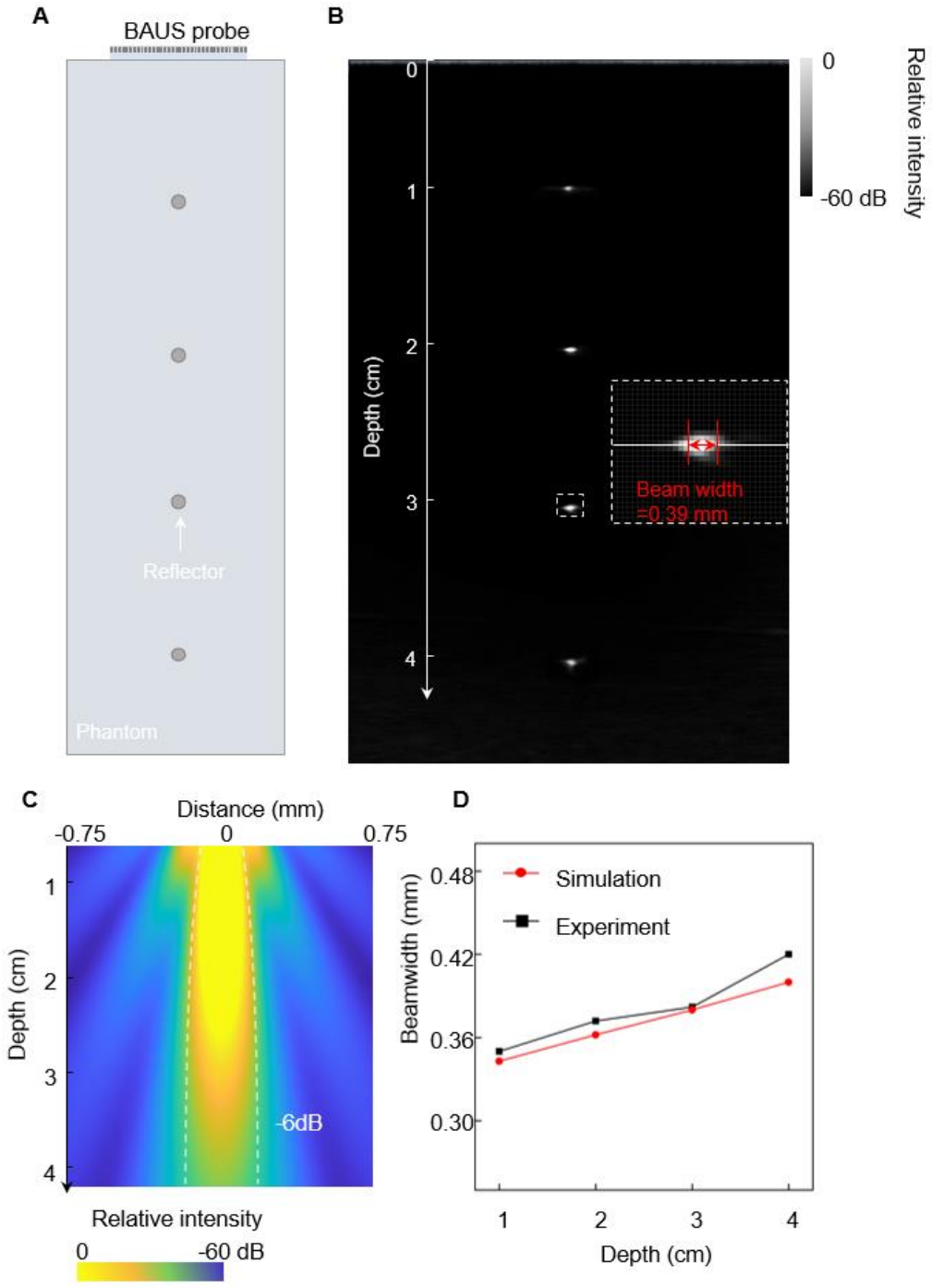

Fig. S20.

Characterization of point spread function (PSF) for the 7 MHz BAUS probe. A. setup of the experiments. B. imaging results from experiments. C. imaging results from simulation. D. comparison of experimental and simulation results.

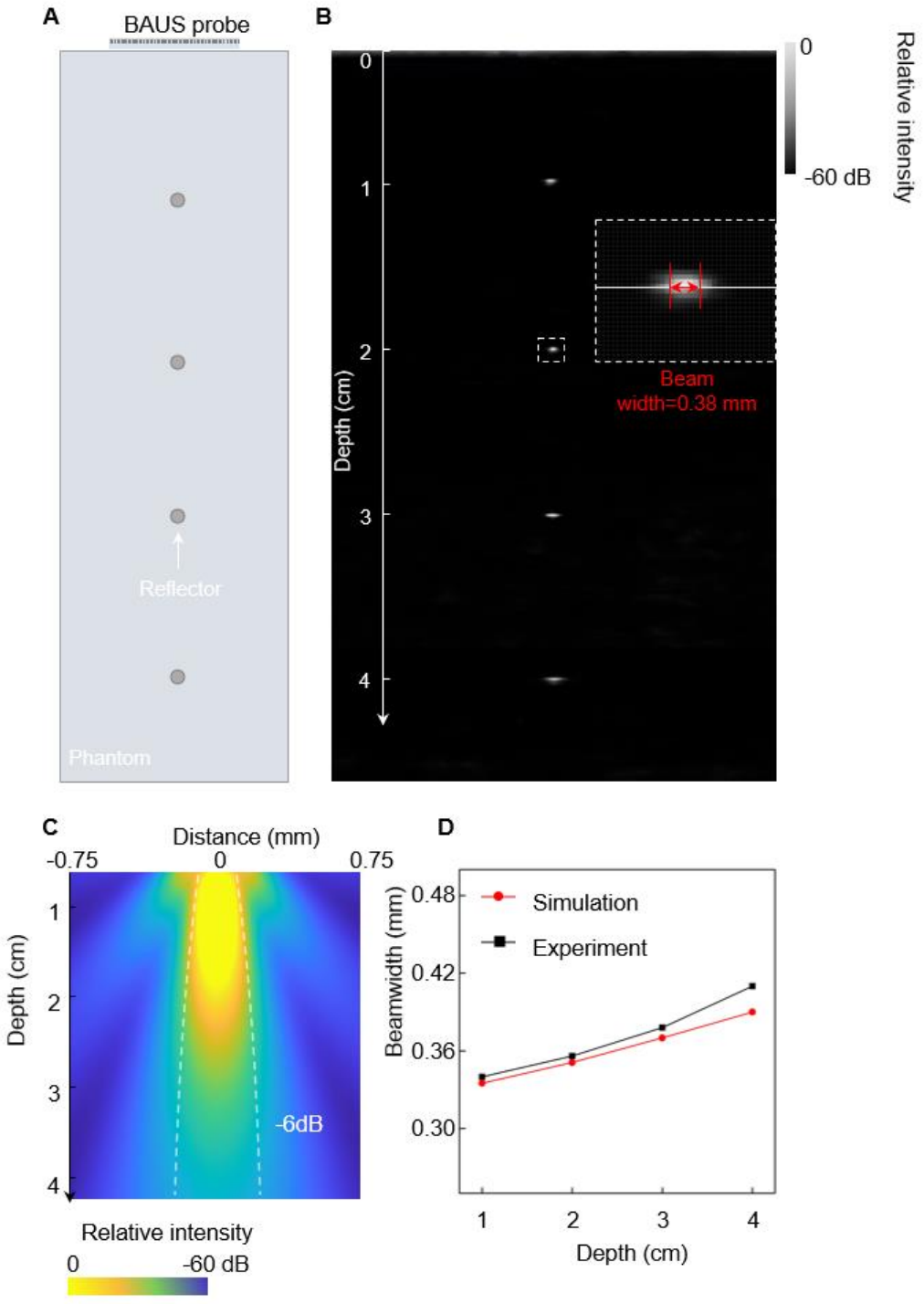

Fig. S21.

Characterization of point spread function (PSF) for the 10 MHz BAUS probe. A. setup of the experiments. B. imaging results from experiments. C. imaging results from simulation. D. comparison of experimental and simulation results.

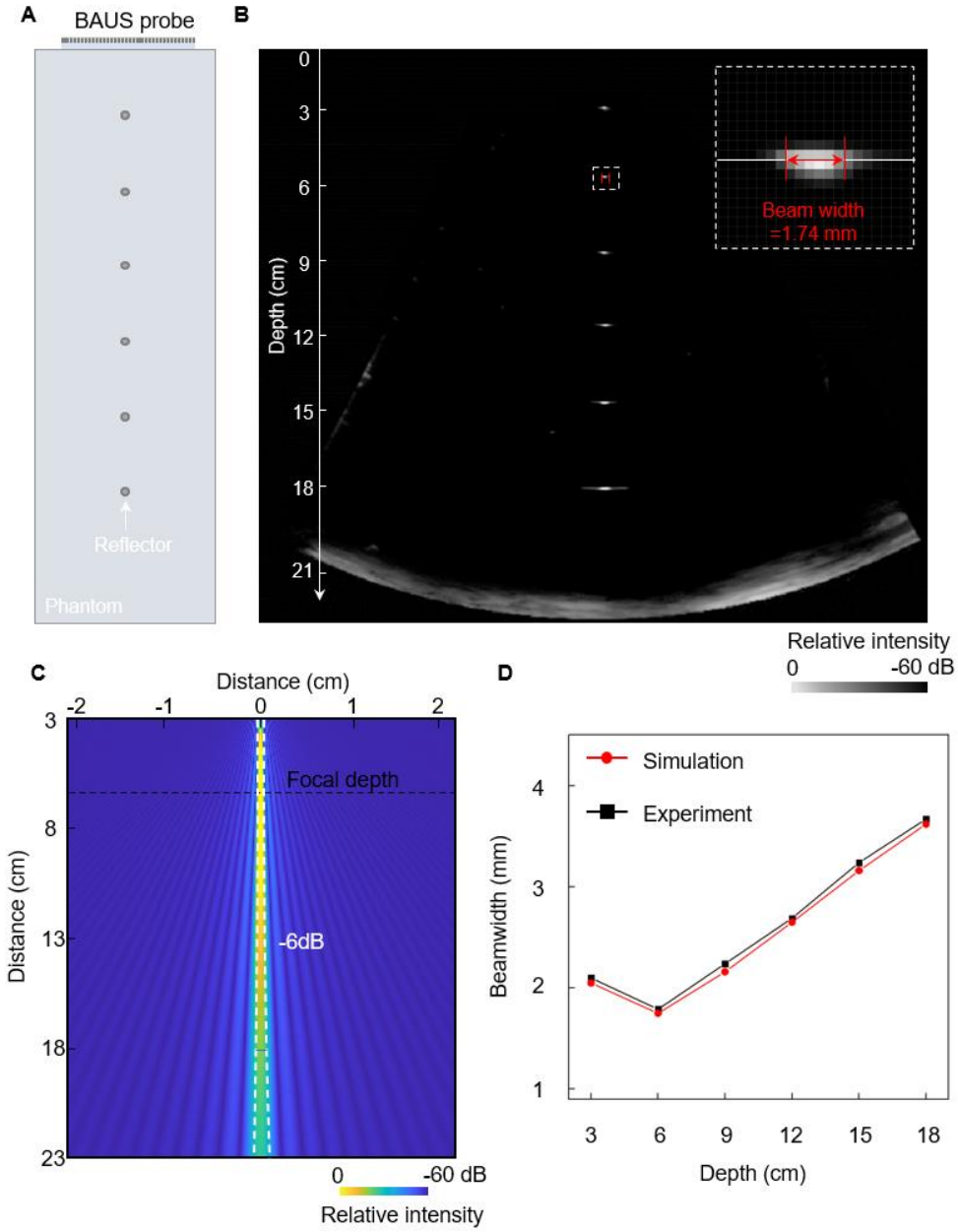

Fig. S22.

Characterization of point spread function (PSF) for the 3 MHz BAUS probe. A. setup of the experiments. B. imaging results from experiments. C. imaging results from simulation. D. comparison of experimental and simulation results.

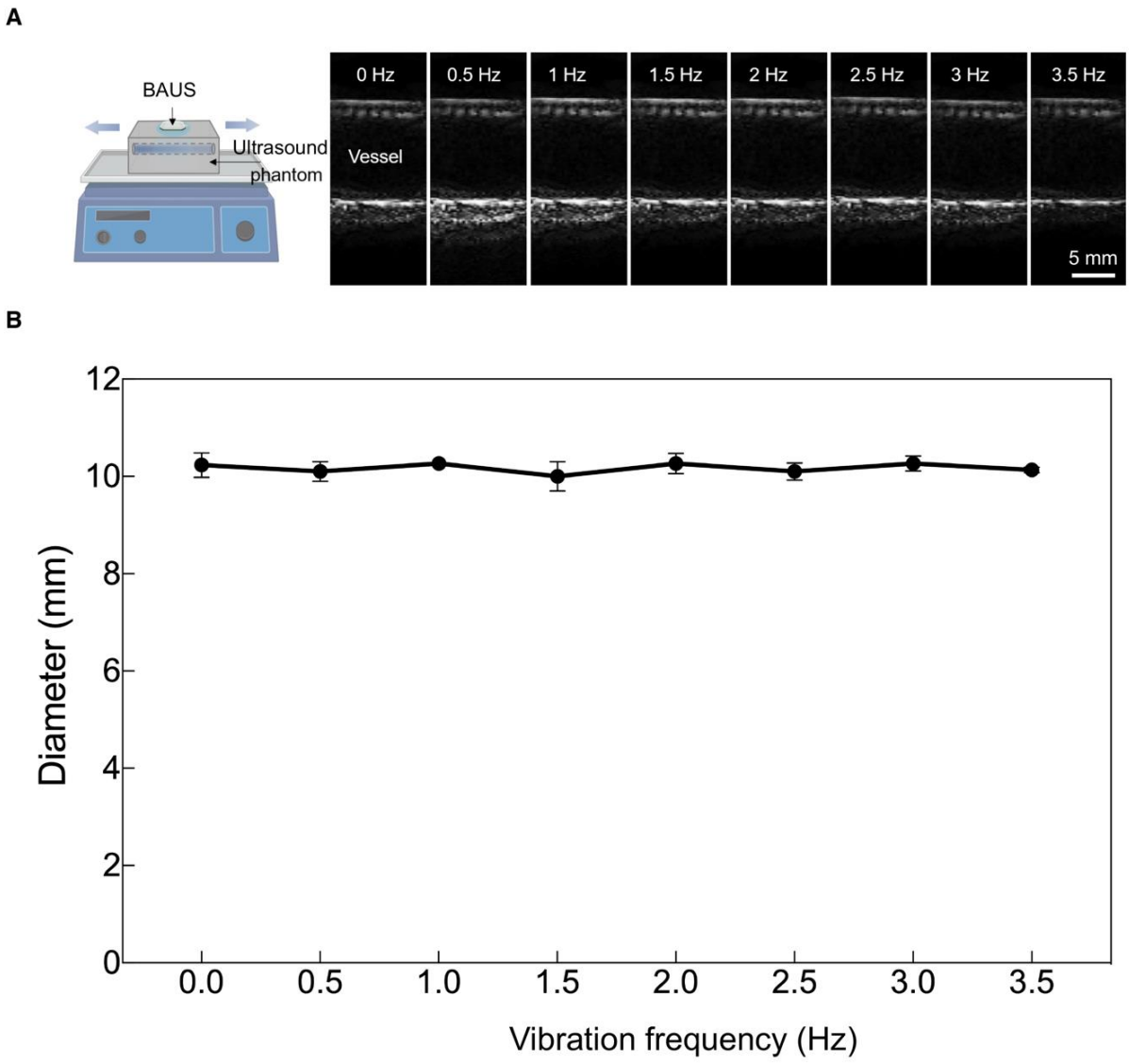

Fig. S23.

Anti-vibration performance of the BAUS device. A. Schematic illustration of the anti-vibration testing setup and the imaging results of the test. Testing setup consists of an orbital shaker with a vibration frequency from 0~3.5 Hz and an ultrasound phantom on the top of the shaker. Imaging of a mock vessel in the ultrasound phantom by the BAUS device at different vibration frequencies. C. Quantitative analysis of the diameter of the mock vessel imaged by the BAUS device at different vibration frequencies. Error bar values represent mean +/- SD (n = 3 independent samples).

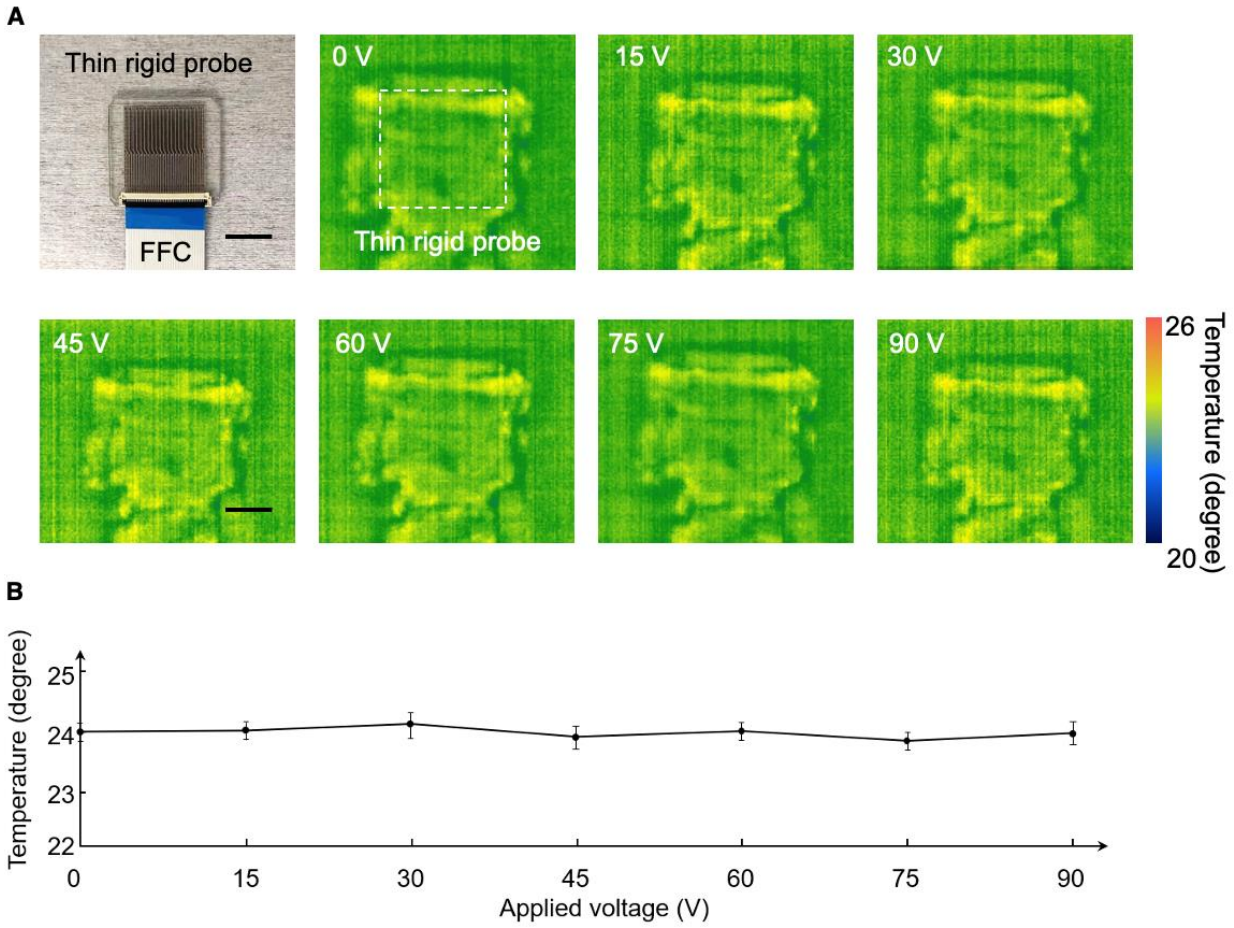

Fig. S24.

Thermal characterization of the BAUS device under various working voltages. A. Thermal images show the temperature mapping of the BAUS device under 0, 15, 30, 45, 60, 75, 90 V working voltages. B. The highest temperature on the device versus the working voltage. Error bar values represent mean +/- SD of the highest temperature on the device surface (n = 3 independent samples). Scale bar, 10mm.

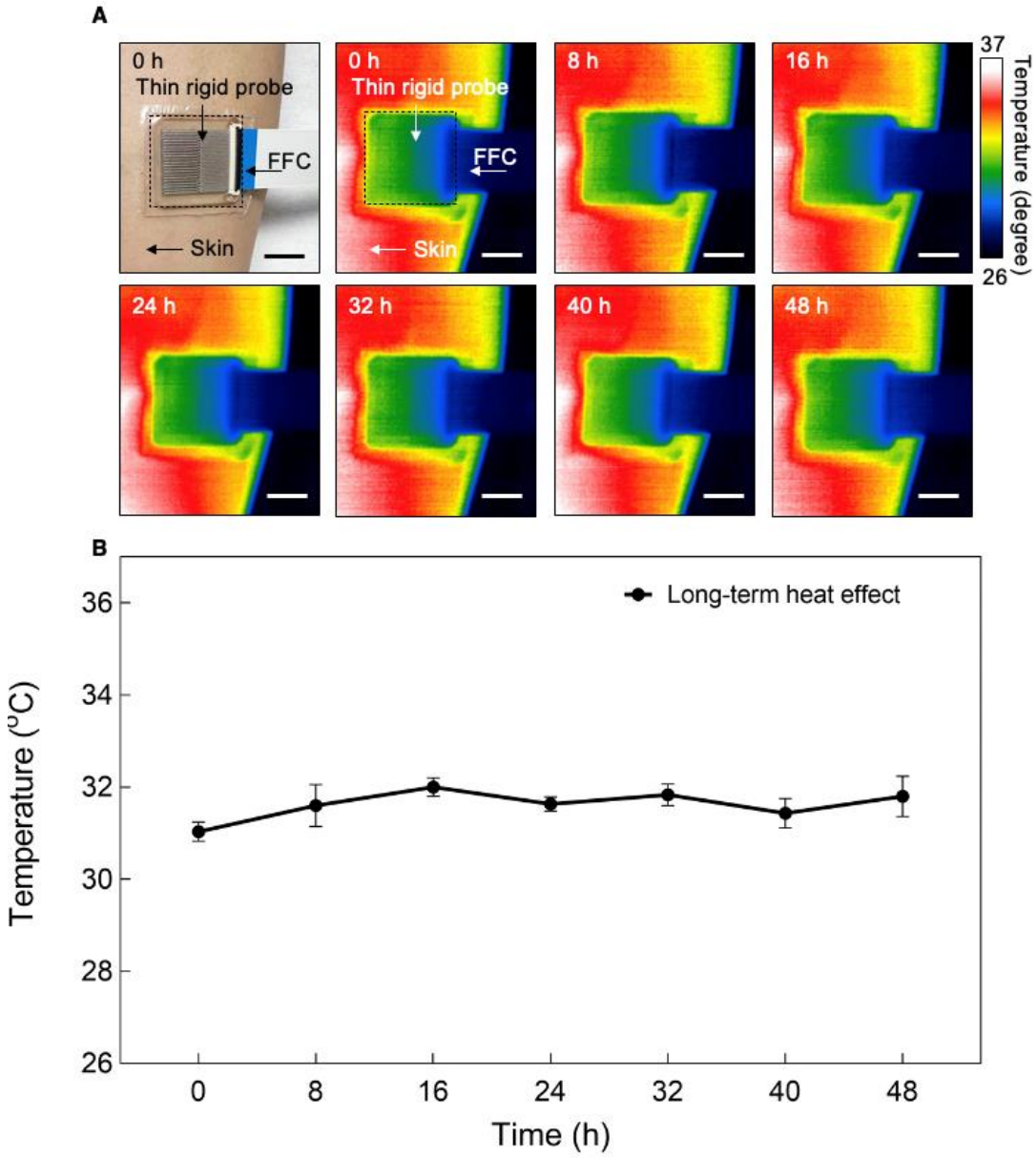

Fig. S25.

Thermal characterization of the BAUS device adhered on the skin under 90 V working voltage for 48 hours. Thermal images show the temperature mapping of the BAUS device under 90 V working voltage for 48 hours. B. The highest temperature on the device versus time. Error bar values represent mean +/- SD of the highest temperature on the device surface (n = 3 independent samples). Scale bar, 10mm.

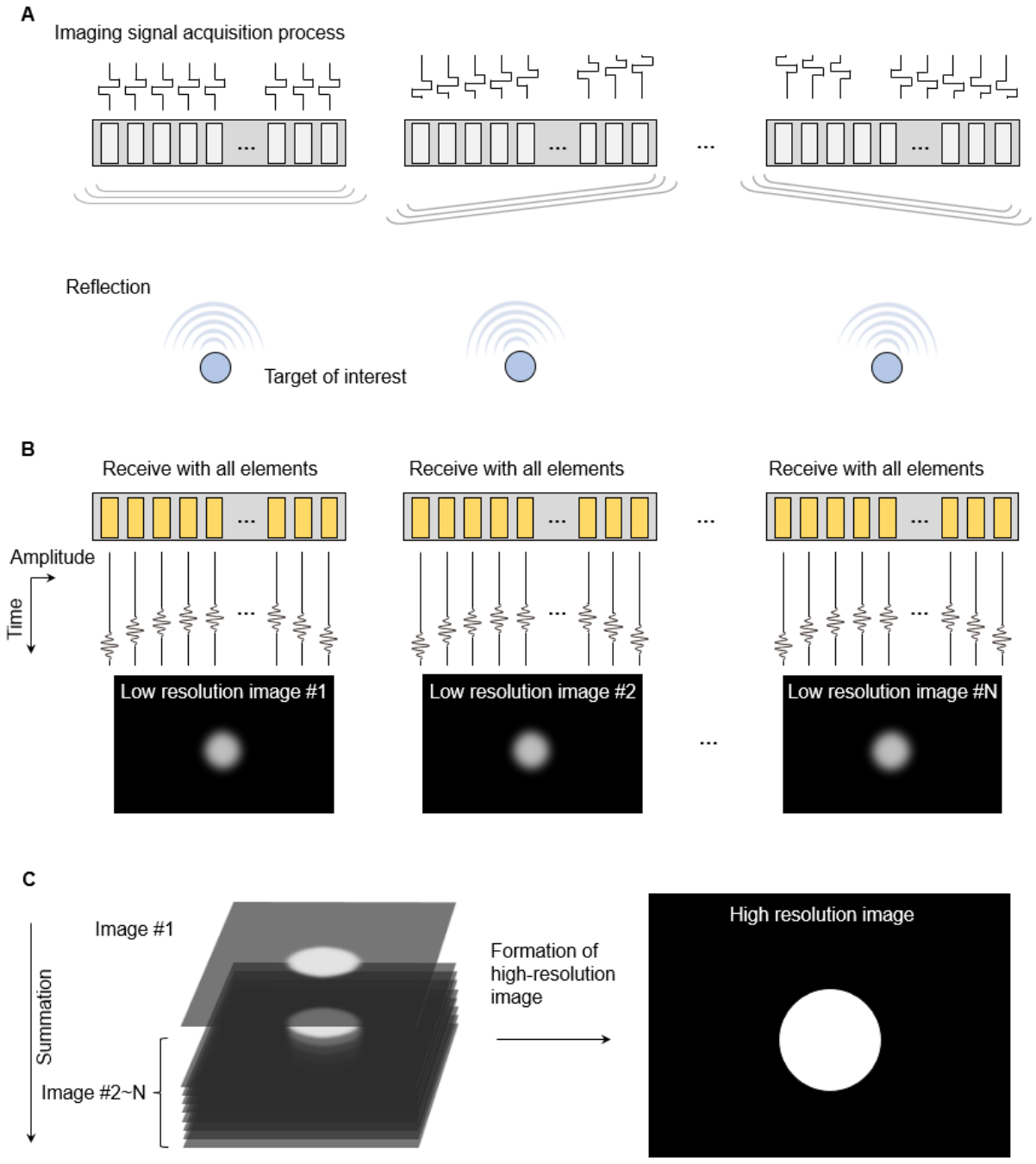

Fig. S26.

Principle of the plane wave compounding method. A. Plane waves from multiple angles can be generated by applying flat time-delay profiles to all elements. B. The radio frequency (RF) data of the ultrasound waves are collected by all elements. The data can be used for constructing multiple images with lower resolutions. C. Summation of these low-resolution images can lead to an image with a higher resolution.

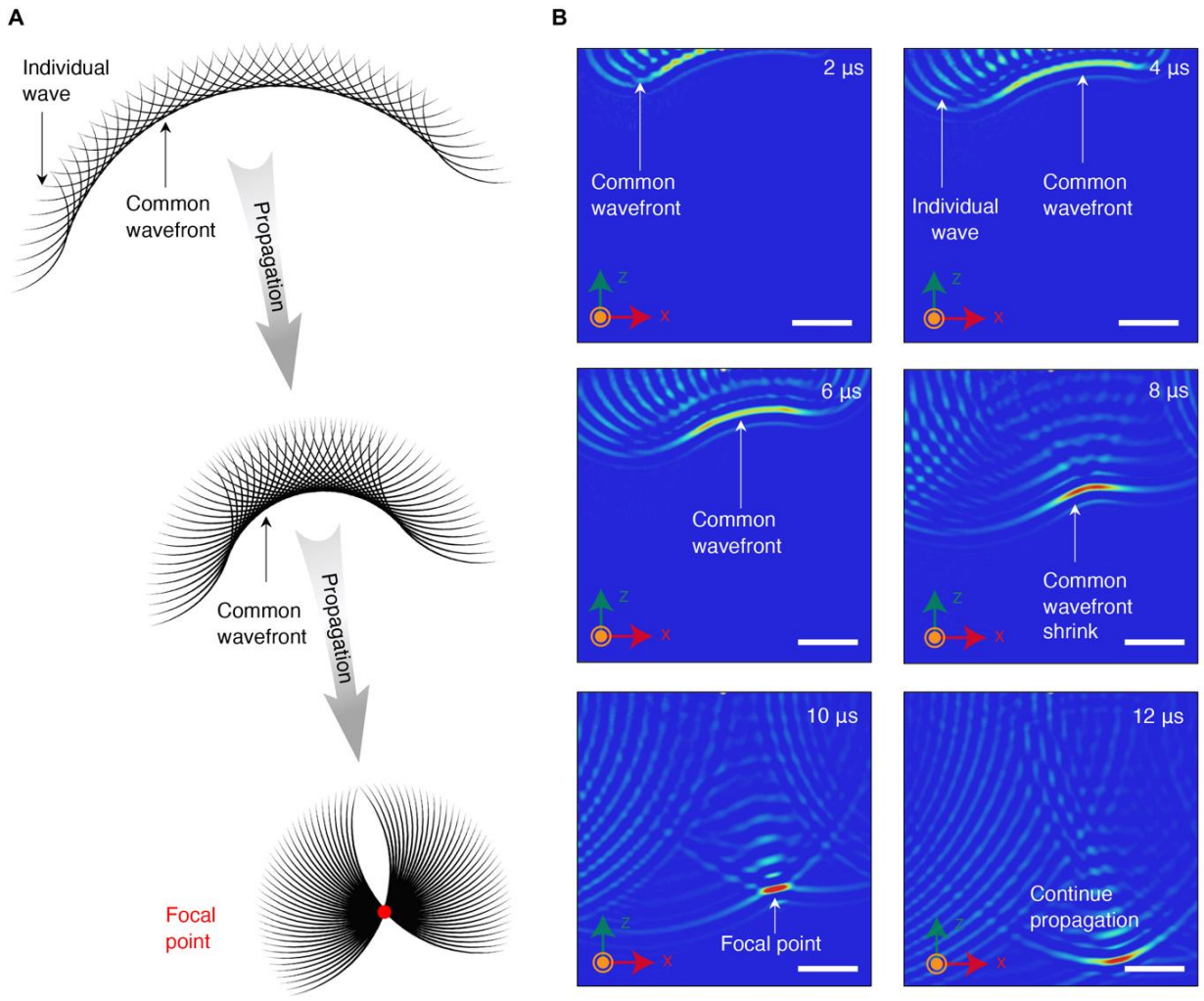

Fig. S27.

Phased array simulation of acoustic wave propagation. A. Wave generation, propagation, waveform formation, and focusing illustration of phased array. The phased array probe consists of an array of elements, each of which can be pulsed independently and generate ultrasound wave, as depicted. By programming the time delay of element array, a pattern of constructive wave interference could be generated. B. Multiphysics simulation of the physical process of the wave propagation, convergence, and focusing behavior of a phased array device (at 2, 4, 6, 8, 10, 12 μs). The simulation is performed using a package of COMSOL Multiphysics software. Scale bar, 0.4cm.

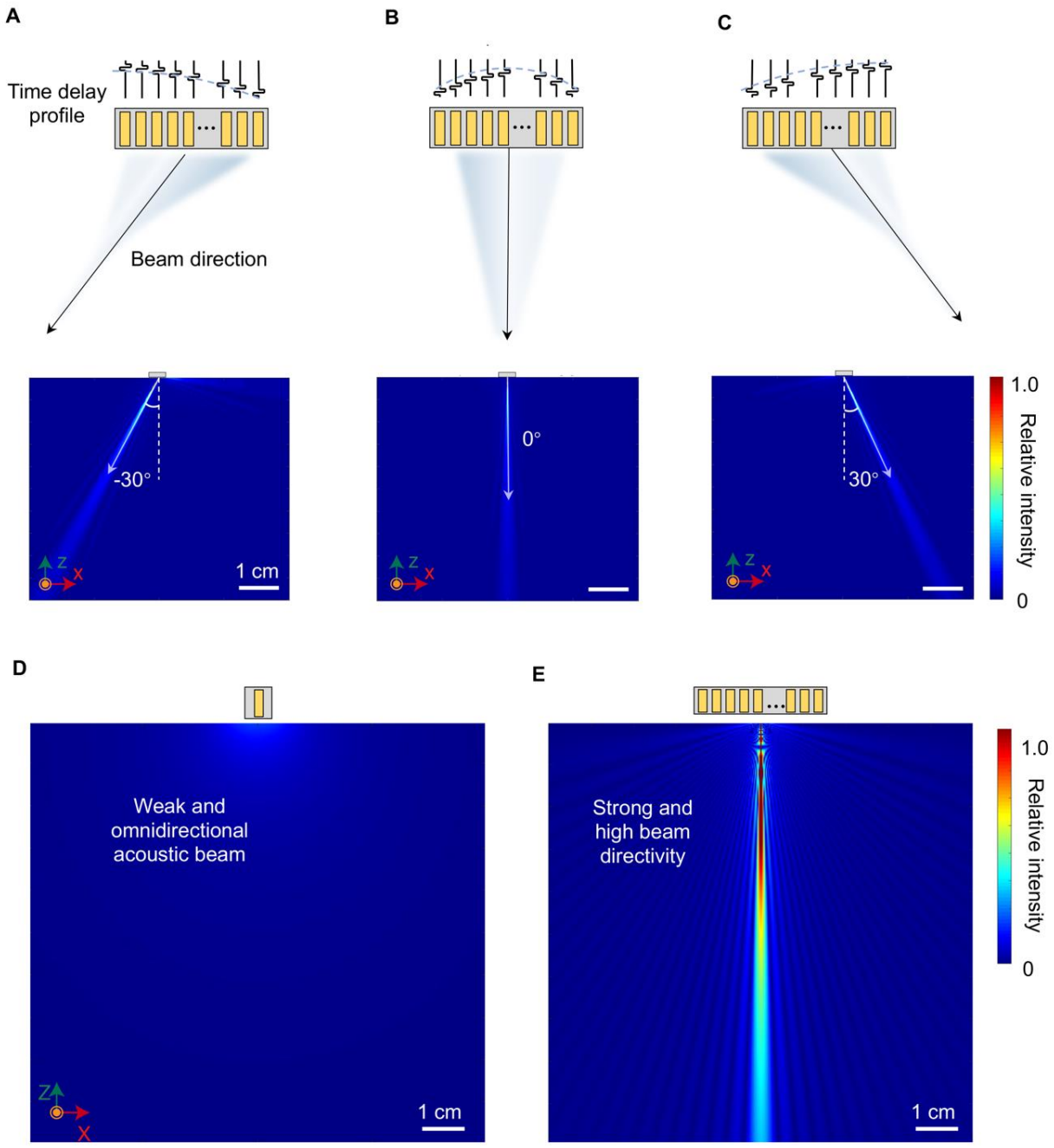

Fig. S28.

Comparison of the phased array transducer and a single-element transducer. A, B, and C show the -30-, 0-, and +30-degree beamforming with the phased array BAUS device by adopting different time-delay profile. D and E show the comparison of a single-element transducer and the phased array transducer. The single-element transducer shows weak and omnidirectional acoustic beam, and the phased array transducer can strongly enhance the beam directivity and acoustic intensity.

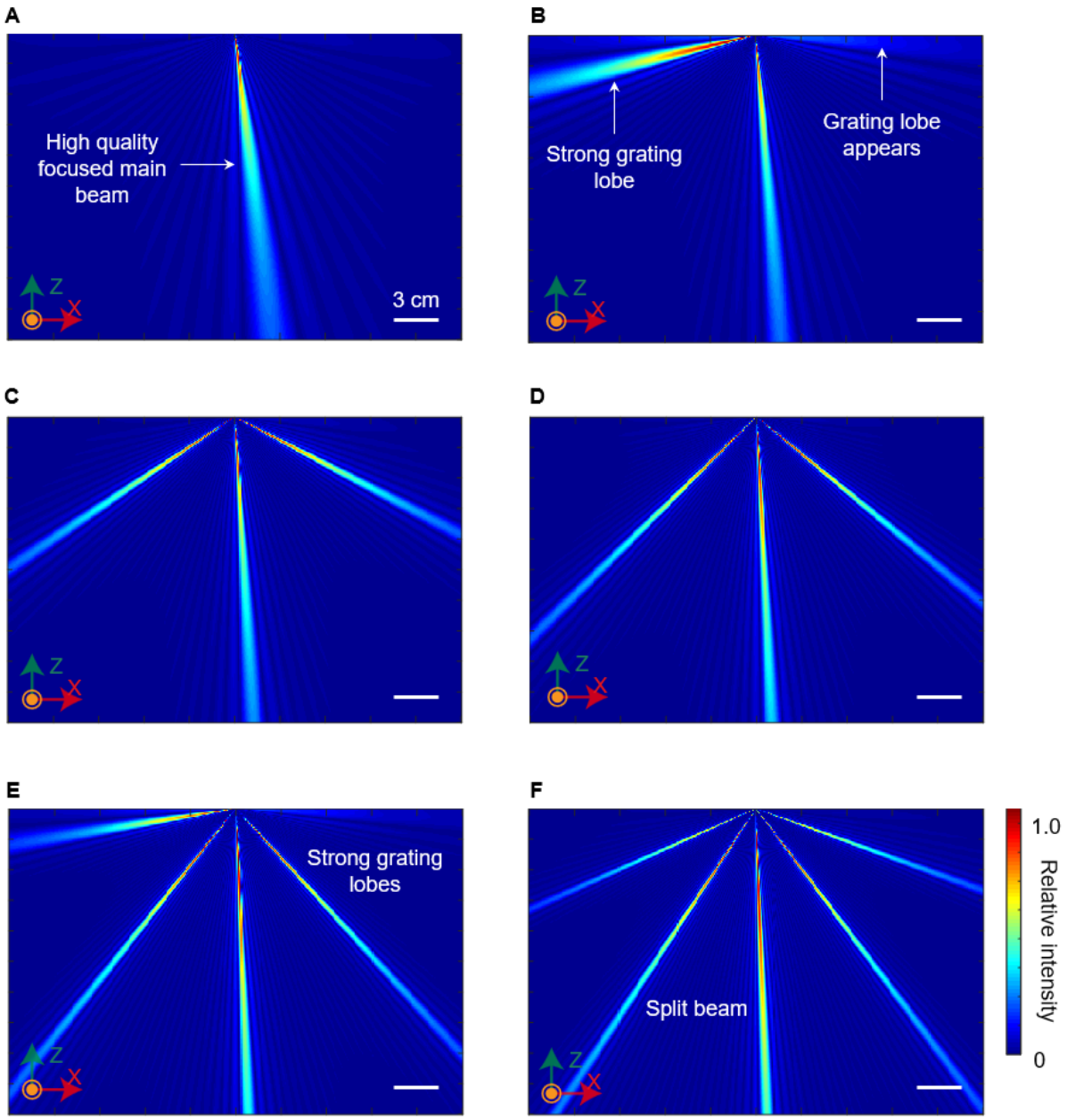

Fig. S29.

Phased array beamforming result versus diverse frequencies. A, B, C, D, E, and F are devices working under 3, 5, 7, 9, 11, and 13 MHz phased array beamforming. The series of results prove the current pitch (0.3 mm) can support 3~5 MHz phased array beamforming and the phased array applications due to the relatively small impact of the grating lobe and side lobes. A higher frequency will cause beam split and will no longer be suitable for imaging applications.

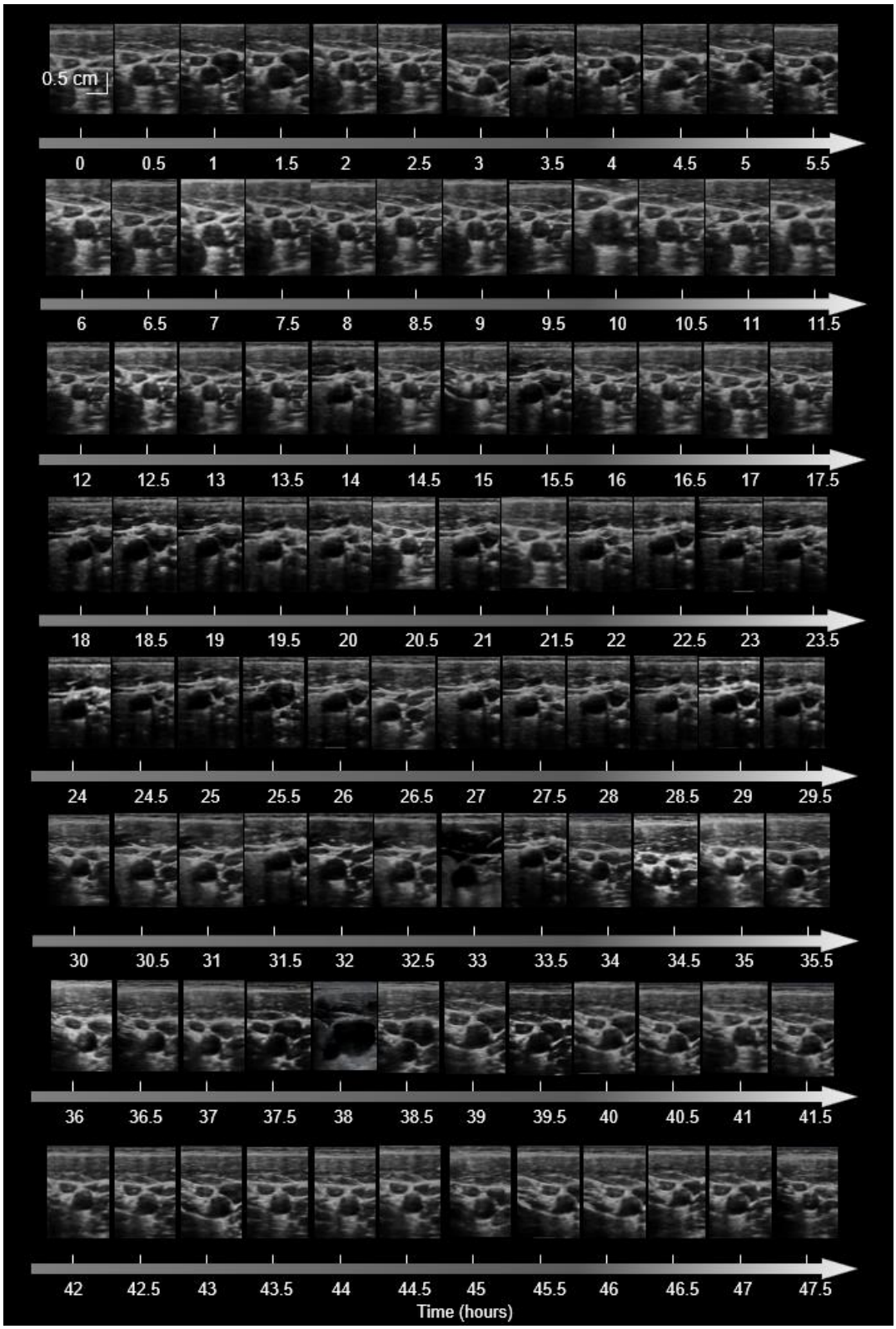

Fig. S30.

48-hour continuous imaging of the carotid artery and jugular vein. One image or a short movie (see Movie. S5) is saved every 0.5 hours.

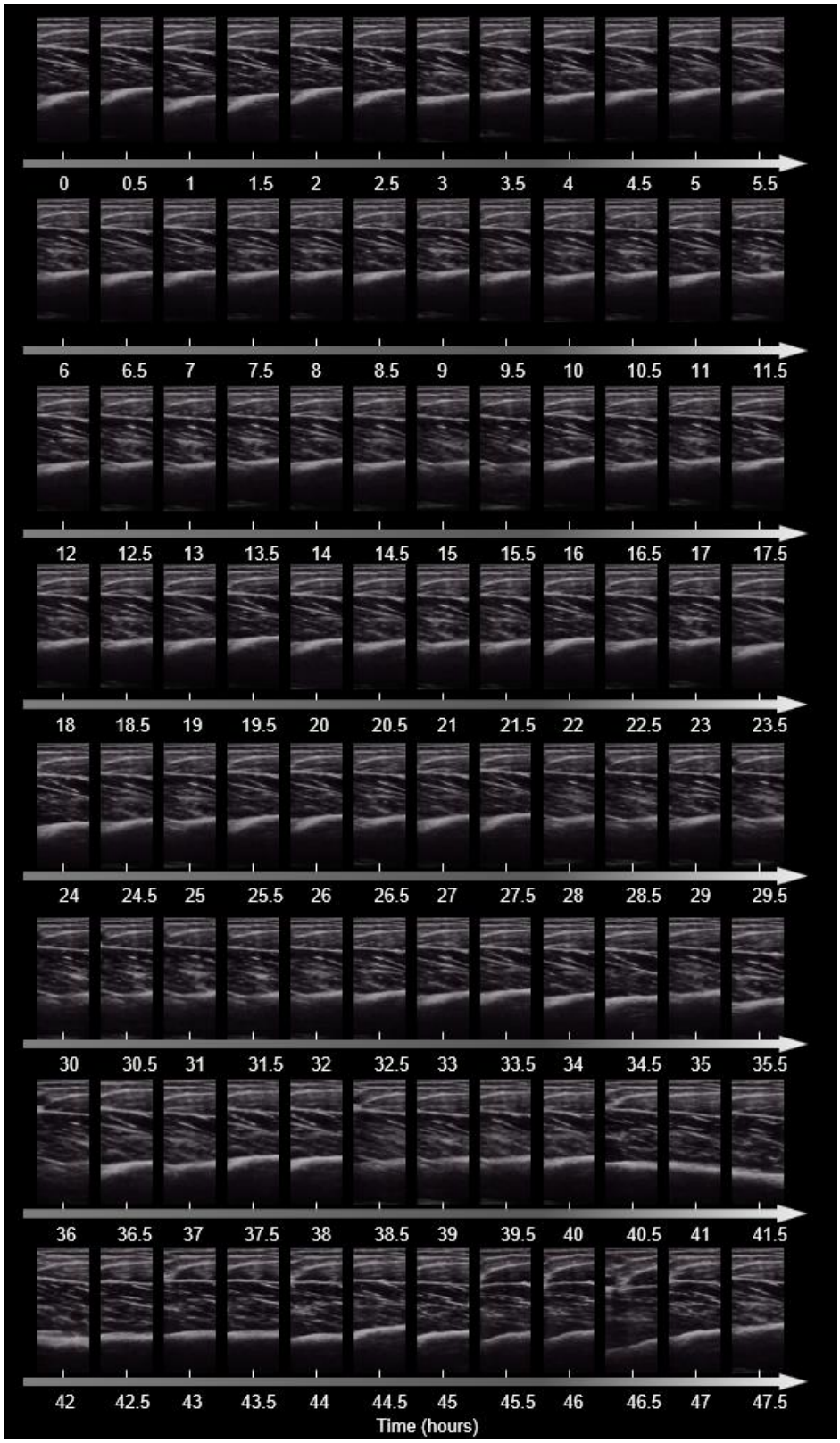

Fig. S31.

48-hour continuous imaging of the bicep muscle. One image is saved every 0.5 hours.

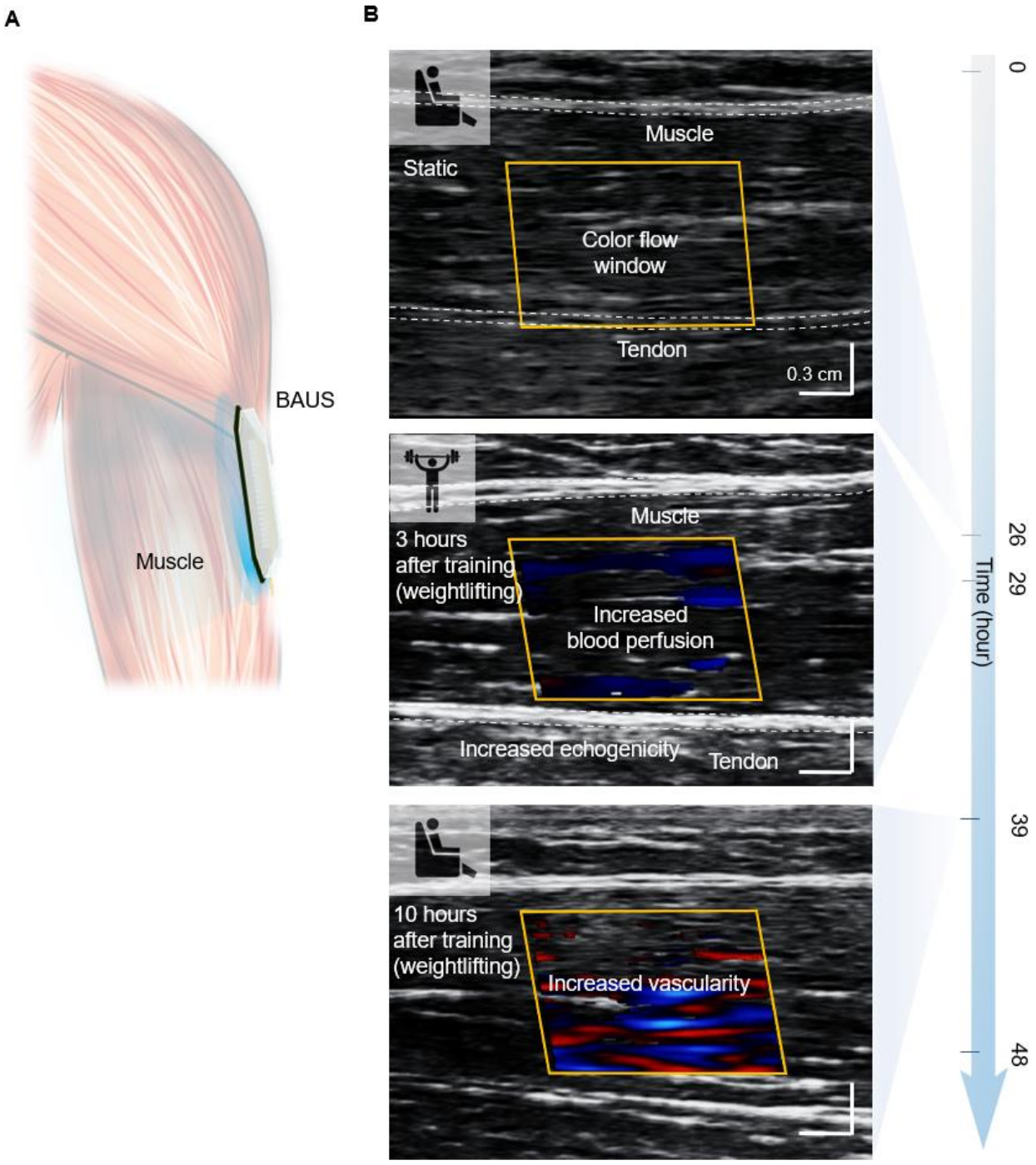

Fig. S32.
48-hour continuous imaging of the bicep muscle. Images are saved before exercise, 2 hours after the 1-hour weightlifting training, and 10 hours after the weightlifting training.

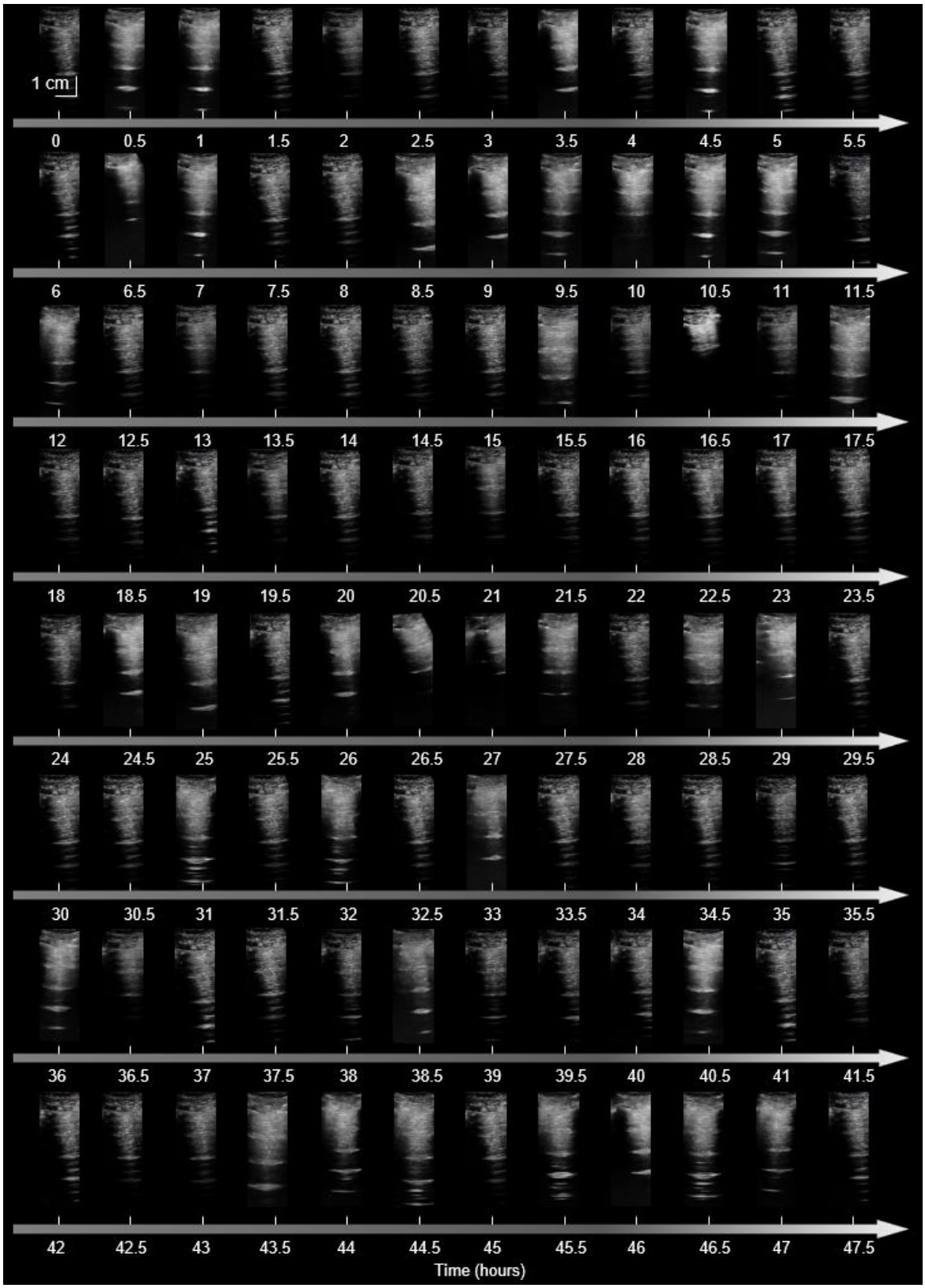

Fig. S33.

48-hour continuous imaging of the lung. One image is saved every 0.5 hours.

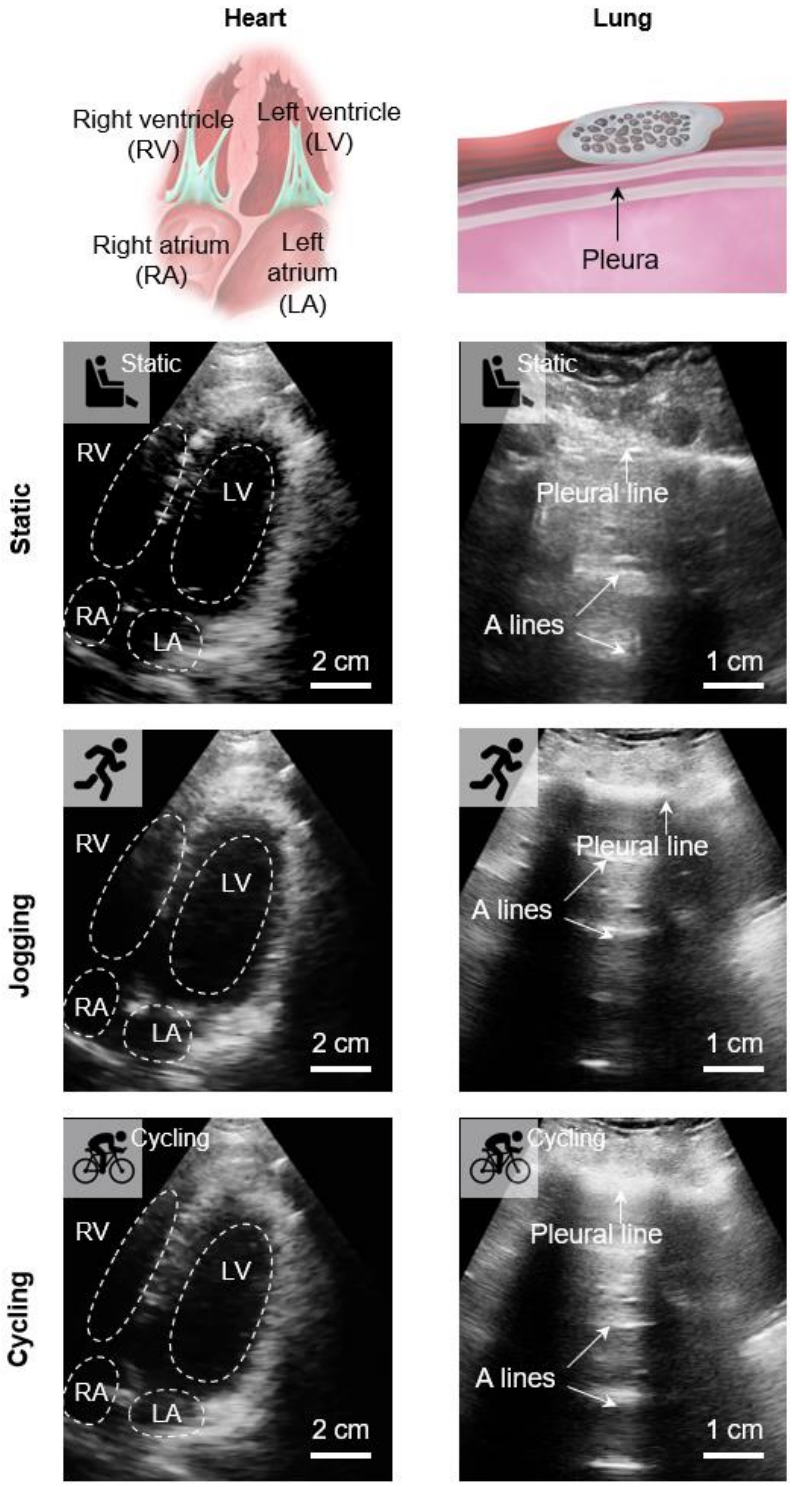

Fig. S34.

Imaging performance of the BAUS device under body motions. A. Imaging of the heart under dynamic body motions including jogging and cycling. B. Imaging of the lung under dynamic body motions including jogging and cycling.

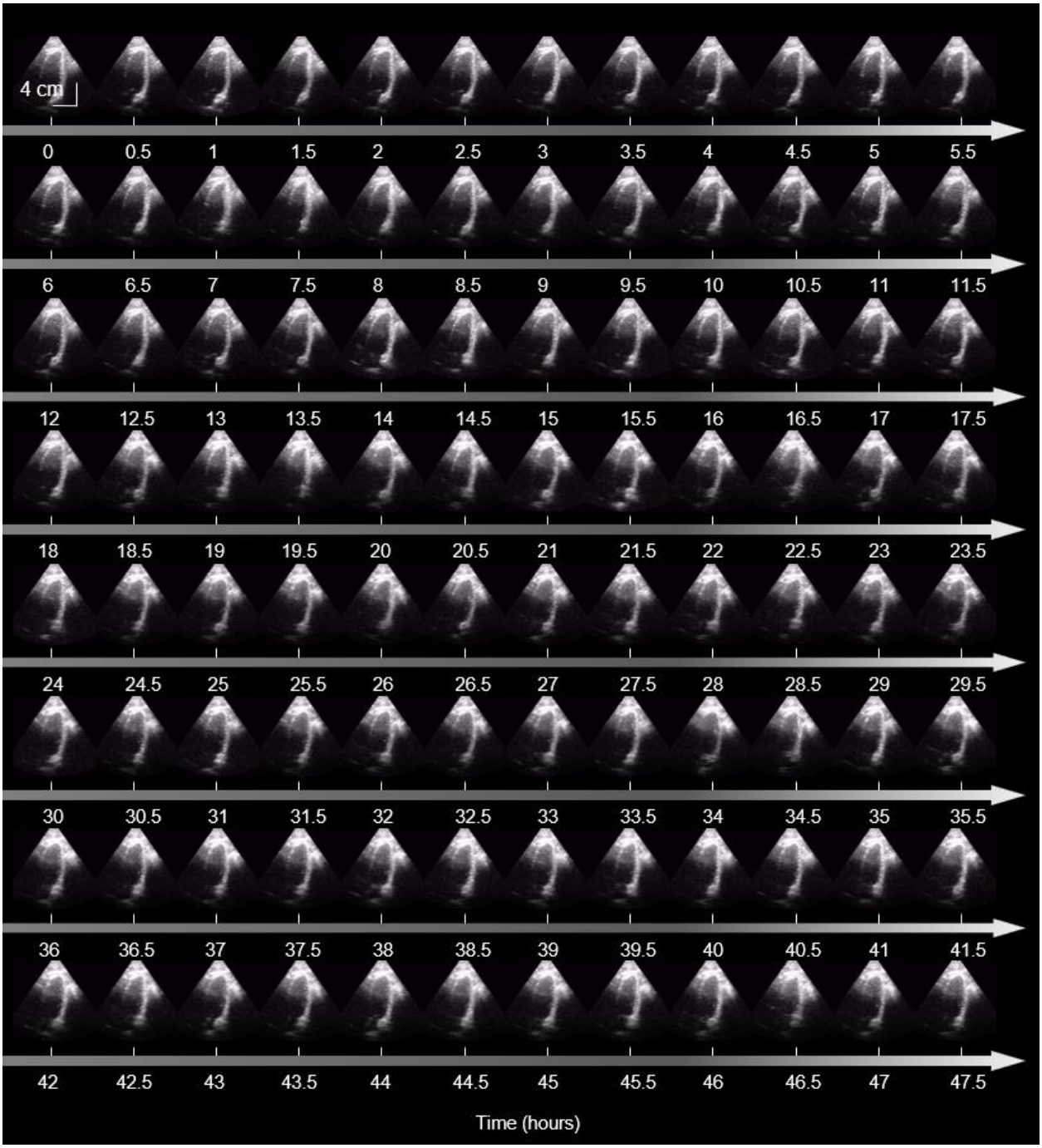

Fig. S35.

48-hour continuous imaging of the heart. One image is saved every 0.5 hours.

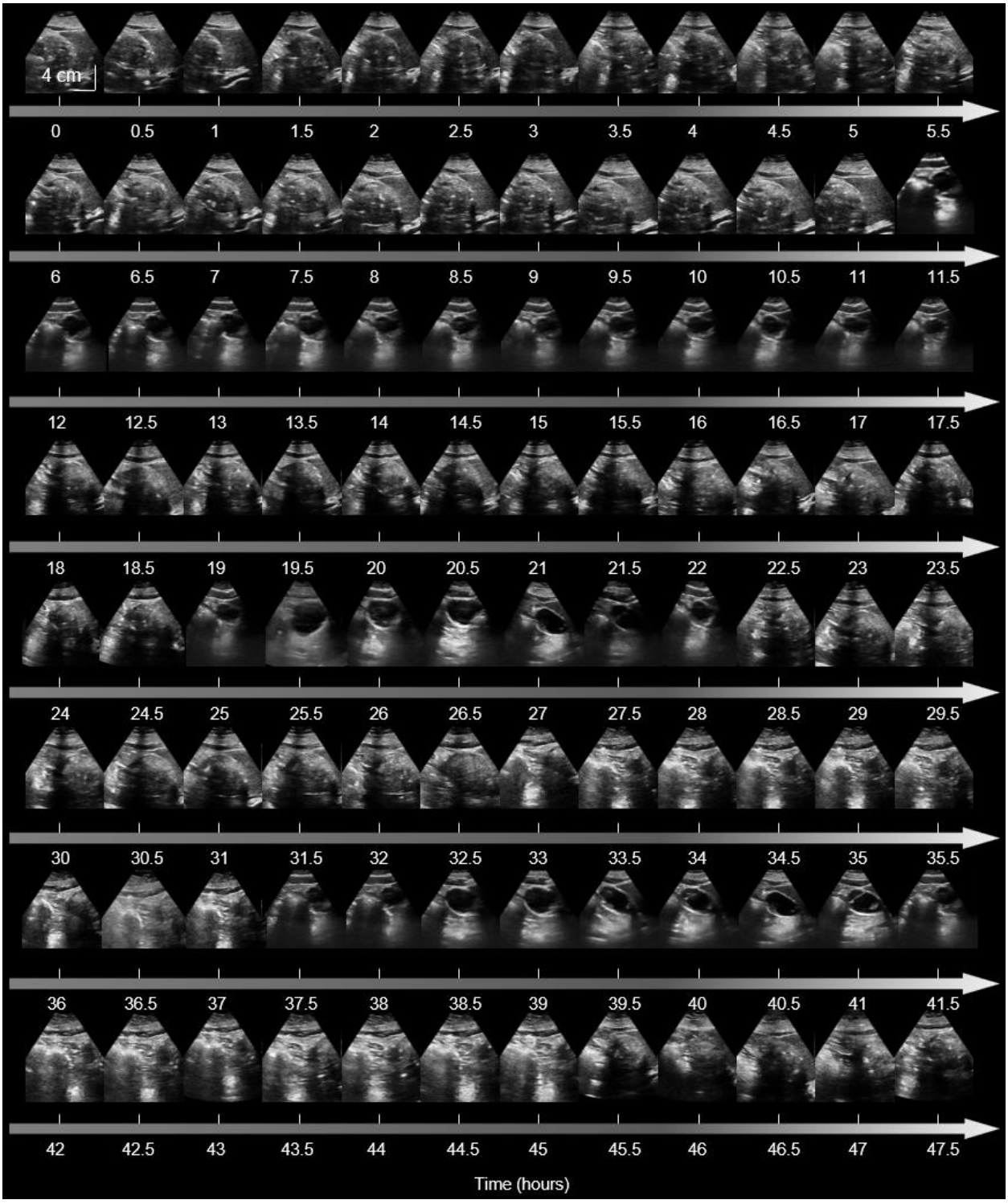

Fig. S36.

48-hour continuous imaging of the gastric atrium. One image is saved every 0.5 hours.

Table S1. Comparison of the performances of the BAUS devices and existing wearable ultrasound imaging devices.

Type of the wearable ultrasound imaging device	Wearable ultrasound (Robotic handling) *(14, 15)*	Wearable ultrasound (Mechanical fixation) *(16-18)*	Stretchable ultrasound *(12)*	Bioadhesive ultrasound (This work)
Subject freely moving?	No	Yes	Yes	Yes
Continuous imaging duration (hour)*	0.5	4	1	48
Interfacial toughness on skin (J/m^2)	<10	<10	1	>850
Probe weight (g)	>400	>400	5-10	10-40
Probe thickness (mm)	>100	>100	0.2-2	3
Frequency (MHz)	4 and 5	7.5 and 10	2	3, 7, 10
With backing and matching? (Yes/No)	Yes	Yes	No	Yes
Axial resolution (mm)**	0.578 at 4 MHz 0.462 at 5 MHz	0.308 at 7.5 MHz 0.231 at 10 MHz	5.775 at 2 MHz	0.77 at 3 MHz 0.225 at 7 MHz 0.193 at 10 MHz
Lateral resolution (mm)**	Not reported	Not reported	Not reported	1.79 at frequency of 3 MHz and focal depth of 6 cm. 0.38 at frequency of 7 MHz and focal depth of 3 cm. 0.38 at frequency of 10 MHz and focal depth of 2 cm.

*: the continuous imaging duration is defined as the longest time that a device can be adhered or worn on the skin for continuous imaging

**: See materials and method for details on evaluating the axial and lateral resolutions.

Table S2. Comparison of performances of the BAUS couplant, typical liquid (Aquasonic Clear, Parker Labs) and solid (Aquaflex, Parker Labs) hydrogel couplants, and elastomer couplants including silicone (Ecoflex, Smooth-On), acrylic tape (VHB, 3M), polyurethane (Sigma-Aldrich), and Aqualene (Olympus) on the market.

	BAUS couplant	Liquid hydrogel	Solid hydrogel	Silicone	VHB acrylic tape	Polyurethane	Olympus Aqualene
Interfacial toughness at 0 h (J/m^2)	853	<10	<10	<10	456	<10	<10
Interfacial toughness after 48 h in air (J/m^2)	756	dehydrated	dehydrated	<10	644	<10	<10
Interfacial toughness after 48 h in water (J/m^2)	518	detached	detached	detached	27	detached	detached
Wearing comfort after 48 h in air (VAS)*	1.21	8.33	6.67	2.13	2.53	2.33	3.26
Attenuation coefficient at 0 h at 3MHz 7MHz 10MHz (dB/mm)	0.0280 0.0671 0.1099	0.0708 0.1010 0.1199	0.1176 0.1323 0.1735	0.2129 0.3127 0.4705	1.3497 1.5718 2.0277	0.7388 1.0783 1.3199	0.2842 0.5061 0.7206
Attenuation coefficient after 48 h in air at 3MHz 7MHz 10MHz (dB/mm)	0.0357 0.0713 0.1314	dehydrated	dehydrated	0.2026 0.2941 0.4597	1.2603 1.6425 1.9925	0.7068 1.0627 1.3777	0.3166 0.4993 0.7056
Speed of sound (m/s)**	1548	1538	1595	989	1520	1040	1586
Acoustic impedance (MRayl)***	1.59	1.61	1.65	1.06	1.49	1.59	1.46

*: VAS is visual analogue scale. A lower VAS indicates a higher wearing comfort.

**: speed of sound in the skin is 1595-1730 m s^{-1}.

***: acoustic impedance of the skin is 1.48-1.68 MRayl.

Table S3. Design specifications of the BAUS probes

Probe center frequency	3 MHz	7 MHz	10 MHz
Probe type	Phased array	Linear array	Linear array
Number of channels	80 (2 by 40)	80 (2 by 40)	80 (2 by 40)
Element pitch (mm)	0.5	0.5	0.5
Kerf (mm)	0.1	0.1	0.1
Aperture (cm)	2	2	2
Focal depth (cm)	6	3	2
Cable length (m)	2	2	2
System Connector	Customized	Customized	Customized
Array dimension (cm)	2 by 2	2 by 1	2 by 1
Active aperture (cm)	2	2	2
Passive aperture (cm)	1	0.5	0.5
Transducer pixel number	40 by 40	40 by 20	40 by 20
Matching layer acoustic impedance Z_m (MRal)	5.4	5.4	5.4
Matching layer thickness $\lambda_m/4$ (μm)*	103.1	58.9	41.3
Backing layer thickness (mm)	2	2	2

*: λ_m is the acoustic wavelength in the matching layer.

Table S4. Acoustic properties and performances of the BAUS probes

Probe center frequency	3 MHz	7 MHz	10 MHz
Electrical impedance (Ω)	49	36	43
Crosstalk (dB)	<-40	<-40	<-40
Pulse bandwidth	68%	75%	78%
Spatial pulse length (mm)	1.54	0.55	0.385
Axial resolution (mm)	0.77	0.225	0.1925
Focal depth (cm)	6	3	2
Lateral resolution at focal depth (mm)	1.79	0.38	0.38

References and Notes

1. E. Topol, *Deep Medicine: How Artificial Intelligence Can Make Healthcare Human Again* (Basic Books, 2019).

2. M. Lin, H. Hu, S. Zhou, S. Xu, Soft wearable devices for deep-tissue sensing. *Nat. Rev. Mater.* (2022). doi:10.1038/s41578-022-00427-y

3. D.-H. Kim, N. Lu, R. Ma, Y.-S. Kim, R.-H. Kim, S. Wang, J. Wu, S. M. Won, H. Tao, A. Islam, K. J. Yu, T. I. Kim, R. Chowdhury, M. Ying, L. Xu, M. Li, H.-J. Chung, H. Keum, M. McCormick, P. Liu, Y.-W. Zhang, F. G. Omenetto, Y. Huang, T. Coleman, J. A. Rogers, Epidermal electronics. *Science* **333**, 838–843 (2011). doi:10.1126/science.1206157 Medline

4. S. Xu, Y. Zhang, L. Jia, K. E. Mathewson, K.-I. Jang, J. Kim, H. Fu, X. Huang, P. Chava, R. Wang, S. Bhole, L. Wang, Y. J. Na, Y. Guan, M. Flavin, Z. Han, Y. Huang, J. A. Rogers, Soft microfluidic assemblies of sensors, circuits, and radios for the skin. *Science* **344**, 70–74 (2014). doi:10.1126/science.1250169 Medline

5. S. Yang, Y.-C. Chen, L. Nicolini, P. Pasupathy, J. Sacks, B. Su, R. Yang, D. Sanchez, Y.-F. Chang, P. Wang, D. Schnyer, D. Neikirk, N. Lu, "Cut-and-paste" manufacture of multiparametric epidermal sensor systems. *Adv. Mater.* **27**, 6423–6430 (2015). doi:10.1002/adma.201502386 Medline

6. W. Gao, S. Emaminejad, H. Y. Y. Nyein, S. Challa, K. Chen, A. Peck, H. M. Fahad, H. Ota, H. Shiraki, D. Kiriya, D.-H. Lien, G. A. Brooks, R. W. Davis, A. Javey, Fully integrated wearable sensor arrays for multiplexed in situ perspiration analysis. *Nature* **529**, 509–514 (2016). doi:10.1038/nature16521 Medline

7. H. Lee, T. K. Choi, Y. B. Lee, H. R. Cho, R. Ghaffari, L. Wang, H. J. Choi, T. D. Chung, N. Lu, T. Hyeon, S. H. Choi, D.-H. Kim, A graphene-based electrochemical device with thermoresponsive microneedles for diabetes monitoring and therapy. *Nat. Nanotechnol.* **11**, 566–572 (2016). doi:10.1038/nnano.2016.38 Medline

8. J. R. Sempionatto, M. Lin, L. Yin, E. De la Paz, K. Pei, T. Sonsa-Ard, A. N. de Loyola Silva, A. A. Khorshed, F. Zhang, N. Tostado, S. Xu, J. Wang, An epidermal patch for the simultaneous monitoring of haemodynamic and metabolic biomarkers. *Nat. Biomed. Eng.* **5**, 737–748 (2021). doi:10.1038/s41551-021-00685-1 Medline

9. C. L. Moore, J. A. Copel, Point-of-care ultrasonography. *N. Engl. J. Med.* **364**, 749–757 (2011). doi:10.1056/NEJMra0909487 Medline

10. C. Wang, X. Li, H. Hu, L. Zhang, Z. Huang, M. Lin, Z. Zhang, Z. Yin, B. Huang, H. Gong, S. Bhaskaran, Y. Gu, M. Makihata, Y. Guo, Y. Lei, Y. Chen, C. Wang, Y. Li, T. Zhang, Z. Chen, A. P. Pisano, L. Zhang, Q. Zhou, S. Xu, Monitoring of the central blood pressure waveform via a conformal ultrasonic device. *Nat. Biomed. Eng.* **2**, 687–695 (2018). doi:10.1038/s41551-018-0287-x Medline

11. S. R. Steinhubl, E. J. Topol, A skin patch for sensing blood pressures. *Nat. Biomed. Eng.* **2**, 633–634 (2018). doi:10.1038/s41551-018-0296-9 Medline

12. C. Wang, B. Qi, M. Lin, Z. Zhang, M. Makihata, B. Liu, S. Zhou, Y. H. Huang, H. Hu, Y. Gu, Y. Chen, Y. Lei, T. Lee, S. Chien, K.-I. Jang, E. B. Kistler, S. Xu, Continuous

monitoring of deep-tissue haemodynamics with stretchable ultrasonic phased arrays. *Nat. Biomed. Eng.* **5**, 749–758 (2021). doi:10.1038/s41551-021-00763-4 Medline

13. C. K. L. Phoon, Imaging tools for the developmental biologist: Ultrasound biomicroscopy of mouse embryonic development. *Pediatr. Res.* **60**, 14–21 (2006). doi:10.1203/01.pdr.0000219441.28206.79 Medline

14. Q. Huang, J. Lan, X. Li, Robotic arm based automatic ultrasound scanning for three-dimensional imaging. *IEEE Trans. Industr. Inform.* **15**, 1173–1182 (2019). doi:10.1109/TII.2018.2871864

15. H. T. Sen, M. A. L. Bell, I. Iordachita, J. Wong, P. Kazanzides, in *2013 IEEE/RSJ International Conference on Intelligent Robots and Systems* (IEEE, 2013), pp. 3071–3076.

16. H. M. Heres, M. Sjoerdsma, T. Schoots, M. C. M. Rutten, F. N. van de Vosse, R. G. P. Lopata, Image acquisition stability of fixated musculoskeletal sonography in an exercise setting: A quantitative analysis and comparison with freehand acquisition. *J. Med. Ultrason.* **47**, 47–56 (2020). doi:10.1007/s10396-019-00983-x Medline

17. R. W. Nuckols, S. Lee, K. Swaminathan, D. Orzel, R. D. Howe, C. J. Walsh, Individualization of exosuit assistance based on measured muscle dynamics during versatile walking. *Sci. Robot.* **6**, eabj1362 (2021). doi:10.1126/scirobotics.abj1362 Medline

18. M. Sjoerdsma, C. Caresio, B. Tchang, A. Meeder, F. van de Vosse, R. Lopata, The feasibility of dynamic musculoskeletal function analysis of the vastus lateralis in endurance runners using continuous, hands-free ultrasound. *Appl. Sci.* **11**, 1534 (2021). doi:10.3390/app11041534

19. H. R. Laine, A. Harjula, P. Peltokallio, Ultrasound in the evaluation of the knee and patellar regions. *J. Ultrasound Med.* **6**, 33–36 (1987). doi:10.7863/jum.1987.6.1.33 Medline

20. F. Chasset, A. Soria, P. Moguelet, A. Mathian, Y. Auger, C. Francès, S. Barete, Contact dermatitis due to ultrasound gel: A case report and published work review. *J. Dermatol.* **43**, 318–320 (2016). doi:10.1111/1346-8138.13066 Medline

21. E. Ginzel, R. MacNeil, R. Ginzel, M. Zuber, A. Sinclar, Acoustic properties of the elastomeric materials Aqualene™ and ACE™. *NDT.net J.* **20**, 1–12 (2015).

22. J. S. Kenny, C. E. Munding, J. K. Eibl, A. M. Eibl, B. F. Long, A. Boyes, J. Yin, P. Verrecchia, M. Parrotta, R. Gatzke, P. A. Magnin, P. N. Burns, F. S. Foster, C. E. M. Demore, A novel, hands-free ultrasound patch for continuous monitoring of quantitative Doppler in the carotid artery. *Sci. Rep.* **11**, 7780 (2021). doi:10.1038/s41598-021-87116-y Medline

23. B. Y. Ahn, E. B. Duoss, M. J. Motala, X. Guo, S.-I. Park, Y. Xiong, J. Yoon, R. G. Nuzzo, J. A. Rogers, J. A. Lewis, Omnidirectional printing of flexible, stretchable, and spanning silver microelectrodes. *Science* **323**, 1590–1593 (2009). doi:10.1126/science.1168375 Medline

24. Z. Huang, Y. Hao, Y. Li, H. Hu, C. Wang, A. Nomoto, T. Pan, Y. Gu, Y. Chen, T. Zhang, W. Li, Y. Lei, N. H. Kim, C. Wang, L. Zhang, J. W. Ward, A. Maralani, X. Li, M. F.

Durstock, A. Pisano, Y. Lin, S. Xu, Three-dimensional integrated stretchable electronics. *Nat. Electron.* **1**, 473–480 (2018). doi:10.1038/s41928-018-0116-y

25. G. Hong, T.-M. Fu, M. Qiao, R. D. Viveros, X. Yang, T. Zhou, J. M. Lee, H.-G. Park, J. R. Sanes, C. M. Lieber, A method for single-neuron chronic recording from the retina in awake mice. *Science* **360**, 1447–1451 (2018). doi:10.1126/science.aas9160 Medline

26. H. Yuk, C. E. Varela, C. S. Nabzdyk, X. Mao, R. F. Padera, E. T. Roche, X. Zhao, Dry double-sided tape for adhesion of wet tissues and devices. *Nature* **575**, 169–174 (2019). doi:10.1038/s41586-019-1710-5 Medline

27. Q. Zhou, K. H. Lam, H. Zheng, W. Qiu, K. K. Shung, Piezoelectric single crystals for ultrasonic transducers in biomedical applications. *Prog. Mater. Sci.* **66**, 87–111 (2014). doi:10.1016/j.pmatsci.2014.06.001 Medline

28. S. Magder, Central venous pressure: A useful but not so simple measurement. *Crit. Care Med.* **34**, 2224–2227 (2006). doi:10.1097/01.CCM.0000227646.98423.98 Medline

29. A. E. Raine, P. Erne, E. Bürgisser, F. B. Müller, P. Bolli, F. Burkart, F. R. Bühler, Atrial natriuretic peptide and atrial pressure in patients with congestive heart failure. *N. Engl. J. Med.* **315**, 533–537 (1986). doi:10.1056/NEJM198608283150901 Medline

30. C. Xing, Q. Li, H. Du, W. Kang, J. Lian, L. Yuan, Lung ultrasound findings in patients with COVID-19 pneumonia. *Crit. Care* **24**, 174 (2020). doi:10.1186/s13054-020-02876-9 Medline

31. M. Tanter, M. Fink, Ultrafast imaging in biomedical ultrasound. *IEEE Trans. Ultrason. Ferroelectr. Freq. Control* **61**, 102–119 (2014). doi:10.1109/TUFFC.2014.2882 Medline

32. D. G. Wildes, R. Y. Chiao, C. M. W. Daft, K. W. Rigby, L. S. Smith, K. E. Thomenius, Elevation performance of 1.25 D and 1.5 D transducer arrays. *IEEE Trans. Ultrason. Ferroelectr. Freq. Control* **44**, 1027–1037 (1997). doi:10.1109/58.655628

33. L. V. Wang, S. Hu, Photoacoustic tomography: In vivo imaging from organelles to organs. *Science* **335**, 1458–1462 (2012). doi:10.1126/science.1216210 Medline

34. C. Errico, J. Pierre, S. Pezet, Y. Desailly, Z. Lenkei, O. Couture, M. Tanter, Ultrafast ultrasound localization microscopy for deep super-resolution vascular imaging. *Nature* **527**, 499–502 (2015). doi:10.1038/nature16066 Medline

35. C. Wang, X. Chen, L. Wang, M. Makihata, H.-C. Liu, T. Zhou, X. Zhao, Bioadhesive ultrasound for long-term continuous imaging of diverse organs, Version 1. Harvard Dataverse (2022); https://doi.org/10.7910/DVN/AFRFBF.

36. X. Sun, L. Yu, M. Rentschler, H. A. Wu, R. Long, Delamination of a rigid punch from an elastic substrate under normal and shear forces. *J. Mech. Phys. Solids* **122**, 141–160 (2019). doi:10.1016/j.jmps.2018.09.009

37. J. M. Meinders, A. P. Hoeks, Simultaneous assessment of diameter and pressure waveforms in the carotid artery. *Ultrasound Med. Biol.* **30**, 147–154 (2004). doi:10.1016/j.ultrasmedbio.2003.10.014 Medline

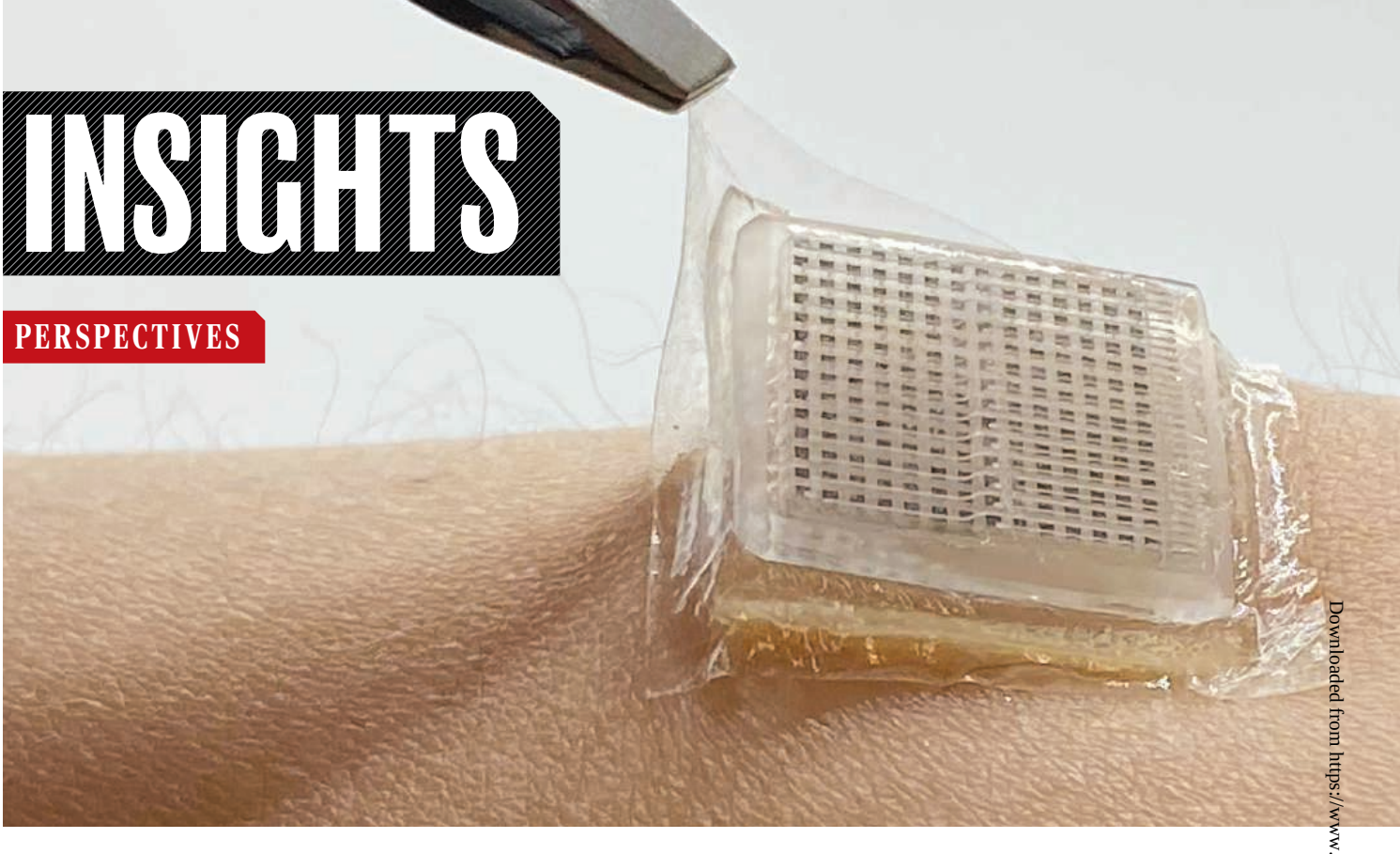

PHOTO: WANG ET AL. (3)

MEDICAL IMAGING

Seeing inside a body in motion

Adhesive ultrasound patches can provide medical imaging for patients on the go

By **Philip Tan**[1] *and* **Nanshu Lu**[1,2,3,4,5]

Ultrasonic imaging is one of the most powerful and commonplace medical tools for noninvasive visualization of soft tissues inside the body. However, ultrasonography requires highly trained sonographers to position and orient the transducer on the surface of the patient's body, and image quality is highly dependent on the steadiness of the operator's hand. Because of this, ultrasonic imaging has been largely limited to short and static sessions not only for logistical reasons but also because of the very real threat of musculoskeletal injuries for sonographers from repetitive motions associated with transducer manipulation (*1*). Coincidentally, there has also been a sonographer shortage worldwide over the past decade, and the demanding and specialized training required for certifying sonographers does not help alleviate this problem (*2*). On page 517 of this issue, Wang *et al.* (*3*) introduce a bioadhesive ultrasound (BAUS) patch with the potential to overcome many of these outstanding challenges.

Over the past few years, several wearable ultrasound patches have been developed (*4*–*7*). Although there have been improvements in transducer thinness and softness, none satisfy all the patch-tissue-interface requirements for high-quality ultrasonic imaging. To be ready for real-world applications, the patch must have stable adhesion to the body, the acoustic energy from the transducer must be transmitted efficiently into the body, and the device must not cause skin irritation. In a standard ultrasound exam, liquid gel is the de facto couplant, that is, a material that improves acoustic transmission at the transducer-tissue interface. However, conventional ultrasonic gel is only suitable for short imaging sessions because it dries out or drips down over time. Conversely, elastomer (*4*, *5*, *8*) and hydrogel (*8*) couplants have been explored but tend to have less-than-desirable transmissivity or usable time, respectively.

To overcome these weaknesses, Wang *et al.* combined the strengths of both elastomers and hydrogels by encapsulating a soft hydrogel in a thin elastomer membrane and coating it with a bioadhesive material. This hydrogel-elastomer hybrid, which they named the BAUS couplant, enables more than 48 hours of adhesion to the skin and sustained transmissivity. The soft and adhesive BAUS couplant also alleviates the stiffness of a rigid transducer array, making it more comfortable to wear. The rigid transducer array allows for a high transducer density, with 400 transducers per square centimeter.

The BAUS patch opens exciting opportunities for increasing accessibility to ultrasound exams. Although, at present, the patch still needs to be attached to a nonportable data acquisition system for processing the images, it could provide immediate relief for sonographers, for example, during sessions when a patient is undergoing anes-

[1]Department of Electrical and Computer Engineering, The University of Texas at Austin, Austin, TX 78712, USA. [2]Department of Aerospace Engineering and Engineering Mechanics, The University of Texas at Austin, Austin, TX 78712, USA. [3]Department of Biomedical Engineering, The University of Texas at Austin, Austin, TX 78712, USA. [4]Texas Materials Institute, The University of Texas at Austin, Austin, TX 78712, USA. [5]Department of Mechanical Engineering, The University of Texas at Austin, Austin, TX 78712, USA. Email: nanshulu@utexas.edu

Wang *et al*. created a hydrogel-elastomer adhesive that can be used as a conductive medium for an ultrasound transducer, which provides the flexibility needed for a wearable ultrasound imaging device.

thesia and constant monitoring of cerebral blood flow is required (*9*). In this scenario, the BAUS patch can simply be stuck to a patient's temple and provide stable blood flow imaging. The patch also opens opportunities for long-term, dynamic, high-resolution imaging of internal organs. For example, discreet monitoring of bladder volume could help people who suffer from urinary dysfunction. The inability to sense bladder fullness is a cause of urinary incontinence, leading to physiological and psychological injury, and a portable ultrasonic device for measuring bladder fullness can provide private alerts for these individuals to relieve themselves (*10*). For managing cardiovascular disease, stress echocardiograms provide valuable insights into cardiac functions, including valvular regurgitation, valve gradients, chamber volume, and myocardial strain tracking (*11*). However, the difficulty of maintaining the transducer probe during motion puts substantial logistical limits on these exams.

Thanks to excellent coupling to the tissue, the BAUS patch can capture high-quality images during a wide range of motions (see the figure). Muscular imaging enables quantification of muscle contraction, which enhances athletic training and rehabilitation of neuromuscular disorders (*12*). Also, ultrasonic imaging of the lungs has been a powerful tool for screening for respiratory diseases such as COVID-19 (*13*). A "set-and-forget" ultrasonic patch would allow for continuous monitoring of contagious patients with minimal exposure risk to the medical staff.

However, there do exist several limitations of the BAUS patch that will require future improvement. Wang *et al.* introduced a plug-and-play snap connector system that could link to several dozen transducers. However, three-dimensional ultrasonic imaging will require thousands of transducers to provide sufficient resolution. Controlling thousands of transducers requires extensive circuitry and hardware, which will limit maneuverability and mobility. Forming interconnects between transducers and the circuitry becomes more challenging with more transducers involved. Research into "ultrasound on a chip" will offer the much-desired integration of transducers with requisite analog and digital processing circuitry. The BAUS couplant has the potential to improve the long-term wearability of these systems, despite differing transducer array fabrication approaches.

To make ultrasound completely user-friendly for the average patient, artificial intelligence technology may also be needed to assist with placement and beam steering. Researchers have demonstrated an interactive application using a deep-learning model that guides the operator to manipulate the transducer to produce the best image of a target anatomy (*14*). Moving forward, automated image analysis and interpretation will be just as important as image acquisition. The road to providing universal accessibility for mobile ultrasonic imaging will require concerted efforts in diverse fields of engineering, science, and medicine. ■

REFERENCES AND NOTES

1. J. Gremark Simonsen, A. Axmon, C. Nordander, I. Arvidsson, *BMC Musculoskelet. Disord.* **21**, 156 (2020).
2. L. Waring, P. K. Miller, C. Sloane, G. Bolton, *Ultrasound* **26**, 206 (2018).
3. C. Wang *et al.*, *Science* **377**, 517 (2022).
4. J. S. Kenny *et al.*, *Sci. Rep.* **11**, 7780 (2021).
5. V. Pashaei *et al.*, *IEEE Trans. Biomed. Circuits Syst.* **14**, 305 (2020).
6. H. Chen *et al.*, bioRxiv 10.1101/2021.11.09.467971 (2021).
7. C. Wang *et al.*, *Nat. Biomed. Eng.* **5**, 749 (2021).
8. R. Manwar, L. Saint-Martin, K. Avanaki, *Chemosensors* **10**, 181 (2022).
9. I. K. Moppett, R. P. Mahajan, *Br. J. Anaesth.* **93**, 710 (2004).
10. H. Niu *et al.*, in *2011 5th International Conference on Bioinformatics and Biomedical Engineering* (IEEE, 2011).
11. T. H. Marwick, in *Echocardiography*, P. Nihoyannopoulos, J. Kisslo, Eds. (Springer, 2018), pp. 325–350.
12. B. Van Hooren, P. Teratsias, E. F. Hodson-Tole, *J. Appl. Physiol.* **128**, 978 (2020).
13. C. Xing *et al.*, *Crit. Care* **24**, 174 (2020).
14. J. M. Rothberg *et al.*, *Proc. Natl. Acad. Sci. U.S.A.* **118**, e2019339118 (2021).

ACKNOWLEDGMENTS

P.T. acknowledges the US National Science Foundation (NSF) Graduate Research Fellowship Program. N.L. is supported by the US NSF Addressing Systems Challenges through Engineering Teams (ASCENT) program under grant 2133106.

10.1126/science.adc8732

CANCER

Targeting brain cancer

A new drug is designed to hit an old target with increased precision

By **Roger Reddel** *and* **Adel Aref**

Glioblastoma (GBM) is the most common form of malignant tumor originating in the brain and is one of the most lethal cancers, with only 1 in 20 patients surviving for 5 years after diagnosis (*1*). The relentless growth of cancers such as GBMs results from DNA mutations and epigenetic changes, but these also create opportunities for targeted therapies. On page 502 of this issue, Lin *et al.* (*2*) describe a new approach to killing GBM cells that targets a well-known molecular change in GBMs: the decreased expression of the DNA repair enzyme O^6-methylguanine methyltransferase (MGMT). The authors develop a new agent that exploits this reduced DNA repair capacity and propose that their approach could be generalized to other cancers with defective DNA repair.

The expression of the *MGMT* gene is repressed by DNA methylation of its promoter. This occurs in ~50% of GBMs and >70% of lower-grade gliomas (grades II and III), and less frequently in other cancers (*3*). How this change contributes to oncogenesis is unclear, but MGMT interacts with the p21 and proliferating cell nuclear antigen (PCNA) cell cycle proteins (*4*), so lack of MGMT protein presumably contributes to unrestrained cell proliferation. What is much clearer is that MGMT provides a critical function in maintaining the integrity of DNA, with its primary function being to repair O^6-methylguanine DNA adducts, which cause base-pairing with thymine rather than cytosine and thus can introduce mutations during DNA replication. MGMT repairs these adducts through a "suicide" mechanism in which it transfers the methyl group from damaged DNA to the sulfur group in its internal acceptor site, inactivating itself (*3*).

One of the few therapeutic interventions that has well-documented benefit in GBM

Children's Medical Research Institute, Faculty of Medicine and Health, The University of Sydney, Westmead, NSW, Australia. Email: rreddel@cmri.org.au

Seeing inside a body in motion

Philip TanNanshu Lu

Science, 377 (6605), • DOI: 10.1126/science.adc8732